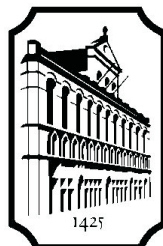


ACTA BIOMEDICA LOVANIENSIA 586
KU Leuven
Group Biomedical Sciences
Faculty of Medicine
Department of Radiology
LUCMFR

Guozhi ZHANG

DEVELOPMENT, VALIDATION AND
APPLICATION OF A HYBRID SIMULATION
TECHNIQUE FOR CONE BEAM CT IN
HEAD AND NECK IMAGING



LEUVEN UNIVERSITY PRESS

Thesis submitted in partial fulfillment of the requirements for the degree
of «Doctor of Biomedical Sciences»

Promoter:	Prof. Dr. Hilde Bosmans
Co-promoters:	Prof. Dr. Reinhilde Jacobs Prof. Dr. Ria Bogaerts
Chair:	Prof. Dr. Philippe Demaerel
Secretary:	Prof. Dr. Frederik Maes
Jury members:	Prof. Dr. Frederik Maes Prof. Dr. Piet Van Duppen Prof. Dr. Habib Zaidi Dr. Filip Vanhavere

©2012 by Leuven University Press / Presses Universitaires de Louvain / Universitaire Pers
Leuven.
Minderbroedersstraat 4 - bus 5602, B-3000 Leuven (Belgium)

All rights reserved. Except in those cases expressly determined by law, no part of this
publication may be multiplied, saved in an automated data file or made public in any way
whatsoever without the express prior written consent of the publishers.

ISBN 978 94 6165 065 8
D/2012/1869/61
NUR: 876

Acknowledgement

It was Dr *Fritz Herlach*, a retired professor from the KU Leuven physics department, who visited my home institution, HUST, in China in summer 2008 and motivated me to pursue a PhD over here. Before that, I must thank my advisers at the *Britton Chance* center in HUST as well as from the RPI in the United States for giving me the best early training, a great fortune throughout my career. I would also like to thank my parents for their understanding about my decision to spend a few years in Europe.

In my journey of making this thesis, I got to know many new people and also got to know better about myself. My first thanks are to *Hilde*, my dear promoter, for her rock continuous support, especially for each time I dragged her with me into the office of other professors that I wanted to consult, each time I dragged her with me into the visit to companies or factories where I wanted to learn their secrets, each time I dragged her with me to the experts at conferences with whom I wanted to talk, and many many such times that she was always by my side. I am also grateful to my dear co-promoters, *Reinhilde* and *Ria*, who have always been nice, encouraging and most importantly believing in me.

This thesis couldn't have been completed without the help of others. I owe *Johan* and *Frederik*, two extraordinary experts in engineering, for their help at the most difficult points of my PhD project. I would love to consider them also as my promoters.

I gratefully acknowledge Profs Philippe Demaerel and Steven Dymarkowski for chairing my defense and the thesis evaluation. I thank the jury of my thesis advisory committee, Profs Piet Van Duppen, Frederik Maes, Habib Zaidi and Dr Filip Vanhavere, for their guidance, reading and commenting on this thesis.

I thank everyone of the breast imaging group and the oral imaging group as well as all my friends in Leuven for being around and for many things, not just work. They are big part of this thesis story too. I am grateful to all the people that I know from our radiology department and the imaging clinic. I would also like to thank the companies that have been working with us.

Finally, acknowledgement goes to the financial support, the OT research fund of KU Leuven, which made this PhD project a reality.

Guozhi

Contents

Acknowledgement	v
Contents	vii
List of Acronyms	xi
I. General Introduction	1
I.A. Cone beam computed tomography	2
I.B. Monte Carlo technique	3
I.C. Thesis objectives and structure	5
II. Preliminary Study	9
II.A. Introduction	10
II.B. Materials and methods	11
II.B.1. Rat anatomical dataset	11
II.B.2. Organ surface reconstruction	12
II.B.3. NUBRS fitting	12
II.B.4. Whole-body integration	13
II.B.5. Voxelization	14
II.B.6. Monte Carlo implementation	14
II.C. Results and discussion	15
II.C.1. Rat computational phantom	15
II.C.2. Simulated cone beam CT images	17
II.D. Conclusion	18
III. Hybrid Simulation Technique	19
III.A. Introduction	20
III.B. Simulation	21
III.B.1. Oral CBCT system	21
III.B.2. X-ray source simulation	21
III.B.3. Projection simulation	23
III.B.4. Detector simulation	25
III.C. Validation	28
III.C.1. Monte Carlo calibration and dose validation	28

III.C.2. Scatter validation	30
III.C.3. Image validation	30
III.D. Results	32
III.D.1. Doses	32
III.D.2. Scatter	33
III.D.3. Images	33
III.E. Discussion	35
III.F. Conclusion	36
IV. Application: System Design	37
IV.A. Introduction	38
IV.B. Materials and methods	38
IV.B.1. Scanora 3D CBCT system	38
IV.B.2. Hybrid simulation technique	40
IV.B.3. Simulation model for original filtration design with the offset scanning geometry	41
IV.B.4. Development of bowtie filters	41
IV.B.5. Simulation of bowtie filtration	45
IV.B.6. Phantoms	45
IV.C. Assessment and results	46
IV.C.1. Radiation field	46
IV.C.2. Dose	48
IV.C.3. Scatter	49
IV.C.4. Image quality	49
IV.D. Discussion	50
IV.E. Conclusion	52
V. Application: Dose Evaluation	53
V.A. Introduction	54
V.B. Materials and methods	55
V.B.1. CBCT systems	55
V.B.2. Phantoms	55
V.B.3. Monte Carlo simulation model	56
V.B.4. Monte Carlo calibration	58
V.B.5. Dose calculation schema	60

V.C. Results	63
V.C.1. Calibration factors and dose statistical uncertainty	63
V.C.2. Organ and effective doses	64
V.C.3. Dose profiles.....	67
V.C.4. Comparison with experimentally measured dose data	67
V.D. Discussion	68
V.E. Conclusion	69
VI. Application: Image Quality	71
VI.A. Assessment of central artefact in cone beam CT with offset scanning geometry	72
VI.A.1. Introduction.....	72
VI.A.2. Materials and methods	73
VI.A.3. Results and discussion	75
VI.A.4. Conclusion	76
VI.B. Model-based volume restoration for Monte Carlo scatter correction in cone beam CT with limited field of view	77
VI.B.1. Introduction.....	77
VI.B.2. Materials and methods	78
VI.B.3. Results and discussion.....	80
VI.B.4. Conclusion	81
Concluding Summary.....	83
Bibliography.....	89
Abstract.....	95
Professional career Guozhi Zhang	97

List of Acronyms

<i>1/2/3/4-D</i>	One-/Two-/Three-/Four-Dimension
<i>ART</i>	Algebraic Reconstruction Technique
<i>BCSE</i>	Bremsstrahlung Cross-Section Enhancement
<i>BEP</i>	Bone-Equivalent Plastic
<i>CBCT</i>	Cone Beam Computed Tomography
<i>CM</i>	Component Module
<i>CPU</i>	Central Processing Unit
<i>CT</i>	Computed Tomography
<i>CTDI</i>	Computed Tomography Dose Index
<i>DAP</i>	Dose-Area Product
<i>DBS</i>	Directional Bremsstrahlung Splitting
<i>ESF</i>	Edge Spread Function
<i>ET</i>	Extrathoracic Tissue
<i>FAD</i>	Focal spot to Axis Distance
<i>FBP</i>	Filtered Back-Projection
<i>FDD</i>	Focal spot to Detector Distance
<i>FOV</i>	Field of View
<i>FPD</i>	Flat Panel Detector
<i>FPS</i>	Frames per Second
<i>GPU</i>	Graphics Processing Unit
<i>HPA</i>	Health Protection Agency (United Kingdom)
<i>HU</i>	Hounsfield Units
<i>ICRP</i>	International Commission on Radiological Protection
<i>ICRU</i>	International Commission on Radiation Units and Measurements
<i>IDS</i>	International Dental Show
<i>IEC</i>	International Electrotechnical Commission
<i>IEEE</i>	Institute of Electrical and Electronics Engineers
<i>ITK</i>	Insight Segmentation and Registration Toolkit
<i>LSF</i>	Line Spread Function
<i>MC</i>	Monte Carlo
<i>MIRD</i>	Medical Internal Radiation Dose
<i>MMI</i>	Maximum Mutual Information
<i>MR</i>	Magnetic Resonance
<i>MSCT</i>	Multi-Slice Computed Tomography
<i>MTF</i>	Modulation Transfer Function
<i>NIST</i>	National Institute of Standards and Technology
<i>(N)NPS</i>	(Normalized) Noise Power Spectrum

<i>NRC</i>	National Research Council (Canada)
<i>NURBS</i>	Non-Uniform Rational B-Spline
<i>PMMA</i>	Polymethyl Methacrylate
<i>PSF</i>	Point Spread Function
<i>QA</i>	Quality Assurance
<i>RAM</i>	Random Access Memory
<i>RBM</i>	Red Bone Marrow
<i>ROI</i>	Region of Interest
<i>SD</i>	Sprague-Dawley
<i>SOFR</i>	Scatter-to-Open Field Ratio
<i>SPIE</i>	International Society for Optical Engineering
<i>SPR</i>	Scatter-to-Primary Ratio
<i>TLD</i>	Thermoluminescent Dosimeter
<i>VCH</i>	Visible Chinese Human

Chapter

I. General Introduction

This chapter reviews the history of x-ray cone beam computed tomography in medical imaging and describes the fundamental principle and application of the Monte Carlo technique for radiation transport simulation. The Monte Carlo technique is the basis of the hybrid simulation approach that has been developed in this doctoral study with the purpose to investigate dedicated cone beam computed tomography of the head and neck. Thesis objectives and structure can be found at the end of this chapter. More detailed introductory paragraphs can be found at the beginning of each of the following chapters.

I.A. Cone beam computed tomography

X-ray Computed Tomography (CT) is one of the most important imaging tools used in current diagnostic radiology (Doi 2006). Although the design of CT scanners has evolved enormously, the theory has never been changed from that as originally proposed by Godfrey N Hounsfield in 1967 (Hounsfield 1980). The basic structure of a CT system consists of three parts: an x-ray source, a geometrical setup for image acquisition and a detector. During the scanning process, x-ray transmission data are measured at different angles with a paired rotation of radiation source and detector around the object. The attenuation property at each position within the axial plane can be resolved mathematically from the transmission data to provide the sectional view, a process that is called image reconstruction (Seeram 2009). The most popular CT design today is the so-called Multi-Slice Computed Tomography (MSCT) (Kalender 2006). It applies a geometry where the x-rays are restricted to a *fan*-shaped radiation field and the rotational data acquisition is coupled with a translation along the axial direction. The detector resides on an arc that is subtending the fan angle. The scan, therefore, appears to be in a spiral manner. Image reconstruction is performed for individual axial slices.

Cone beam computed tomography (CBCT) is a relatively new CT technique (Gupta *et al* 2006). The name originates from its conical radiation field and the image acquisition geometry. This new modality became possible with availability of the so-called flat panel detectors (FPDs). Unlike the detector used in MSCT, FPD allows the volumetric data to be acquired within a single rotation of the paired source and detector. A comparison of the CBCT and the MSCT geometry is shown in Fig. 1.1. The reconstructed images of CBCT are composed of truly isotropic elements—voxels—in the three-dimensional (3D) space. It provides a superior spatial resolution when compared to that of MSCT, especially in the axial direction (Feldkamp *et al* 1984, Fahrig *et al* 2006, Yu *et al* 2010). Although exact comparison has been difficult to realize in practice, the associated radiation dose in CBCT is generally lower than that in MSCT. This might be attributed to its reduced imaging field of view (FOV) in most applications (Lai *et al* 2009, Loubele *et al* 2009). However, CBCT does have its limitations. The soft-tissue contrast resolution, for instance, is inferior to that of MSCT. Related factors for this shortcoming of CBCT may include the inherent characteristics of FPD and the scattered radiation. These factors have been hot topics in CBCT studies for years (Jaffray and Siewerdsen 2000, Siewerdsen and Jaffray 1999, 2000, 2001, Jarry *et al* 2006, Mail *et al* 2008, Bootsma *et al* 2011).

Clinical application of CBCT was first introduced in 1980s for angiography in interventional radiology (Orth *et al* 2009). In the nineties, CBCT was explored as a tool for image-guidance in radiotherapy (Moore *et al* 2006), which leads to the onboard CBCT units mounted onto the end of linear accelerators today. Since 2001, there has been a proliferation of dedicated CBCT systems for head and neck imaging on the commercial market (De Vos *et al* 2009, Miracle and Mukherji 2009a). As compared to the CBCT for use in interventional radiology and in radiotherapy, these systems are featured with high-speed scanning, compact design, simple operation and a wide range of exposure settings. The size of the imaging FOV is typically less than 20 cm in diameter. They are increasingly adopted in diagnostic radiology and image-guided surgery for extracranial head and neck regions, including the teeth, the mandible, the maxilla, the sinuses, the throat, the temporal bone and the skull

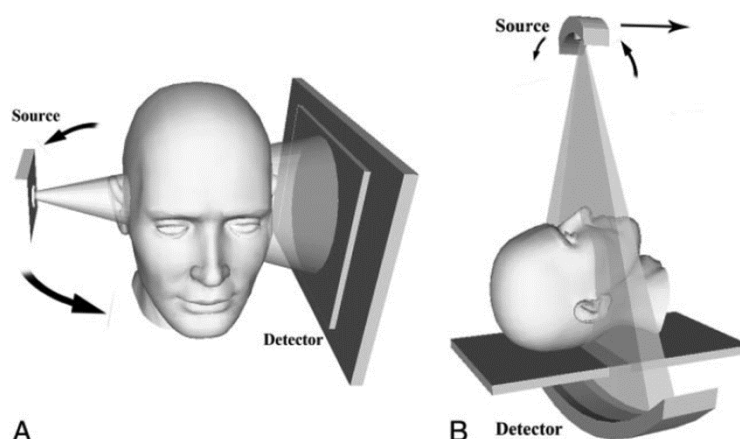


Fig. 1.1 Comparison of the (A) CBCT and the (B) MSCT geometry (Miracle and Mukherji 2009a).

base. In dental practice, CBCT has become a powerful complement to intraoral and panoramic radiography and is available in both public hospitals and private clinics. The field of application covers implantology, orthodontics, endodontics and periodontics (Guerrero *et al* 2006, Miracle and Mukherji 2009b, Mah *et al* 2010).

The extracranial head and neck regions have a very complex anatomy, mixed with bony tissue, soft tissues and air cavities. CBCT turns out to be a preferable imaging tool because of its relatively low dose requirement and the high spatial resolution. More importantly, it manages to move the imaging task from the large CT facility into the normal office space. However, it has also been under criticism as every emerging technique (Horner *et al* 2009, HPA 2010a, 2010b). Radiation safety may be an issue because the relatively easy access of dedicated head and neck CBCT can eventually lead to overuse. Regulatory policies and standardization measures are yet to be established or improved. Further evidence is needed for cases where this imaging modality can replace the traditional radiography and CT. Quality test methodologies used in general radiology still have to be adapted before applied to CBCT. Given the large difference in the performance of various commercial CBCT systems, optimization is also of great interest in current researches.

I.B. Monte Carlo technique

The *Monte Carlo* technique is named after the casinos in the city of Monte Carlo. It refers to a class of computational algorithms relying on repetitive random sampling (Fishman 1995). The Monte Carlo technique is often adopted to solve a problem with intertwining degrees of freedom that is infeasible to answer by solely deterministic methods. The exact implementation may vary in different cases but the general pattern should consist of (1) defining the input domain, (2) sampling inputs with some probabilistic distribution, (3) calculating each corresponding output under deterministic rules and (4) aggregating (integrating) the outputs. Such a repetitive nature makes it well-suited for computer simulation. The Monte Carlo technique has been widely applied in mathematics, physics, statistics, engineering, biology, finance, etc. In medical physics, the Monte Carlo technique is most popular in simulating the radiation transport of particles in matter (Andreo 1991, Rogers 2006), with applications not only in diagnostic radiology but also in diagnostic and therapeutic nuclear medicine (Ljungberg *et al* 1998, Zaidi 1999, Zaidi and Sgouros 2002). In order to illustrate all this, we consider the coupled photon/electron transport. On one hand, photons may interact with matter by pair production, photoelectric absorption, Compton scattering and Rayleigh scattering. The first three all involve some energy transfer from photons to electrons. Electrons, on the other hand, may interact

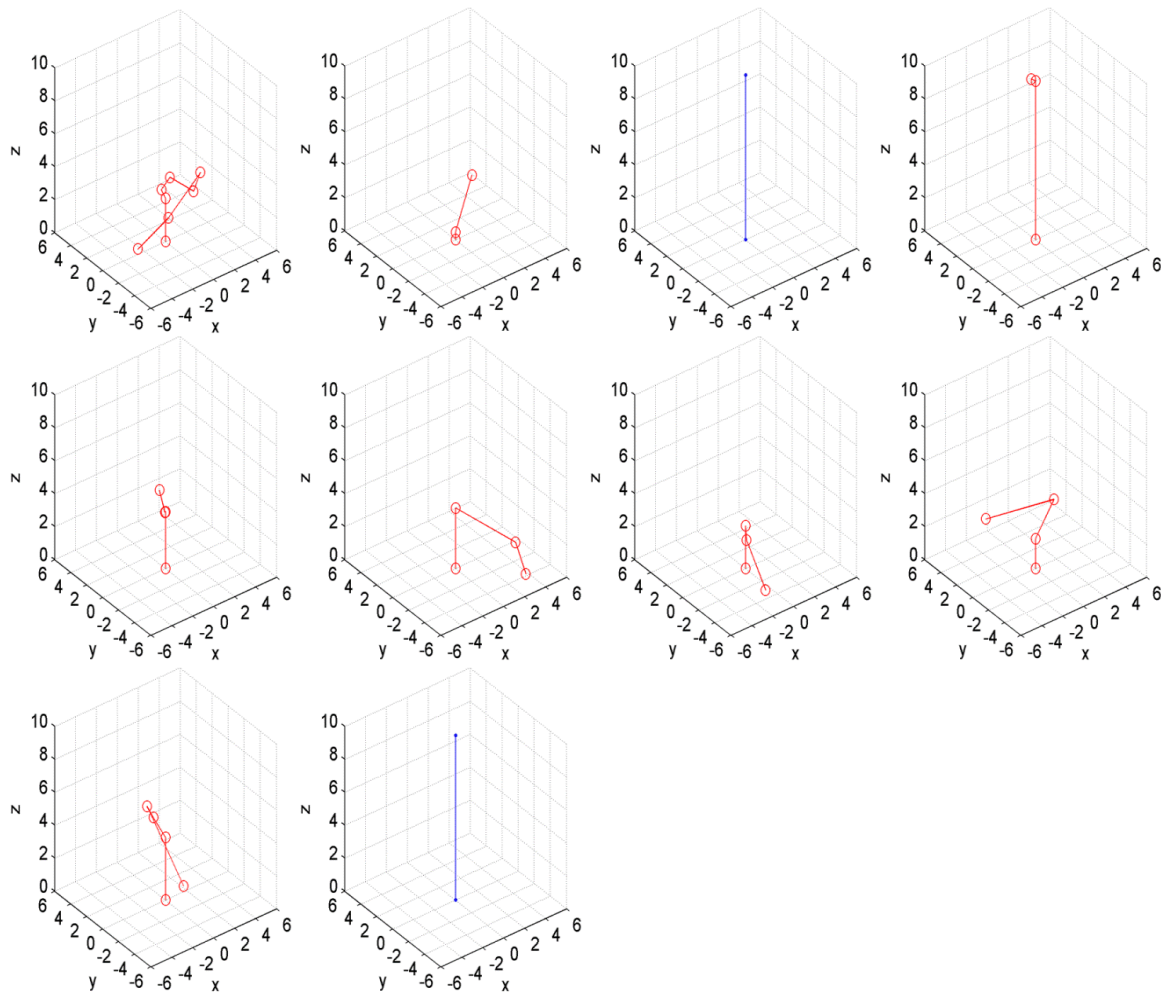


Fig. 1.2 Tracks of ten Monte Carlo histories for a 50-keV photon beam through a 10-cm water cube, where those with and without interactions are shown in red and blue, respectively. The circles indicate the sites of photon interactions.

with matter by elastic collision against the atomic nuclei, inelastic collision against the atomic electron as well as by radiation. Radiation occurs in form of Bremsstrahlung and positron annihilation, both of which involve some energy transfer from electrons to photons. In physics, the probability distribution of different interactions is defined via so-called *cross-sections*. The Monte Carlo simulation works by (1) defining the state of the initial particle and the properties of the medium; (2) transporting the particle by a certain distance to the site of interaction according to the data sampled from the total cross-section; (3) determining the type and outcome of the interaction by sampling each corresponding cross-section; (4) transporting the produced secondary particles if there is any; (5) terminating the transport when the primary and all the descendant particles either get absorbed or escape from the considered geometry. Every loop is called a *history* in Monte Carlo technique. The quantity of interest is obtained by integrating the results from multiple histories. The statistical uncertainty is therefore subject to the number of transported histories.

Monte Carlo codes for radiation transport are software tools that provide the user interfaces to the sampling rules and numerical approximations as well as the cross-section data and associated physical models. Advanced code systems also supply variance reduction techniques that can be utilized to improve the simulation efficiency and basic geometry routines that can help in defining the

Table 1.1 Photon interactions occurred in the simulation shown in Fig. 1.2.

History	Photoelectric	Compton	Rayleigh	Deposited energy (keV)
1	0	6	0	16.502
2	1	1	0	50.000
3	0	0	0	0.000
4	0	1	0	1.664
5	1	2	0	50.000
6	0	2	0	5.872
7	1	2	0	50.000
8	1	2	0	50.000
9	0	2	1	7.440
10	0	0	0	0.000
<i>Total</i>	<i>4</i>	<i>18</i>	<i>1</i>	<i>231.478</i>

problem for investigation. A few general-purpose Monte Carlo code systems are popular in the current medical physics community, such as the EGSnrc (Kawrakow *et al* 2009), MCNP (Brown 2003), GEANT (Agostinelli *et al* 2003) and PENELOPE (Salvat *et al* 2003). EGSnrc—the current version of the EGS (Electron Gamma Shower) system—makes use of a so-called *condensed history* technique for electron transport and is often considered to have a better performance in low-energy physics when compared to the others. Apart from the standard photon/electron physics, EGSnrc is also capable of simulating the binding effects in Compton scattering, the atomic relaxations, the spin effects of electrons and the electron impact ionization.

A simple case of Monte Carlo simulation is illustrated here. We used the EGSnrc to transport a 50-keV pencil x-ray beam incident perpendicularly towards the center of one face of a $10 \times 10 \times 10$ cm³ water cube. The geometry was defined in 3D Cartesian coordinates, with the beam entering from the origin. The tracks of the first ten photon histories are shown in Fig. 1.2. Secondary electrons are associated with multiple collisions in rather small ranges, which are difficult to show. Photon interactions in each history and energy deposition associated with each history are summarized in Table 1.1. It can be seen that photons in histories 3 and 10 pass through the cube without any interaction, those in histories 1, 4, 6 and 9 escape from the cube after a few interactions, and the others are totally absorbed inside.

I.C. Thesis objectives and structure

Monte Carlo simulation seems to be a powerful tool for CBCT studies by offering the possibility to look into the detailed imaging process from a physics point of view. However, real CBCT systems are very complicated in design architecture. Basic Monte Carlo simulations might therefore be limited in both accuracy and efficiency. For dedicated head and neck CBCT, the large range of exposure settings and the large difference between various imaging systems are added challenges, demanding high flexibility of the simulation platform. With the support of the internal research fund of KU Leuven (OT/08/057), a 4-year doctoral study was launched in this regard.

The objectives of the study were:

- 1) To develop an accurate, efficient and flexible simulation tool with general applicability to CBCT;
- 2) To apply the simulation tool for quality assurance, system evaluation and optimization of the dedicated head and neck CBCT.

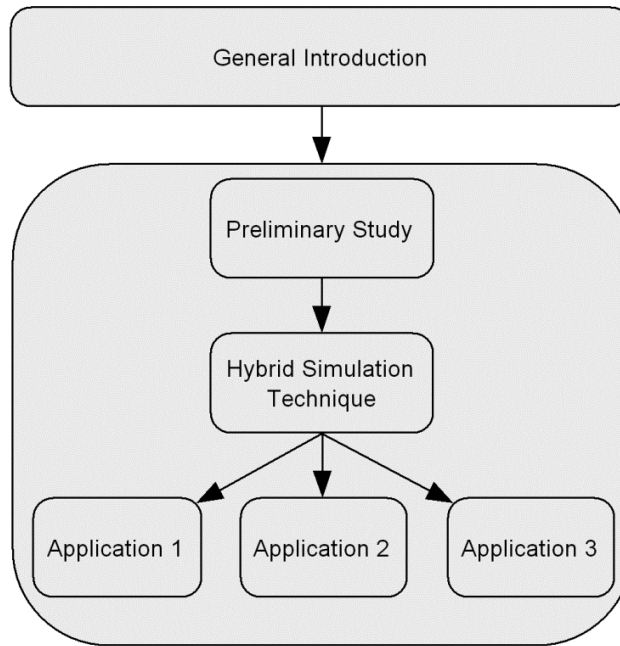


Fig. 1.3 Thesis structogram.

Accordingly, the thesis is organized in six chapters, as shown in Fig. 1.3. Apart from this chapter (**Chapter I**), the general introduction, following chapters are

- **Chapter II:** This chapter describes a preliminary study which seeks to work out the general framework of CBCT simulation. While simulating the cone-beam radiation field and angular projections using the Monte Carlo technique, special attention was paid to the object undergoing the scan. In simulation, the object is represented in form of computational phantoms. Three categories of approaches to represent the phantoms were compared: mathematical, voxel-based and boundary representation. (1) Mathematical phantoms are also called stylized phantoms. They have both their internal organ shapes and exterior contours defined by geometric shapes, e.g. planar, cylindrical, conical, elliptical and spherical surfaces. Such a representation is usually flexible in spatial alteration but fails to describe the realistic anatomy, even at the cost of using very complex mathematical expressions. (2) Voxel-based phantoms, which emerged owing to the fast computers and modern medical imaging techniques, are represented via 3D arrays of organ- or tissue-specific volume elements—voxels—segmented from transaxial medical images. Such a representation can preserve most anatomical features but relies on accurate image segmentation, which is always labor-intensive and requires high image quality. Besides, it is severely limited in its ability of geometric transform. (3) The non-uniform rational B-spline (NURBS), a powerful boundary representation tool, has been widely applied in computer graphics to describe 3D surfaces, even for rather intricate structures. It is capable of a rich set of spatial operations, and in this way combines both geometric flexibility and anatomical realism. In this study, a unique rat phantom was developed using the boundary representation approach and implemented in Monte Carlo simulation of CBCT images. A lot of experience was obtained from the phantom development and the Monte Carlo CBCT simulation, all of which was essential for the subsequent study in this thesis. This work has been published with *Proceedings of the IEEE* (Zhang *et al* 2009).

- **Chapter III:** This chapter describes an in-depth study which completes and improves the previous simulation work of CBCT. A so-called *hybrid* simulation technique was developed to model the entire imaging chain of CBCT. It starts with the x-ray generation, filtration and collimation, continues with rotational projections, calculates the 3D dose distributions, produces primary and scatter images using different methods, applies the measured characteristics of the detector, and ends with a sequence of realistic 2D projection images for reconstruction. It is hybrid in several aspects: taking into account both dose and image related aspects; splitting the simulation chain into the source, projection and detector; combining deterministic and stochastic techniques; including the measured detector characteristics; involving different variance reduction and acceleration means. This hybrid simulation technique is flexible and has wide applicability to CBCT systems. The simulation model was validated in dose, scatter and image quality with application to a dedicated oral imaging system. This work has been published with *Physics in Medicine and Biology* (Zhang *et al* 2011).
- **Chapter IV:** This chapter describes an application of the hybrid simulation technique for CBCT: System design. Simulation offers an opportunity of exploring the current system beyond its provided design. Explorations may focus on the exposure setting, the image acquisition geometry as well as individual hardware components. This can be a direct way to system optimization. Given the large difference of commercial CBCT systems, the information obtained via such simulation may be of great interest. The application that has been selected in this study focuses on the source structure of a CBCT system, where simulation was conducted to investigate the system performance under different filtration designs, namely flat filtration versus the so-called *bowtie* filtration. For CBCT systems with a relatively small imaging FOV, such as the dedicated head and neck imaging system, simple flat filtration is widely used. It was an unsolved question whether the findings about bowtie filters for larger CBCT systems would remain valid, and if so, which improvement could be achieved. We formulated optimal bowtie dimensions under a given set of presumptions and quantified its influence in terms of the output radiation field, the dose delivered to the object, the distribution of scattered radiation and the quality of reconstructed images. It showed the flexibility and usefulness of the hybrid simulation technique for evaluation of a potential hardware component to CBCT systems, which would have been difficult and even impossible with an experimental approach. This work has been submitted for publication.
- **Chapter V:** This chapter describes an application of the hybrid simulation technique for CBCT: Dose evaluation. For imaging modalities based on ionizing radiation, dose is always an issue to be considered. The dedicated head and neck CBCT often applies reduced imaging FOVs, suggesting a lower patient dose as compared to MSCT. However, a large dose range has been found among the systems that are currently available on the commercial market. This might be due to large differences in the exposure setting. Accurate determination of dose distribution, therefore, is beneficial for optimization of the imaging protocol, where the patient dose and image quality can then be better balanced. In the past, dose information solely relied on physical measurements using different types of dosimeters and phantoms. This is difficult in practice because the phantom and dosimeters are both cost-prohibitive and the measurement is usually accompanied with a large uncertainty. Furthermore, to obtain the patient dose information for a variety of CBCT systems and exposure settings would be rather labor-intensive. In comparison, the computer simulation approach offers better flexibility and convenience for dose calculations under different exposure setting and with different computational phantoms.

This study reports a systematic dose evaluation that was performed with the previously developed CBCT simulation model. This work has been submitted for publication.

- **Chapter VI:** This chapter describes an application of the hybrid simulation technique for CBCT: Image quality. Scattered radiation had been recognized as a major source of image artefacts in CBCT. The studies reported in this chapter make use of the simulation for (1) determination of the scatter-induced image artefacts and (2) the correction of scatter signals prior to image reconstruction. The first part looked into the *central artefact* which is commonly seen in CBCT with an offset scanning geometry. We evaluated a hypothesis that such artefact is caused and only caused by the rotationally asymmetric distribution of scatter. Since the simulation offers the opportunity to predict the scatter distribution, this question was able to be answered with a simple experiment. The second part of the study focused on the scatter correction strategy. For many CBCT applications, it has been shown that the Monte Carlo simulation technique can be used to retrieve the scatter data from real patient images on a projection-by-projection basis, which enables effective scatter correction prior to image reconstruction. However, this method requires full patient information from the initially reconstructed 3D image. For CBCT with limited imaging FOVs, the complete image is not available. This study explored an approach to restore the volume of the patient from the truncated 3D image. We proposed an approach based on the image registration technique and a standard patient model. Part A and B have been published and submitted for publication with *Proceedings of SPIE*.

Chapter

II. Preliminary Study

II.A. Introduction

Development of computational models for small experimental animals, such as for rats and mice, is of particular interest with their widespread application in preclinical studies of nuclear medicine. Monte Carlo technique for radiation transport simulation coupled with properly structured phantoms, for instance, has become a commonly adopted approach to estimate the 3D dose distribution in support of evaluating the therapeutic effects of various radionuclides (Konijnenberg *et al* 2004, Stabin *et al* 2006, Bitar *et al* 2007, Peixoto *et al* 2008). Models of favorable anatomical designs are also helpful for performance investigation of small animal imaging modalities and in virtual dissection researches.

Three categories of phantom representation models have been reported in the literature: mathematical, voxel-based and boundary representation. Mathematical phantoms—or, namely, the stylized phantoms—have both their internal organ shapes and exterior contours defined by geometric equations, such as in form of planar, cylindrical, conical, elliptical, toroidal and spherical surfaces. These simplified objects are usually flexible in spatial alteration but fail to faithfully represent the realistic anatomy, even at the cost of using very complex mathematical expressions (Peter *et al* 2000, Han *et al* 2006). Voxel-based phantoms, of which the development is attributable to fast computers and modern medical imaging techniques, are represented via 3D matrices of organ- or tissue-specific volume elements segmented from computed tomography (CT), magnetic resonance (MR), cadaver cryosectional images, etc. Preservation of the anatomical realism with respect to original samples relies on accurate segmentation work that is always labor-intensive and could be rather difficult in case of low-contrast modalities. Furthermore, voxel-based phantoms are severely limited in their ability of geometric transform, except for directionally uniform scaling on voxel size (Caon 2004). On the contrary, nonuniform rational B-spline (NURBS), as a powerful boundary representation tool, has been widely applied in 3D computer graphics to accurately describe the boundary shapes, even with rather intricate structures, and is capable of a rich set of spatial operations. The corresponding surface models, which may sometimes be combined with solid objects as in so-called *hybrid* phantoms, are therefore capable of maintaining the advantages on geometric flexibility and anatomical realism simultaneously. This technique has been successfully utilized in development of both human and small animal models. Segars *et al* (2004) developed a four-dimensional (4D) NURBS-based cardiac-torso phantom using the CT data from the Visible Human Project and modeled its cardiac and respiratory motions. As a direct parallel, a 4D mouse phantom was developed on the basis of high-resolution magnetic resonance microscopy data for molecular imaging research. On whole-body human modeling, Xu *et al* (2007) developed radiation dosimetric phantoms for pregnant females at the ends of three gestational periods. Lee *et al* (2007) developed hybrid phantoms for both the male and female newborns.

For rats, all of the very few available models unfortunately have been either mathematical or voxel-based, until now. Konijnenberg *et al* (2004) developed a general-purposed stylized rat phantom using the measured average dimensions and weights of internal organs on three dissected Wistar rats. Stabin *et al* (2006) used transaxial images of a Sprague–Dawley (SD) rat obtained from a dedicated small-animal CT scanner to model a computational phantom with a voxel resolution of $0.3 \times 0.3 \times 0.5 \text{ mm}^3$. Peixoto *et al* (2008) used CT images of an adult male Wistar rat to model a phantom with a voxel resolution of $0.71 \times 0.71 \times 1.50 \text{ mm}^3$. More recently, a new rat phantom was developed at the Wuhan National Laboratory for Optoelectronics using high quality cryosectional color photographic images of an adult male SD rat with a voxel resolution of $0.02 \times 0.02 \times 0.02 \text{ mm}^3$ (Wu *et al* 2008). Increasingly accurate as the voxel-based phantoms are, numbers of presented local discontinuities, due to either low contrast images or false segmentation, may prevent their extensive use other than in fields of radiation dosimetry and thereby entail the necessity of better representation with enhanced organ boundaries for medical imaging researches.

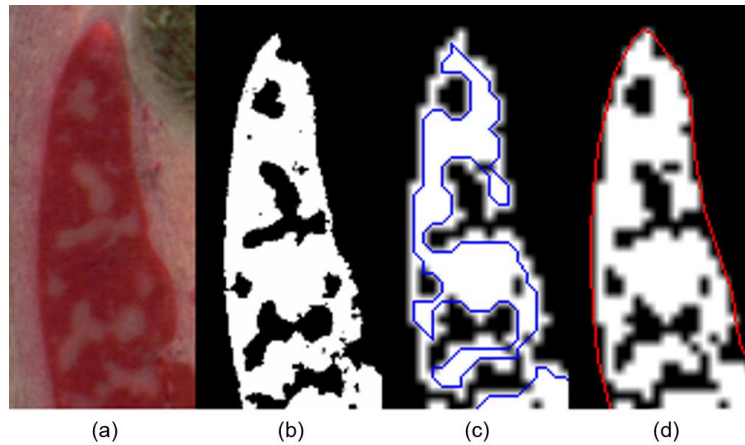


Fig. 2.1 (a) A local area in original color transaxial image containing part of the spleen; (b) semi-automatic segmentation result for spleen in the same region; (c) automatically retrieved spleen contours (in blue) from the downscaled segmentation image; (d) manually rectified spleen outline (in red) used for surface reconstruction.

The objective of this paper is to model a rat computational phantom following NURBS-based boundary representation approach and to demonstrate its usefulness by Monte Carlo simulation for cone beam x-ray CT.

II.B. Materials and methods

II.B.1. Rat anatomical dataset

The transaxial color photographic images for the cryosectioned rat sample, which was 156 g in weight and $42.2 \times 63.2 \times 146.9 \text{ mm}^3$ exclusive of the tail, were previously obtained at a pixel resolution of 2580×4600 with per size of $0.02 \times 0.02 \text{ mm}^2$ and a slice interval of 0.02 mm. Segmentation was performed manually or semi-automatically using ImageJ (National Institutes of Health) for a total of 13 major organs. Specifically, the skin data were approximated as the outermost voxel layer of the outline. Neither the content region for walled structures nor the skeletal marrow distribution was identified at that stage. Initial results were stored on an organ-by-organ basis with 8-bit monochromatic images, in which the target region was highlighted in white and the residual in black. Detailed information for rat sample preparation, sectioning and segmentation has been described by Wu *et al* (2008). In this study, data of the brain, esophagus, heart, intestine, liver, lungs, kidneys, skeleton, spleen, stomach and the newly segmented bladder, testes and thyroids were used, while the skin and muscle data were left out. In order to handle the extremely large amount of segmentation data by currently available computer resources and within an acceptable time frame, only every tenth segmented image was selected, and each was resized down by ten times using a nearest neighbor interpolation method. This process gave birth to a whole-body rat anatomical atlas consisting of $258 \times 460 \times 900$ voxels with per size of $0.2 \times 0.2 \times 0.2 \text{ mm}^3$. In-kind treatments have been frequently adopted in course of fast voxel-based modeling from high-resolution image sets. Considering the size of the rat sample and the absence of segmentation data for tiny structures in this study, such as those in circulatory and urogenital systems, the 0.2 mm voxel resolution should be sufficient to express its anatomical information with only minimal compromise on details.

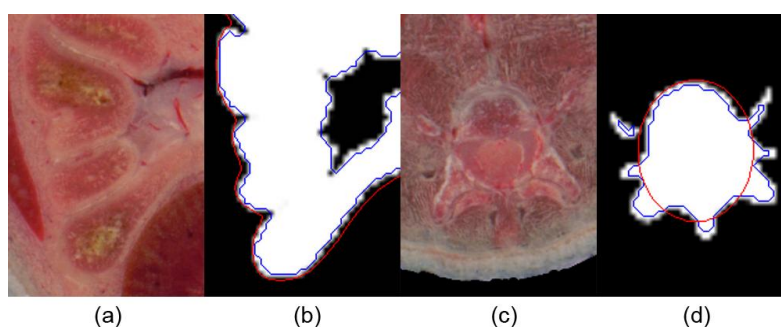


Fig. 2.2 (a) A local area in original color transaxial image containing part of the intestine; (b) comparison of the automatically identified intestine boundary (in blue) with manually outlined boundary (in red) ignoring internal structures; (c) a local area in original color transaxial image containing the spine; (d) comparison of the automatically identified spine boundary (in blue) with that approximated with an ellipse (in red).

II.B.2. Organ surface reconstruction

The 3D organ shapes could be reconstructed from transaxial segmentation data via either volume or surface rendering algorithm, while the latter is important for NURBS modeling since the topological and geometric information is represented all by boundaries. 3D-DOCTOR (Able Software Corp, Lexington, MA), an advanced 3D modeling, image processing and measurement software for multimodality, scientific and industrial applications, was employed to retrieve the boundaries of organs of interest from the segmented images. 3D-DOCTOR is able to automatically identify 2D contours by its built-in interactive segment command and to present the outline curve in form of polygon with many nodes. Due to the limited detectability of the automatic boundary retrieving function as well as the structural complexity on corners, edges and internal breaks of certain regions, manual editing was necessary to correct for any irregular indentation, false looping, self-overlapping and local discontinuities. This operation was greatly accelerated by the multiple node editing tools incorporated with the software. Contour rectification performed on a typical area of the spleen is illustrated in Fig. 2.1.

As shown in Fig. 2.2, special treatments were made on the intestine and small skeletal sites by reason of their complex topology in 3D space. A simplified outermost layer was delineated to define the abdominal portion that is mainly composed of intestine, since its intricate structure was unable to be fully recognized even within the original transaxial images. Bone articulation fragments were mostly united, and the contour of spine in each associated image was approximated with an ellipse that covers the maximum region, by which the ridges were generally disregarded.

Coherent and smooth boundary lines were stacked on an organ-by-organ basis according to the parameter settings specified at initial image calibration for automated reconstruction process in 3D-DOCTOR, where the denseness to generate triangle mesh surfaces should be appropriately configured in order to accurately represent the shape of corresponding organ in 3D space. Since the voxel resolution (0.2 mm) of the selected segmentation data in the study described in this paper was equivalent on all three dimensions, the same value was chosen for all organs along all three perpendicular directions. Figure 2.3(b) exemplifies the reconstructed surface model of the left kidney. Resultant polygonal mesh models were exported in the format of *wavefront object* where all the geometric information was retained.

II.B.3. NUBRS fitting

The polygonal mesh files for each organ were then imported to Rhinoceros (McNeel North America, Seattle, WA), a powerful NURBS modeling software which provides a rich set of tools to create, edit,

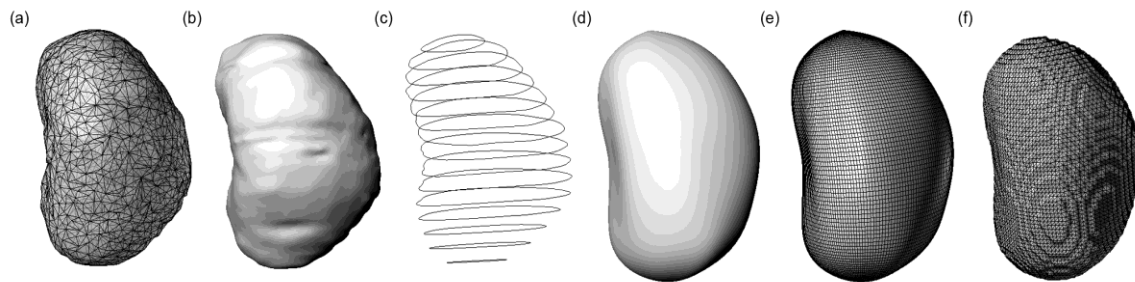


Fig. 2.3 Comparison of the left kidney model in anterior-posterior perspective at different stages (a) the original triangular mesh model at 0.02 mm voxel resolution; (b) reconstructed surface model at 0.2 mm voxel resolution; (c) extracted contours used for generation of NURBS object; (d) NURBS model; (e) re-meshed model; (f) voxelized model at 0.2 mm voxel resolution.

analyze and translate various NURBS primitives. NURBS surfaces could be derived by fitting through the selectively extracted, topologically representative, and closed profile curves of the corresponding polygonal mesh object using the established *Loft* tool of Rhinoceros, the style of which could be more rigid on flat objects but looser on steep boundaries to generate comparatively smooth surface. Procedures of contour extraction and NURBS generation are illustrated using the left kidney in Fig. 2.3(c) and (d), respectively. For organs of complex structures, NURBS fitting was performed separately on different parts, which were determined according to the organ-specific structure in 3D space and could be merged later using the built-in *Boolean Union* function of Rhinoceros. The liver, for instance, was divided into five parts and the entire body outline modeled as a combination of trunk (with head), ears, arms and tail. The same measure was also implemented on the heart and the stomach. Special concern should be given on joint sites between adjacent components since objects sharing no common areas could not be successfully merged by Rhinoceros. The recombined effect of the liver surface model is illustrated in Fig. 2.4, where the partition was not based on the natural leaves of liver but only on its topological features. The content region for simple walled structures, such as for the bladder and the stomach, was approximated in 3D space using the built-in *Scale* transformation tool of Rhinoceros.

II.B.4. Whole-body integration

After all the organ models being carefully prepared, they were to be assembled into the right position within the outline of the entire body, which hereby referred to the skin, in order to generate the whole-body computational phantom. NURBS models for individual organs or organ systems were placed on different layers or sub-layers of Rhinoceros, by which the operation on a certain object could be independent and unaffected to each other. Two important measures need to be stressed at this step:

- 1) The previously reconstructed voxel-based rat phantom at original resolution, in which the organ positions were in precise conformity to the segmentation data, was taken as the gold standard for integration of the individual surface models. Specifically, every effort was made to achieve the largest agreement between the spatial bounding box of NURBS objects and each corresponding voxel model, which were presented in virtual reality modeling language.
- 2) Manual stretching, which was performed by manually manipulating the control points of NURBS objects in Rhinoceros, was implemented on contact regions to compensate the gap between adjacent organs due to the comparatively higher degree of deformation at sharp edges during the lofting process. The resultant spatial information after integration was reported in form of centroid coordinates for each component objects, of which the

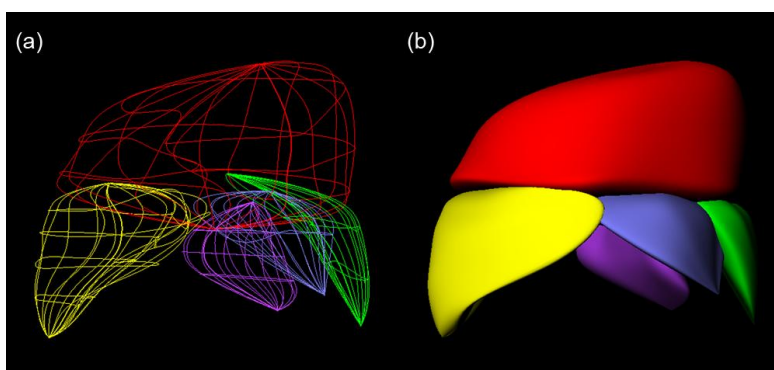


Fig. 2.4 (a) Wireframe view of the liver that was modeled in five separate parts; (b) 3D rendering of the combined liver surface model.

combined centroid for the entire body was intentionally positioned at the origin as a general reference.

II.B.5. Voxelization

Substituting the continuous surfaces with solid geometry as discrete voxels is necessary for phantom definition for Monte Carlo radiation transport simulation, which is one of the most important applications of computational anthropomorphic anatomical models, since the boundary representation geometry could not be fully handled by currently available Monte Carlo systems. All NURBS models, therefore, were re-meshed on an organ-by-organ basis, while the merging of partial surfaces, such as for the liver, was automatically made in between. The denseness of mesh units for each structure should be selected appropriately in accordance with their volume and topological complexity. Normally, tighter mesh leads to higher accuracy with a larger file size, while organs of rather flat appearance require less triangular mesh units to be sufficiently represented. Binvox (Min 2009), a shareware that reads a 3D model file and rasterizes it into a binary 3D voxel grid using the parity voting and ray stabbing methods, was then employed for voxelization. A consistent resolution of $0.2 \times 0.2 \times 0.2 \text{ mm}^3$ was selected for all organs. Taking into account the upper grid limit of 1024 for Binvox and to preserve relative organ positions, a cubic bounding box of $9 \times 9 \times 9 \text{ cm}^3$ was alternately used on the upper and lower part of the rat model, which led to a combined whole-body lattice composed of $450 \times 450 \times 900$ voxels in total. Three-dimensional rendering of the re-meshed model and voxelized model for the left kidney is provided in Fig. 2.3(e) and (f), respectively.

An in-house program was coded in MatLab (MathWorks, Natick, MA) to interpret the raw voxelized information, as exported by Binvox, and to integrate the voxel group for each organ to the final computational phantom. All the residual space was regarded as homogeneous soft tissue, the majority of which was estimated to be muscles and fat.

II.B.6. Monte Carlo implementation

The resultant computational phantom was imported in a general-purpose cone beam CT simulator that was developed using EGSnrc Monte Carlo system (Kawrakow *et al* 2009) for arbitrary 3D voxelized geometry, precisely synchronized gantry rotation and simplified flat panel detector design. The irradiation source was simulated beforehand using the BEAMnrc code (Rogers *et al* 2009) of the EGSnrc system for an X-ray generator with an anode target of Mo at 10° , filtration of 0.5 mm Be plus 0.025 mm Rh and a constant tube potential of 30 kV. A so-called *phase-space* scoring plane was placed against the collimators, on which a total of 6,968,373 photons were obtained within 500 million primary histories of impinging electrons. Each particle was transported 10 times in the follow-

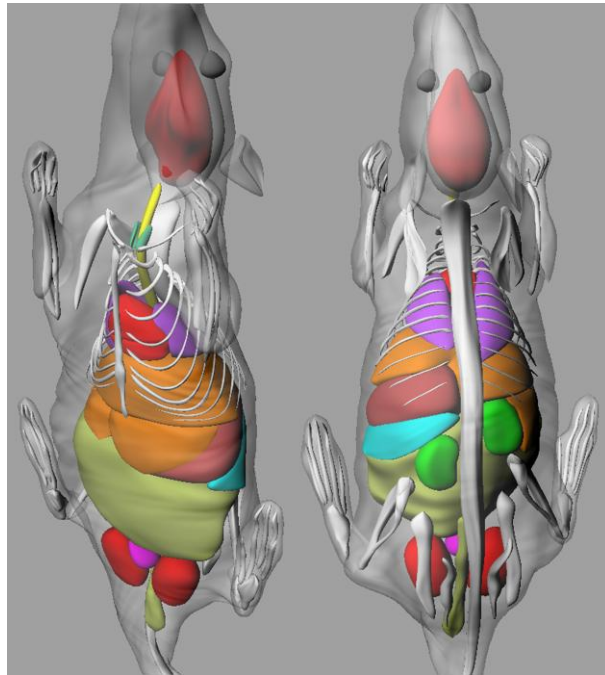


Fig. 2.5 3D rendering of the rat surface model in two perspectives.

up projection simulation to achieve a satisfactory level of statistical uncertainty. Physics treatment and variance reduction settings all across the simulation process were configured in accordance with the developers' suggestions. Geometry of the x-ray tube and cone beam volume imaging unit was constructed in partial reference to information provided by the manufacturers. Organ densities and elemental compositions defined for the rat phantom were based on (ICRU 1989). The density correction data was included for all available materials (ICRU 1984). Photon cross-section files were prepared using the XCOM library (Berger *et al* 2010). Cutoff energies of 0.01 and 0.521 MeV for photons and electrons, respectively, were set to speed up the simulation. Detailed information on the Monte Carlo cone beam CT simulator is to be reported elsewhere.

II.C. Results and discussion

II.C.1. Rat computational phantom

Visual inspection is a straightforward way to check the fidelity of the whole-body geometry with respect to the realistic rat anatomy. Figure 2.5 shows 3D views of the integrated organ surface models in two different perspectives, where the skin and the so-called residual tissue are made semitransparent for better presentation of the internal structures. Despite the simplification on articulations and spinal ridges, it is reasonable to accept the skin and skeleton model as a reliable frame for rat computational phantoms. It could also be observed that the extremely smooth surfaces are rendered for all NURBS models, in which local areas of discontinuities and small points of irregularities or protuberance, due to either low image contrast or false segmentation, have been greatly neutralized. For organs modeled in separate parts, better merging technique might be attempted in the future.

Although it is infeasible to compare positions of individual organs against other rat computational models, by reason of both the considerable morphological difference on original samples and the limited information in the literature, Table 2.1 presents spatial coordinates of organ

Table 2.1 Centroid coordinates and volume for selected organs in the rat phantom.

Organ	Centroid coordinates (mm)			Volume (mm ³)
	X	Y	Z	
Bladder	-2.16	-7.73	-36.76	213.81
Brain	1.01	7.81	58.03	1556.70
Esophagus	-0.67	-1.76	31.56	120.70
Eyeball, left	7.59	9.17	69.41	47.68
Eyeball, right	-3.03	9.06	69.60	47.62
Heart	0.26	-7.77	22.23	734.19
Intestine	-0.87	-3.87	-17.26	15803.86
Kidney, left	5.65	13.25	-11.08	531.90
Kidney, right	-8.67	11.36	-3.55	556.49
Liver	-1.38	-1.39	5.61	9076.54
Lung, left	4.92	-1.25	19.50	787.41
Lung, right	-7.03	0.13	18.44	1134.50
Skeleton				
Skull	1.09	6.67	62.86	3333.39
Spine + Tail bone	2.85	6.55	-14.34	2160.60
Sternum + Ribs + Clavicle	-0.21	-5.44	21.16	248.97
Scapula, left	10.10	2.92	34.28	49.08
Scapula, right	-9.72	2.86	36.04	48.75
Humerus, left	12.70	-5.44	35.22	86.66
Humerus, right	-13.29	-5.21	34.46	73.88
Ulna + Radius, left	18.33	-10.05	32.65	70.86
Ulna + Radius, right	-19.20	-10.79	33.62	82.57
Phalanges, upper left limb	18.06	-9.92	49.42	20.53
Phalanges, upper right limb	-19.18	-10.07	51.77	25.17
Hip bone, left	2.35	8.68	-42.06	125.41
Hip bone, right	-8.79	6.64	-41.60	159.57
Femur, left	7.61	7.52	-35.45	213.89
Femur, right	-11.86	5.87	-34.30	203.91
Tibia + Fibula, left	15.56	3.39	-26.75	150.10
Tibia + Fibula, right	-18.68	-0.83	-23.54	152.08
Metatarsals + Phalanges, lower left limb	27.29	-8.75	-26.43	135.15
Metatarsals + Phalanges, lower right limb	-29.28	-9.80	-24.72	139.87
Spleen	13.39	5.79	-6.70	678.65
Stomach	8.52	-0.04	-1.25	4580.81
Testicle, left	5.04	-6.01	-42.30	903.68
Testicle, right	-9.47	-6.15	-42.76	913.65
Thyroid gland	0.77	-6.23	40.77	17.71

centroid, with the origin located in the center of the body, x-axis facing left, y-axis running through ventral to dorsal side and z-axis pointing to the head on longitudinal direction. This information might be helpful to radiation dosimetry investigations since the dose is always sensitive to the in-body depth and organ-to-organ distance.

As explained above, the organ volume could have been changed in several procedures: polygonalization of the organ surfaces from the contours in selected transaxial images, NURBS derivation from the polygonal mesh surfaces, manual adjustment of organ shapes in process of whole-body integration, re-meshing of the NURBS objects before final voxelization and voxelization at a specific resolution. A little program was coded in MatLab for volume calculation by pixel

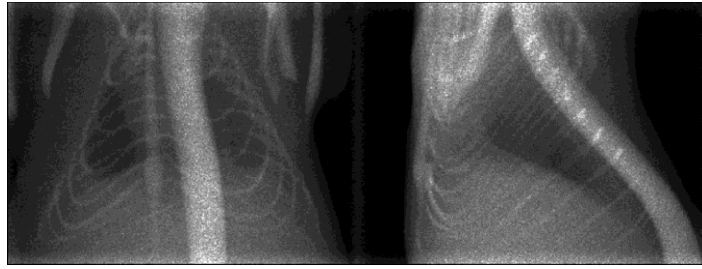


Fig. 2.6 Raw images of the simulated projection at two different angles.

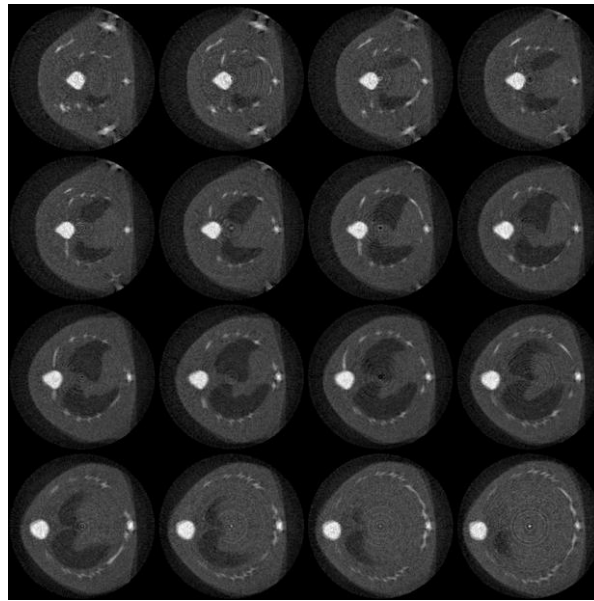


Fig. 2.7 Reconstructed images of cone beam x-ray CT simulation using the rat computational phantom.

counting on the used 2D segmentation data in order to quantify the volume variation resulted in course of surface modeling. An overall volume discrepancy around 10% could be found between the counted volume and that of 3D NURBS models. Considering that the volume of objects that are to be merged by separate parts could not be accurately estimated by Rhinoceros, data for these organs are based on the re-meshed model, of which high polygon denseness was set and the volume deviation with regard to NURBS models remains practically negligible. The difference before and after voxelization is found to be less than 2% for all structures at the 0.2 mm voxel size, which in theory could be voxelized at any resolution. The volume data for organ surface models are also provided in Table 2.1.

II.C.2. Simulated cone beam CT images

A total of 170 cone beam projections were simulated focusing on the thorax region of the rat phantom at equally spaced angles. Pixel resolution of the imaging field was 220 μm . Figure 2.6 presents the raw image data acquired from two typical irradiation geometries. Reconstruction was performed using a filtered back-projection algorithm (Feldkamp *et al* 1984), and the resultant transaxial slices are selectively shown in Fig. 2.7. The smooth and continuous organ boundaries provided by NURBS modeling are of special advantage for high-resolution small-animal imaging

research. Additionally, it has great potential to be applied in imaging modalities where the time dimension is important. The required geometrical transformations can be achieved by matrix multiplication on the set of NURBS control points. However, more information about the organ motion needs to be obtained elsewhere.

II.D. Conclusion

To be both anatomically realistic and computationally versatile has always been a major challenge in development of anthropomorphic models for radiation dosimetry as well as for medical imaging researches. The boundary representation approach by use of NURBS surfaces offers a possibility to combine the advantages on both anatomical realism and geometrical flexibility. In this paper, a NURBS-based rat phantom with 14 major structures has been developed using previously published segmentation data for cryosectional color photographic images of an adult male SD rat. Usefulness of the phantom has been demonstrated by Monte Carlo implementation of x-ray cone beam CT simulation. Presented organs models with smooth surface are suitable for various radiological imaging researches. NURBS models of the rat phantom may be shared with other investigators after contract with the authors.

Chapter

III. Hybrid Simulation Technique

III.A. Introduction

CBCT is a medical imaging technique with increasing applications in diagnostic radiology, image-guided surgery and image-guided radiotherapy. It acquires volumetric data within a single rotation of the paired source and 2D detector, producing a truly isotropic dataset with a high resolution in 3D space (Miracle and Mukherji 2009a). Over the last decade, CBCT has found its way into dental practice as a powerful complement to intraoral radiography and panoramic imaging (De Vos *et al* 2009, Miracle and Mukherji 2009b), in both public hospitals and private clinics. It has greatly influenced strategies in implantology by facilitating the assessment of bone quality and morphology as well as the determination of implant position, size and angle (Guerrero *et al* 2006). The tightly confined x-ray beams with a cone shape result in a more restricted imaging field of view (FOV) and thus a reduced radiation dose compared to conventional CT (Loubele *et al* 2009, Suomalainen *et al* 2009). Over the last few years, there has been a proliferation of oral CBCT models on the commercial market, offering features such as high scanning speed, compact mechanical design, simple operation and a wide range of exposure settings (IDS 2011). Following advances in flat panel detector technology, many current oral CBCT systems are available with imaging FOVs for the entire craniomaxillofacial region.

As a relatively new technique, oral CBCT is still in development of evidence-based guidelines for its sound and safe use (Horner *et al* 2009, HPA 2010a, 2010b). Justification of this modality for replacing classical x-ray examinations and for application in new domains, such as pediatric orthodontics, requires a reasonable balance between radiation dose and image quality. Similar to CBCT in general, methods and tools to investigate and optimize the system performance are of interest, including both experimental and computer modeling approaches. Monte Carlo simulation, for instance, is a generally efficient approach of the latter category that has become popular with the increased availability of powerful computers. It has been adopted in CBCT studies to characterize the radiation field, estimate scatter distribution and calculate doses (Colijn *et al* 2004, Ay and Zaidi 2005, Jarry *et al* 2006, Ding *et al* 2007, 2008, Downes *et al* 2009, Spezi *et al* 2009, Bootsma *et al* 2011). However, CBCT is mainly referred to in radiotherapy or to micro-CT in small animal research and remains very rare yet in oral imaging systems.

A complete simulation chain for CBCT, in theory, should consist of four major parts: the x-ray source, the rotational projection, the detector and image reconstruction. One difficulty in modeling oral CBCT systems is their relatively still closed nature compared to those in other fields. While most reports concern clinical applications, few look into the technical background behind each unique model, setup and parameter. Consideration must also be given to the significant difference in the acquisition geometry, beam quality and the anatomical regions of interest (ROIs). Oral CBCT is dedicated to the visualization of the complex oral and maxillofacial anatomies, mixed with soft tissues, bony tissues and air cavities, thus having specific requirements in terms of image spatial and contrast resolution (Miracle and Mukherji 2009a). These are all relevant when choosing the appropriate simulation techniques. Additionally, a simplified approach was commonly used to model the detector due to the complexity and lack of information on its construction and signal generation processes (Colijn *et al* 2004, Ay and Zaidi 2005, Jarry *et al* 2006, Bootsma *et al* 2011). This might easily over- or underestimate the detector performance, compromising the accuracy of the simulated image quality. Therefore, a better solution is needed.

A hybrid technique is proposed in this study to simulate the entire chain of an oral CBCT system. The simulation model takes into account both dose and image and is flexible for varied exposure settings. Special care is taken to model the non-flat radiation field produced by the bow-tie filter and to include the resolution and noise characteristics of the flat panel detector. Attention is also paid to the time efficiency of associated computational procedures. We first describe the model components and then steps to validate the accuracy of dose, scatter and image simulations by comparison against experimentally acquired data.

III.B. Simulation

III.B.1. Oral CBCT system

The CBCT unit modeled in this study was the 3D Accuitomo 170 (J Morita, Kyoto, Japan), a head and neck imaging system in daily clinical use for oral, maxillofacial and otolaryngological radiology. The flat panel detector has a largest effective area of 748×940 pixels with a pixel size of $254 \times 254 \mu\text{m}^2$, i.e. $\sim 190 \times 239 \text{ mm}^2$ (height \times width). No anti-scatter grid is used. The focal spot to rotation axis distance (FAD) is 540 mm, while the detector has two positions (FDD): 744 mm or 842 mm apart from the focal spot. This yields two magnification factors: 744:540 or 842:540, depending on the selected imaging FOVs. The FOV is provided with nine options, corresponding to cylindrical volumes between $40 \text{ mm} \times 40 \text{ mm}$ and $170 \text{ mm} \times 120 \text{ mm}$ (diameter \times height), which for convenience will be denoted as $\text{FOV}_{\text{Diameter} \times \text{Height}}$ throughout the text. The radiation coverage is always symmetric, i.e. the central beam runs perpendicularly toward the exact center of the detector. The paired source–detector movement and the radiation exposure are continuous, i.e. no gap for data readout between adjacent projections. The system can operate in four modes: Standard, Hi-Speed (fast scanning), Hi-Fi (high fidelity with a larger number of angular projections) and Hi-Res (high spatial resolution). These choices relate to different acquisition parameters and outcome image qualities, allowing for patient-specific imaging protocols. With standard mode, the reconstructed image resolution, in terms of voxel size, is up to $80 \mu\text{m}$ for $\text{FOV}_{40 \times 40}$, $125 \mu\text{m}$ for $\text{FOV}_{60 \times 60}$, $160 \mu\text{m}$ for $\text{FOV}_{80 \times 80}$ and $250 \mu\text{m}$ for the remaining FOVs. The system supports both 360° and 180° scanning. In the present study, only the full-circle rotation with the standard mode was considered. The nominal exposure time is 17.5 s with an acquisition speed of 30 frames per second (FPS). The tube voltage can be adjusted in a range from 60 to 90 kV, in steps of 1 kV, and the tube current from 1.0 to 10.0 mA, in steps of 0.5 mA. According to the manufacturer, an exposure setting of 90 kV with 5.0 mA is recommended for adult patients.

III.B.2. X-ray source simulation

The x-ray generator of the Accuitomo system uses a Toshiba D-051 tube (Toshiba, Otawara, Japan). The minimum total filtration, in terms of aluminum-equivalent thickness, is 3.1 mm. Motorized collimator placement is preprogrammed for different opening sizes according to each FOV. Inhomogeneity of the radiation field is obvious and can be easily observed from flood projection images, i.e. images acquired with an open field exposure. The variation of x-ray fluence in the vertical direction can be explained by the heel effect along the anode–cathode axis, while in the horizontal direction a strong gradient due to non-flat filtration is exhibited (Fig. 3.1). Measurements using a Barracuda system (RTI Electronics, Molndal, Sweden) confirmed that the minimum filtration occurs at the center of the radiation field.

The BEAMnrc/EGSnrc Monte Carlo code system was employed to simulate the x-ray generation, filtration and collimation (Kawrakow *et al* 2009, Rogers *et al* 2009). The bound Compton scattering, radiative Compton correction, Rayleigh scattering, electron impact ionization and atomic relaxation were included. The XCOM photon cross section data and the NIST Bremsstrahlung cross-section data were used (Berger *et al* 2010, Kawrakow *et al* 2010). The simulation was speeded up by cutting off the photon and electron transport (PCUT/ECUT) at energy thresholds of 10 and 520 keV, respectively. In BEAMnrc, the random number generator was switched to the RANLUX and the value for boundary tolerance (BDY_TOL) was reduced from 1×10^{-5} to 5×10^{-7} (Ali and Rogers 2008, Rogers *et al* 2009). Other default configurations were kept. These physics settings were maintained across all Monte Carlo simulations in our work unless otherwise mentioned.

The simulation was split into three parts and bridged by so-called phase spaces. Each phase space is a virtual scoring plane defined at a specific position within the simulation model, recording onto an external data file the information for every particle crossing it. In the first part, the angled

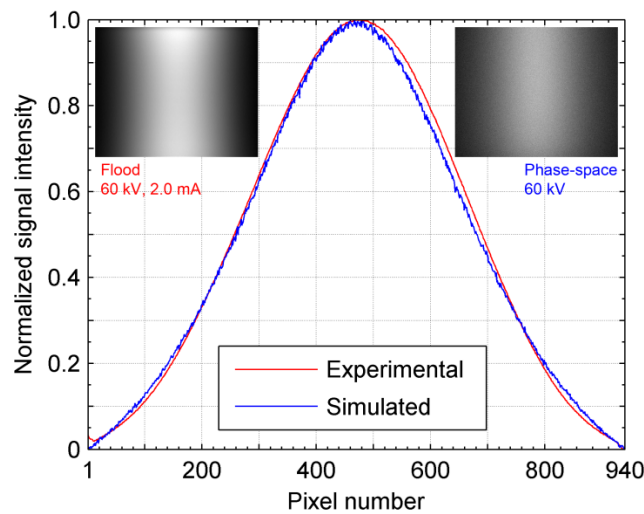


Fig. 3.1 The experimentally acquired flood image (upper left), the flood image derived from the simulated phase space data (upper right) and comparison of the mean horizontal profiles.

tungsten target, focal spot and inherent filtration of the tube were modeled, based on specifications provided by the manufacturer. The tube housing assembly was not included. Two component modules (CMs) available in the BEAMnrc codes—XTUBE and FLATFILT—were utilized. A number of 10^9 mono-energetic impinging electrons were simulated for each selected tube potential: 60, 70, 80 and 90 kV. The simulation efficiency of the x-ray production was increased with the directional Bremsstrahlung splitting (DBS) for a factor of 2×10^3 (Kawrakow *et al* 2004). It was further increased with Bremsstrahlung cross-section enhancement (BCSE) to the anode target for a factor of 200 (Ali and Rogers 2007). The DBS field was set to a radius of 200 mm at a source-to-surface distance (SSD) of 744 mm, which was sufficient to cover the largest FOV. The generated x-ray photons were collected on a phase-space file that was placed directly behind the downstream surface of the flattening filter.

The additional non-flat filter, which is fixed on the Accuitomo unit but pertains to a proprietary bow-tie design, was modeled as follows. With the given minimum thickness of total filtration, the joint effect of the combined absorbers was imitated by modeling one single absorber with dimensions that were estimated iteratively: aluminum was selected as the absorber material; the basic shape was approximated by a rectangle with an elliptical cutout and with the minimum thickness at the center; the 60 kV source phase space was transported by Monte Carlo simulation through the absorber and the resulting particles were output to an intermediate phase space; this phase space was then analytically projected to the detector distance to form a virtual flood image; the intensity profile of this image was compared against that of a real one; the measured discrepancy was used to adjust the exact dimensions of the rectangle and the ellipse; simulations were repeated until the best match was found. The lowest tube potential was chosen because of its stronger attenuation effect compared to the others. Since no CM in BEAMnrc was suitable for such an absorber shape, the simulations were implemented with a specific EGSnrc code developed in-house. The final filtration model accounted for the non-flat radiation field with a relative error $<2\%$ between intensity profiles of the simulated and experimentally acquired flood image, as shown in Fig. 3.1. Due to the DBS method used in the first part, photons of high statistical weights, which were directed beyond the splitting field, were eliminated prior to the simulation. Of note is that the heel effect had already been included in the anode target modeling, so the added filtration in this part accounted primarily for the horizontal

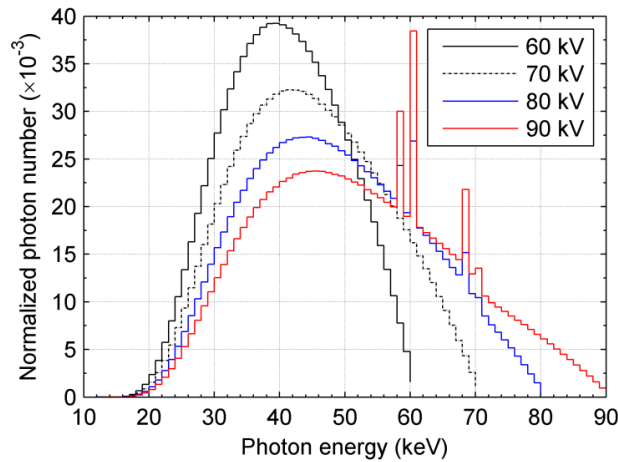


Fig. 3.2 General x-ray spectra derived from the simulated phase-spaces with $\text{FOV}_{170 \times 120}$. Photons are grouped by 1-keV energy bins.

inhomogeneity. The filtered beam data were dumped into a new phase space put against the bottom of the absorber.

The third part of the source simulation dealt with the collimation. Two pairs of lead blockers were modeled using the JAWS CM in BEAMnrc. A thin plastic cover on top of the generator exit was also modeled, for which the FLATFILT CM was used again. The slit was varied in accordance with different FOVs. Owing to the advantage of using the phase space, previous simulations did not have to be repeated. Each tube potential and FOV combination led to a new phase space, on which the photon data were used next in projection simulations. The general x-ray spectra derived from the phase spaces for $\text{FOV}_{170 \times 120}$ with selected tube potentials are shown in Fig. 3.2.

III.B.3. Projection simulation

Cone beam projections were simulated in a step-and-shoot pattern with the source/detector moving over discrete rotation angles. This geometry was integrated with the stationary voxel phantom for the object to be imaged. Irregular 3D voxel array was used to describe the phantom, which allowed much simplification as defining large objects with sparse structural details. The projection simulation was responsible for the primary projection images, scatter projection images and dose estimates. Images were formed at a virtual mesh grid defined at the detector position and with full energy absorption. *Signal Intensity* was interpreted as the accumulated energy of the photons arriving at each element area.

Primary projections were analytically obtained by ray tracing (Siddon 1985), where the original algorithm was slightly modified to cope with irregular voxel arrays of the phantom. Monoenergetic x-rays were directed from a point source at the focal spot position toward the center of each image pixel. Discrete energies with an interval of 5 keV were considered in our calculations. One may of course increase this sampling frequency. The total attenuation coefficients were taken from the NIST database (Hubbell and Seltzer 2004). Each calculated image, normalizing to the initial photon energy, represented a 2D mask for the remaining energy fraction after attenuation.

Given the non-flat radiation field of the CBCT, primary image data have to be merged more carefully than via a simple weighted summation that uses only an average x-ray spectrum. The source phase spaces were further utilized in this regard. First, we mapped the phase space to the detector position to form a flood image. This image was binned at the same energies as in ray tracing. Due to the limited number of photons on the phase space, it led to a stack of noisy profiles. Next, we applied

a Gaussian curve fit to the horizontal direction and a quadratic polynomial fit to the vertical direction for each profile. Maintaining the energy sum, these fitted profiles gave a smoothed variant of the initial flood image and served as 2D modulation templates for the source. The primary image (P) was then assembled as

$$P = \sum_{i=1}^{N_\varepsilon} A(\varepsilon_i) \cdot T(\varepsilon_i) \quad (\text{Eq. 3.1})$$

where N_ε is the total number of energy bins, $A(\varepsilon_i)$ is the 2D attenuation mask at energy ε_i and $T(\varepsilon_i)$ is the corresponding modulation template at energy ε_i . This should be equivalent to the effect of pixel-wise spectrum analysis.

Monte Carlo simulations were conducted to generate the scatter projection images and to calculate the 3D dose distributions. An in-house EGSnrc code making use of the source phase space and carrying out the paired source–detector rotation was developed for this purpose. Dose distributions were tracked on the fly by successively incrementing the dose tags for predefined ROIs, which could be a single voxel or a voxel group. Dose statistical uncertainties were evaluated on a history-by-history basis (Walters *et al* 2002). One primary history refers to one initial electron bombardment on the tube anode target, which might be associated with a series of descendant particles on the source phase spaces by reason of the DBS. Kerma approximation was made to speed up the simulation, i.e. the secondary electrons were terminated in simulation once they were generated and all of their carried energy was assumed to be deposited locally. Dose differences caused by this are negligible because of the short range of electrons in the diagnostic energy regime (ICRP 2007). To obtain good statistics, each particle on the phase space was usually transported more than once before moving on to the next, i.e. recycling.

Particles undergoing scatter were labeled during the Monte Carlo simulation to acquire the image component by scattered radiation alone. Comparing to dose calculation, much heavier recycling of the phase space is needed for images, which would be extremely time consuming. Therefore, the method that combines Monte Carlo tracking with Richardson–Lucy fitting was adopted to accelerate the simulation of scatter projections (Colijn and Beekman 2004). Noisy scatter distribution data (S_0) were first obtained by a coarse Monte Carlo simulation, i.e. using a small number of particle histories or low recycling. The corresponding smooth scatter projection (\hat{S}) was then predicted by Gaussian blurring of a uniform virtual distribution (λ), which was updated in an iterative manner:

$$\hat{S} = G \otimes \lambda \quad (\text{Eq. 3.2})$$

$$\lambda^{(k+1)} = \lambda^{(k)} \frac{G \otimes \left(\frac{S_0}{S^{(k)}} \right)}{\sum G} \quad (\text{Eq. 3.3})$$

Where \otimes stands for convolution, G is the 2D Gaussian kernel, $\lambda^{(k)}$ is the distribution after the k th iteration and $S^{(k)}$ is the intermediate noise suppression by blurring $\lambda^{(k)}$. To speed up the fitting process, the 2D Gaussian convolution was broken down to two successive 1D operations. This algorithm was implemented with 40 iterations for each simulated scatter projection and with a Gaussian width (σ) of 30 pixels for magnification 744:540 and 50 pixels for magnification 842:540 (Colijn and Beekman 2004). The fitted scatter data were added to the primary projection data (P) according to

$$I = P + \frac{\hat{S}}{N_{rc} + 1} \quad (\text{Eq. 3.4})$$

where I is the total image for one projection and N_{rc} is the recycle number of the source phase space in Monte Carlo simulations. Since the signal intensity of the simulated scatter distribution approaches the fitted distribution with the increase of recycling, the division guarantees that the magnitude of

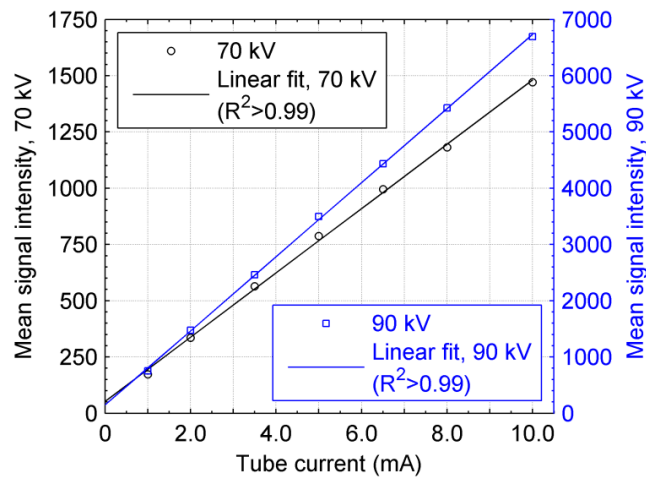


Fig. 3.3 Relationship between the operating tube current and the mean signal intensity in the central area of flood images acquired with additional filtration of a 1.0 mm flat copper plate.

denoised scatter data remains consistent to that of the phase space and thereby also with the primary images.

III.B.4. Detector simulation

The resolution characteristic of the flat panel detector is described by the modulation transfer function (MTF) (Samei *et al* 2006). Methods to measure the MTF of digital imaging devices have been standardized and the slanted-edge technique was adopted in this study (IEC 2003). The measurement assumes a linear imaging system. The linearity of the Accuitomo unit was verified by examining the mean signal intensity in flood images acquired with increasing tube current under a fixed tube potential and exposure time. A flat copper plate with a thickness of 1.0 mm was put against the source exit of the x-ray generator as additional filtration in order to modulate the beam quality as in the presence of a patient's head. Considering the non-flat radiation field of the system, signal intensity analysis was performed on a central area of 256×128 pixels (height \times width), which was approximately uniform. As shown in Fig. 3.3, the linearity of detector response is evident. A small offset of ~ 50 for the pixel values was also observed.

To generate the so-called edge images for the MTF measurement, a square tantalum plate, with machined straight edges, $5 \times 5 \text{ cm}^2$ in area and $< 1.0 \text{ mm}$ in thickness, was taped on top of the detector surface. The plate was placed at the center of the imaging area and with an angle of $\sim 5^\circ$ between the edge and the pixel matrix. A range of tube potentials was used, while the tube current was held at 10.0 mA, as this gave the lowest image noise. Next, a rectangular region of $3 \times 3 \text{ cm}^2$ with the edge approximately at the center was extracted from the image and the pixel value data were differentiated in a direction orthogonal to the edge direction. The angle of the edge was estimated from a linear polynomial fit to the maxima in the gradient image in a least-squares sense. A super-sampled edge spread function (ESF) with a uniform pixel spacing of a quarter of the physical pixel spacing was formed by re-projecting the 2D image data around the angled edge. A median filter of 5 bins in width was applied to the ESF, which was followed by a differentiation operator to form the line spread function (LSF). The Fourier transform of the LSF was calculated and normalized to the zero frequency to give the pre-sampled MTF in 1D. Due to the strong gradient from the bow-tie filtration across the horizontal direction, the MTF was only calculated for the vertical direction. Two options are available to circumvent the difficulty in measuring the horizontal MTF. One is to correct

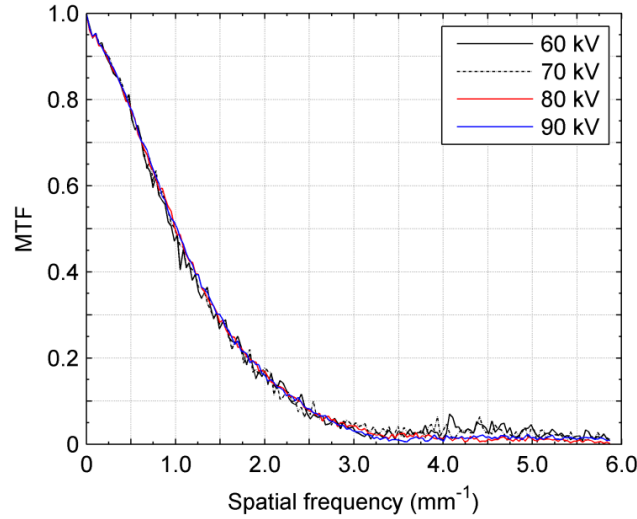


Fig. 3.4 Measured modulation transfer function (MTF) of the flat panel detector of the Accuitomo system.

for the flat field inhomogeneity using the fitted intensity profile from flood images, while the other is to reposition the plate such that the vertical edge lies in the central uniform area. However, only a small difference was found between the MTF in two directions. The data were thus averaged under the assumption of rotational symmetry across the entire detector. Figure 3.4 depicts the MTF curves for selected tube potentials.

Fitting was applied to the calculated MTF such that it can be evaluated at arbitrary points. A model combining three *Lorentzian* functions was used:

$$MTF(f) = \frac{\frac{a}{1 + \left(\frac{f}{b}\right)^2} + \frac{1-a}{1 + \left(\frac{f}{c}\right)^2}}{1 + \left(\frac{f}{d}\right)^2} \quad (\text{Eq. 3.5})$$

where f represents the spatial frequency in units of mm^{-1} and $a-d$ are the fitting coefficients, with $a \in [0, 1]$ and $b, c, d > 0$. The goodness of fit, in terms of the coefficient of determination R^2 , was >0.99 . After extending the 1D MTF curve to the 2D Fourier domain (MTF_{2D}), each simulated projection image (I) was filtered for detector resolution by

$$I' = \mathfrak{F}_2^{-1}(\mathfrak{F}_2(I) \cdot MTF_{2D}) \quad (\text{Eq. 3.6})$$

where \mathfrak{F}_2 and \mathfrak{F}_2^{-1} represent the 2D discrete Fourier transform and the inverse 2D discrete Fourier transform, respectively. These transforms were performed using MATLAB (MathWorks, Natick, MA). It is worth mentioning that the transforms were implemented in a way that the image center always corresponded to the zero frequency in Fourier domain. Till this point, the simulated image remains linear and the pixel values can be freely scaled to match the signal intensity range found in real acquisitions.

Detector noise is characterized by the noise power spectrum (NPS), which was calculated in this study from the flood images using a standardized method (IEC 2003, Dobbins *et al* 2006). Similar to the MTF measurement, the additional copper filter was used in acquiring the flood images. Flood images were first normalized using the detector response curve of the pixel value plotted against tube current. This removed any offset that may have been present in the flood image. The

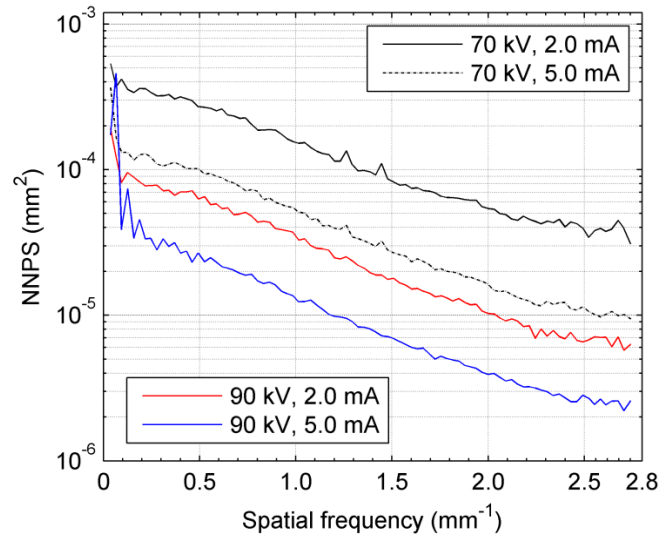


Fig. 3.5 Normalized noise power spectra (NNPS) of the flat panel detector of the Accutomo system.

NPS calculation was based on a central area of 352×352 pixels. To reduce the uncertainty from using a small region, ten consecutive flood images were used. Image correction by quadratic polynomial fitting to the extracted central region was applied in order to further reduce the influence from the non-flat radiation field. Signal intensity (pixel value) data of a floating sub-region of 128×128 pixels were extracted from each projection and the NPS was formed by a 2D Fourier transform. The positions of these sub-regions were half-overlapped across projections by 64 pixels in the horizontal and vertical directions. An additional spatial offset of 16 pixels was applied to the horizontal and vertical coordinates, from which the sub-region was extracted, ensuring that the fixed pattern (structure) noise was different for each dataset in the final NPS ensemble. A total of 20 datasets were included in the NPS ensemble. The 1D NPS was sectioned from the 2D ensemble using a radial average at full spatial frequency. Data from the 0° and 90° axes were included in the NPS estimate. The normalized noise power spectrum (NNPS) was then obtained by dividing the NPS with the squared mean signal intensity from which it was calculated. Error on the NPS was greater at low spatial frequencies as there were fewer points in the NPS. The NNPS calculated for four different exposure settings are plotted in Fig. 3.5. It can be observed that only the scale of the NNPS depends on the exposure setting (beam quality) while the shape is generally invariant. For the radial NPS presented here, the error varied from 11.3% at 0.15 mm^{-1} down to 2.2% at 2.7 mm^{-1} . The NNPS curves can be fitted with the sum of two exponential functions.

The noise properties of the real detector and the quantum noise due to the x-rays were added to the simulated images by adding a noise field (Saunders and Samei 2003, Smans *et al* 2010). To do so, a so-called *colored noise image* was created. More specifically, a 2D Gaussian white noise array with zero mean and unity variance was generated and transformed into the Fourier domain, representing a noise appearance with constant magnitude and random phase. Next, a frequency filter identical to the square root of the NNPS was applied to induce the noise correlation. Back to the spatial domain, the real part resulting from the inverse Fourier transform (\mathfrak{F}_2^{-1}) is the colored noise image (N_c) to be used:

$$N_c = \text{real}\left(\mathfrak{F}_2^{-1}\left(\sqrt{NNPS} \cdot \mathfrak{F}_2(N_G)\right)\right) \quad (\text{Eq. 3.7})$$

where N_G is the 2D Gaussian white noise array. The magnitude of N_c relative to pixel values of the simulated images was determined according to the mean–variance relationship of signal intensities of

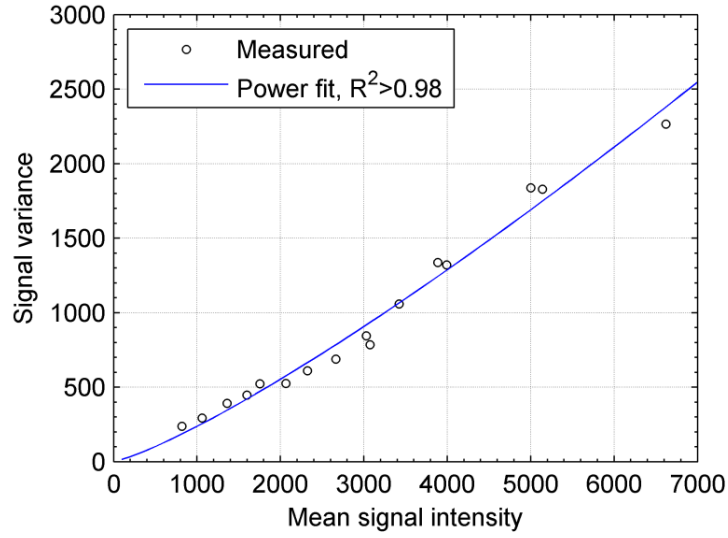


Fig. 3.6 Mean-variance relationship of the signal intensity of the Accuitomo system, measured with different thicknesses of PMMA slabs and aluminum foils.

the system. This information was obtained by examining the central uniform region across a series of projection images acquired with different thicknesses of polymethyl methacrylate (PMMA) slabs and aluminum foils. During a CBCT scan, they were placed about the isocenter, after which the raw image at the most perpendicular angle to the incident plane was extracted for analysis. Proper combinations of PMMA and/or aluminum thickness were made to cover the dynamic range of pixel values. As shown in Fig. 3.6, the Accuitomo system exhibits a power correlation between the mean signal intensity and the variance (σ^2). Noise was then added to each simulated projection image on a pixel-by-pixel basis:

$$I''(i, j) = I'(i, j) + N'_c(i, j) \cdot \sigma(I'(i, j)) \quad (\text{Eq. 3.8})$$

where i and j are the pixel coordinates, I' is the simulated image after inclusion of the MTF, N'_c is the colored noise image (N_c) standardized to zero mean and unity variance and σ is the standard deviation evaluated from the mean–variance relationship in a pixel-wise manner. The standard deviation is numerically equal to the square root of the variance. The resulting image I'' includes the effects from primary attenuation, scattered radiation, detector MTF and NPS and is thereby the final outcome of the image simulation process.

III.C. Validation

III.C.1. Monte Carlo calibration and dose validation

The Monte Carlo dose estimation needed to be calibrated against experimental measurements in terms of absolute dose. To this end, a FC65-G Farmer-type ionization chamber in conjunction with a D-90592 electrometer (IBA Dosimetry, Schwarzenbruck, Germany) was employed. The chamber itself had recently been calibrated, with an air kerma calibration factor (N_K) of $4.555 \times 10^7 \text{ Gy C}^{-1}$ and a flat response over associated beam qualities of the Accuitomo system. Kerma free-in-air was first measured by placing the chamber vertically at isocenter of FOV_{170×120} in CBCT scanning with 5.0 mA and for 60, 70, 80 and 90 kV, respectively. The data ($K_{\text{air,msr}}$) were normalized to product of the operating tube current and exposure time, i.e. in units of $\mu\text{Gy mAs}^{-1}$. Monte Carlo simulations of these measurements were performed next. Only the active end of the chamber (23.1 mm in length)

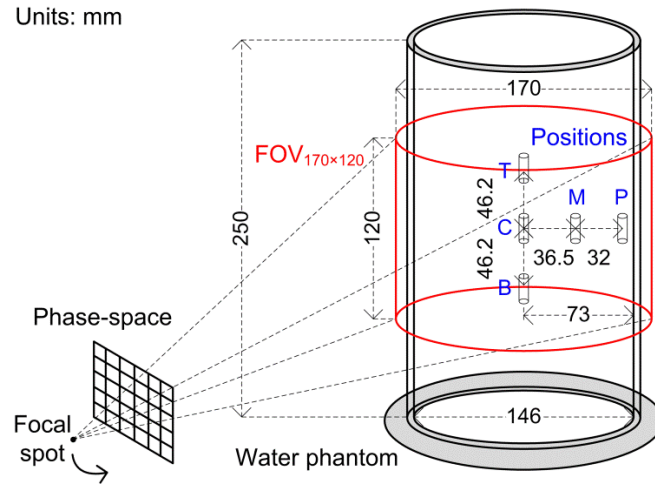


Fig. 3.7 Positioning of the ionization chamber within the water phantom to measure the air kerma in water and to validate the Monte Carlo dose calculation. Five positions—C: Centre; M: Mid-radius; P: Periphery; T: Top; and B: Bottom—are selected with FOV_{170×120}.

was modeled. The basic structure was described by three concentric cylinders, with diameters of 1.0, 6.2 and 7.0 mm, respectively. The first cylinder represented the inner aluminum electrode. The annular space between the first and the second cylinders represented the air-filled volume, while that between the second and third cylinders represented the outer graphite electrode. The Monte Carlo calculated kerma free-in-air ($K_{air,MC}$) were normalized to product of the number of initial primary histories, the number of simulated rotation angles and the transported times of phase space, i.e. in units of μGy per history per angle per transport ($\mu\text{Gy hist}^{-1} \text{ang}^{-1} \text{trans}^{-1}$). The Monte Carlo calibration factor (f_{MC}) was then obtained by

$$f_{MC} = \frac{K_{air,msr}}{K_{air,MC}} \quad (\text{Eq. 3.9})$$

in units of $\text{hist ang trans mAs}^{-1}$. The value of f_{MC} is unique to each simulated phase space.

Dose validation was then performed by comparing the air kerma in water predicted by Monte Carlo simulation against those measured by the ionization chamber. A cylindrical acrylic water phantom, 250 mm in height and 152 mm in diameter, was used. The CBCT scanning was performed using FOV_{170×120} with 5.0 mA and for 60, 70, 80 and 90 kV, respectively. The phantom was placed about the isocenter such that the entire transversal area was covered by the imaging FOV. The chamber was placed in water at five positions, as illustrated in Fig. 3.7. The reference position is at the center. It is combined with two positions at the same height, one about the midpoint of the radius and the other at the periphery, to reflect the dose variation along the horizontal direction. It is further combined with two positions along the central axis of the cylinder, one near the upper edge and one close to the bottom edge of FOV_{170×120}, to reflect the dose variation along the vertical direction. In measurements, the reconstructed axial images were used to verify the chamber placement. The measured air kerma in water ($K_{air,msr}^{in-w}$) were compared with the estimates (\hat{K}_{air}^{in-w}) for each position and tube potential, which were obtained by applying the Monte Carlo calibration factor to the direct simulation results ($K_{air,MC}^{in-w}$):

$$\hat{K}_{air}^{in-w} = f_{MC} \cdot K_{air,MC}^{in-w} \quad (\text{Eq. 3.10})$$

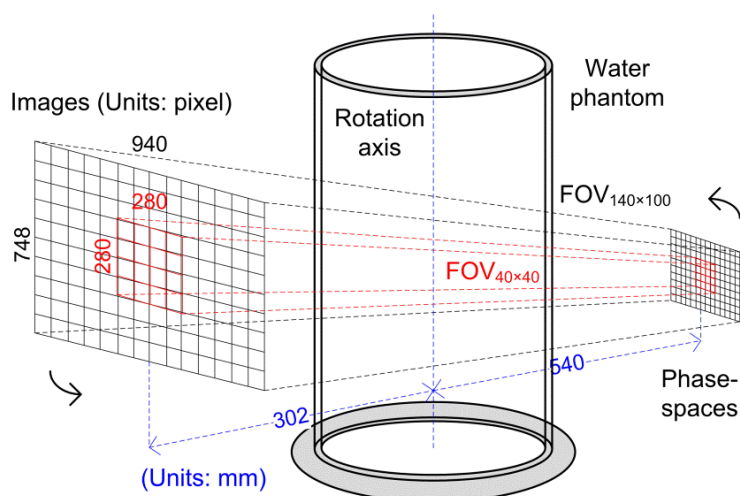


Fig. 3.8 Schematic of the approach used for scatter validation. The difference of signal intensity within the common area of the two FOVs represents the variation of scatter fraction.

where the simulated number of angular projections and phase-space recycle number to obtain $K_{air,MC}^{in-w}$ might not be necessarily the same as those used in calibration.

III.C.2. Scatter validation

Other than direct measurement, an indirect approach was chosen to validate the simulation of scattered radiation. The hypothesis of the validation experiment was that a larger field size increases the contribution of scattered radiation to the projection image, while leaving the primary fraction unchanged under the same exposure setting. The signal in the projection image that results from a fairly narrow beamlet can be regarded as primary-only. Therefore, it seems reasonable to investigate the scatter by comparing images of the same object while the FOV is varied, as illustrated in Fig. 3.8. The greatest FOV difference on the Accutomo system is found between $FOV_{140 \times 100}$ and $FOV_{40 \times 40}$, both of which are with a magnification factor of 842:540. The $FOV_{140 \times 100}$ corresponds to x-ray coverage of 748×940 pixels ($\sim 190 \times 239 \text{ mm}^2$) on the detector, which is the entire active imaging area, while the $FOV_{40 \times 40}$ corresponds to 280×280 pixels ($\sim 71 \times 71 \text{ mm}^2$). The water phantom for dose validation was reused here and imaged under these two FOVs with 90 kV and 5.0 mA. This is the exposure setting recommended for adult patients because the phantom is of comparable size to a human head. No image reconstruction was needed, i.e. the evaluation was performed on projection images. Simulations were carried out with the same geometry and exposure settings. The variation of signal intensities over the common area between $FOV_{140 \times 100}$ and $FOV_{40 \times 40}$, for both simulation and experimental data, were presumed to reflect the differences in scatter only.

III.C.3. Image validation

The Accutomo system is supplied with a set of cylindrical phantoms for use in routine quality assurance (QA) procedures: a contrast phantom and an artefact verification phantom. They were utilized for validation of the simulated image. Both of the phantoms have a diameter and a height of 50 mm. The basic composition of the phantoms is PMMA. The contrast phantom has three cylindrical inserts placed along its central axis, 13 mm in diameter and with different attenuation properties: air, bone equivalent plastic (BEP) and aluminum. The artefact verification phantom embeds a mushroom-like structure made of aluminum. The cap of the mushroom is shaped by a couple of hemispheres that are 9 mm and 10 mm in radius, while the stem by two cylinders that are 8

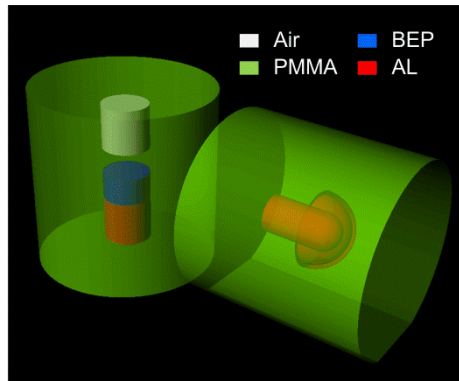


Fig. 3.9 Rendered 3D views of the contrast phantom (left) and the artefact verification phantom (right) delivered with the Accuitomo system.

Table 3.1 Calibration factors (f_{MC}) for Monte Carlo dose estimation. The measured and the calculated kerma free-in-air are about the isocenter with FOV_{170×120}.

Tube potential (kV)	Simulated phase-space		Kerma free-in-air		f_{MC} (hist ang trans mAs ⁻¹)
	Primary histories	X-ray photons	Measured (μGy mAs ⁻¹)	Simulated (μGy hist ⁻¹ ang ⁻¹ trans ⁻¹)	
60	21,950,610	22,623,712	80.428	9.707×10^{-13}	8.286×10^{13}
70	35,399,995	36,923,938	112.808	8.477×10^{-13}	1.331×10^{14}
80	50,978,953	54,676,382	150.653	7.549×10^{-13}	1.996×10^{14}
90	67,802,416	75,392,990	190.581	7.041×10^{-13}	2.707×10^{14}

mm × 10 mm and 19 mm × 20 mm (diameter × height). There is also a 2 mm indentation design on the periphery of the artefact verification phantom such that it can be placed horizontally along the central axis. Rendered 3D views of the two phantoms are shown in Fig. 3.9. Both of the phantoms were placed around the isocenter and imaged under FOV_{170×140} with 70 kV and 2.0 mA. Image reconstruction was accomplished by the software incorporated with the Accuitomo system and for an isotropic voxel dimension of 250 μm.

Next, voxel models of the two phantoms were created and implemented in the projection and detector simulations. The resulting images were compiled into the same format as on the Accuitomo system and were imported to the same reconstruction process. To account for the differences between phantom placement in simulation and experimental acquisition, registration was needed to precisely align the reconstructed images in 3D space. This is conducted using the Insight Toolkit (ITK, Kitware, Clifton Park, NY). A six-parameter Versor rigid transform was used in conjunction with linear interpolation to describe the 3D rotation and translation. The registration was performed in a maximum mutual information (MMI) sense, which is based on evaluation of the joint histograms and independent of the image gray scale. Both the reconstructed experimental and simulation data were registered with respect to a corresponding geometrical drawing of the phantom. The benefit of doing so, instead of direct registration, is threefold: the resulting images were in an ideal geometry, rectified for the nonzero starting angle of the system and the shift about isocenter; the effect of interpolation during transform was comparative to both images; the geometrical drawings could be used as an accurate basis to locate voxels in the resulting images. The MMI metric was important in this regard because the voxels of geometrical drawings were not truly valued.

The Accuitomo system has a built-in automated QA protocol with three checkpoints for image quality assessment: contrast resolution, noise uniformity and artefact. These are represented by the

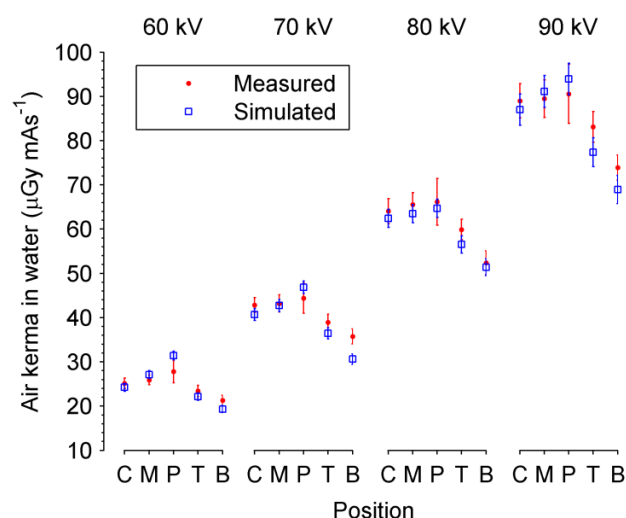


Fig. 3.10 Comparison of the air kerma in water estimated by Monte Carlo simulations and those measured using the ionization chamber. Five positions—C: Centre; M: Mid-radius; P: Periphery; T: Top; and B: Bottom—within the water phantom are considered.

signal difference for insert material regions in the contrast phantom, the signal deviation across homogeneous PMMA in both phantoms and the visual fineness around the mushroom insert of the artefact verification phantom, respectively. The comparison of reconstructed images from simulation data and experimentally acquired data was then carried out in these aspects.

III.D. Results

III.D.1. Doses

For Monte Carlo calibration, the source phase spaces were transported for 72 equally spaced angles over the full rotation trajectory and each recycled nine times. This increased the total number of photons that entered the small volume chamber. The overall statistical uncertainty for the calculated kerma free-in-air, in terms of fractional standard deviation, was <1%. Being situated in a fluent and relatively strong radiation field, the ionization chamber had a stable response with fluctuations <3% during the measurements. The derived Monte Carlo calibration factors for phase spaces with FOV_{170×120} are listed in Table 3.1.

The source phase spaces were transported less in validation simulations with the water phantom, since the photons experienced rich interactions in water and had a higher chance of reaching the chamber. Only 36 rotation angles with recycle numbers of 3, 2, 1 and 0 were simulated for 60, 70, 80 and 90 kV, respectively. The statistical uncertainties for the calculated air kerma in water were <5%. The experimental measurement was conducted five times at each chamber position and for each selected tube potential to obtain the range of deviation. As shown in Fig. 3.10, the relative difference for the Monte Carlo estimated air kerma in water to the measured data is <10% for most cases and the maximum discrepancy is <15%. It can also be observed that Monte Carlo results exhibit a more evident directional variation. This may in part be explained by the fact that simulation always assumed an ideal geometry, i.e. the chamber was modeled exactly at the predefined positions, while the experimental measurement might easily be associated with slight misplacement, although having been verified with the reconstructed images. Considering the low-energy beam qualities for use in oral CBCT that may affect the accuracy of dose measurement in many possible ways, the resulting agreement suggests that the dose calculation with the simulation model can be trusted.

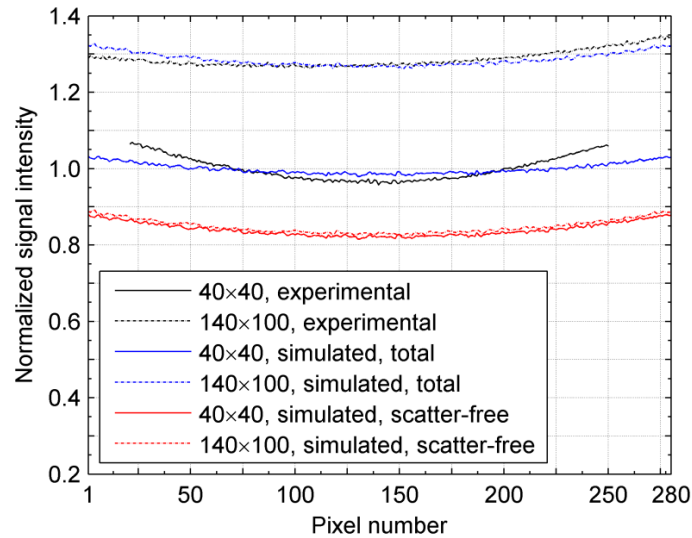


Fig. 3.11 Comparison of the normalized mean horizontal profiles of the simulated projection images and the experimentally acquired images, using a cylindrical water phantom with $FOV_{40 \times 40}$ and $FOV_{140 \times 100}$.

III.D.2. Scatter

In validation of the scattered radiation as a contribution to the image, the 90 kV source phase space was recycled nine times. The normalized mean horizontal profiles for the common area of the acquired projection images under $FOV_{140 \times 100}$ and $FOV_{40 \times 40}$ as well as the corresponding simulation data with and without scatter are plotted in Fig. 3.11. Since the Accuitomo system applies different ranges of pixel value for these two FOVs, the experimental data were first normalized to each corresponding flood images. Next, to rule out the dependence on absolute intensity scale, the experimental and the simulated images were normalized to each corresponding profiles under $FOV_{40 \times 40}$. Partial data close to the edge in the experimental image under $FOV_{40 \times 40}$, which turned out only to be a dark region, were excluded from the comparison. This is due to the fact that the real collimation usually generates a valid exposure area somewhat smaller than the nominal dimensions. A comparable intensity change of $\sim 25\%$ between the two FOVs is shown for both the experimental data and the simulation data, suggesting that the scatter was accurately accounted. The profiles of simulated primary-only data indicate that the scatter fraction with $FOV_{40 \times 40}$ was $\sim 15\%$. As expected, the intensity of primary signals matches well between the two FOVs.

III.D.3. Images

To simulate images with the contrast phantom and the artefact verification phantom, the source phase space for 70 kV was recycled nine times for each projection. One rotation was associated with 512 equally spaced projections. For the contrast phantom, only one angle had to be fully simulated and the rest were all replications because of its strong symmetry in structure. Similarly, projections were only fully simulated over the first 180° for the mushroom phantom. However, the noise distribution was phase-randomized among all projections to avoid any unrealistic bias in creating the appearance. It is worth mentioning that the phantoms in experimental acquisition were padded with loose paper tissues in order to avoid artefacts that might have been induced by the densely structured phantom holder, while the simulation assumed that they were in an ideal geometry of air space. Figure 3.12 shows the reconstructed slices from the simulated images in comparison with those from the experimental images. The images resulting from a simulation with ideal detector performance are

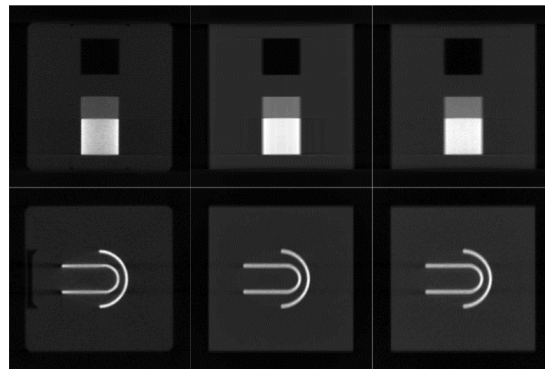


Fig. 3.12 Reconstructed central slices of the experimentally acquired images (left), the simulated images with ideal detector performance (middle) and with realistic detector performance (right) for the contrast phantom (top) and the artefact verification phantom (bottom).

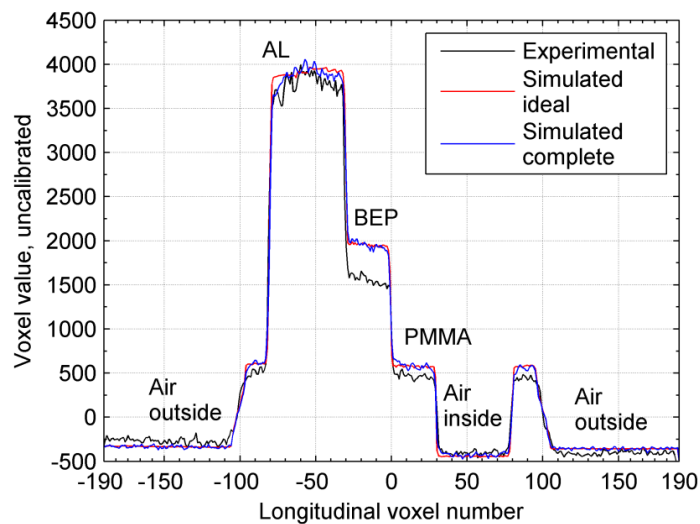


Fig. 3.13 Comparison of the reconstructed voxel values (uncalibrated) along the central longitudinal axis of the contrast phantom for the experimentally acquired image, the simulated image with ideal detector performance and with realistic detector performance.

additionally provided to show the effect of including the resolution and noise characteristics of the detector. Visual inspection of these images side by side shows high resemblance in terms of contrast and artefact pattern, while the detector properties have a big influence on noise appearance and border sharpness. Differences might first be related to the material and structure detail of the phantoms, for which the simulation assumed perfect purity and exact boundary but the real ones may deviate from this. Figure 3.13 shows the profiles of reconstructed voxel values along the longitudinal axis of the contrast phantom. It should be noted that the reconstructed voxel value for the Accuitomo system has not been calibrated as the Hounsfield Units (HU) yet. The relative difference of the mean voxel value was $<5\%$ for the aluminum and air insert regions between the experimental and simulation data. A larger discrepancy ($\sim 20\%$) is observed for the BEP insert region, which may root in the density and composition definition of the BEP material. Specifically, the NIST data for B-100 BEP (Hubbell and Seltzer 2004) were used in simulations while detailed information for real phantoms remains ambiguous. A rather close noise uniformity, in terms of standard deviation across homogeneous PMMA, was obtained by the detector simulation, with a relative difference of $<3\%$ to

the experimental data, which was raised by at least 20% comparing to the simulated data under ideal detector performance.

III.E. Discussion

The simulation model starts from the x-ray generation, modulates the non-flat radiation field, continues with rotational projections, calculates 3D dose distributions, produces primary and scatter images with perfect energy integrating, applies the measured detector characteristics and ends up with a sequence of realistic 2D image data for reconstruction. It is hybrid in several aspects: taking into account both dose and images; splitting the model into the source, projection and detector; combining the deterministic ray-tracing method and stochastic Monte Carlo technique; including the detector characteristics in image simulation; involving different variance reduction and acceleration means. The phase space turns out to be an important utility across the simulation chain.

The source and projection simulation tasks as demonstrated in the present study were split and run on a high-performance computing cluster with *Linux* kernel version 2.6.18 and *GCC* compiler version 4.1.2. With DBS and BCSE measures, the x-ray generation is still the most time-consuming process and produces large-size phase-space data. Fortunately, it has only to be simulated once for each considered tube potential. Subsequent filtration and collimation simulation is much faster, except for the iterative search on non-flat absorber dimensions. This again has to be performed only once. Primary projections are based on the analytical ray tracing, thus can be finished per angle and per energy in a rather short time, namely orders of seconds. The simulation speed for scatter projections is highly dependent on the phantom complexity as well as on the required dose statistics and the smoothness of the scatter distribution. Owing to the scatter acceleration measure, only coarse Monte Carlo simulations are needed. The total time to simulate scatter projection images is therefore not much more than that required by dose calculations. Fitting the scatter distribution and applying the detector MTF and NNPS add no substantial computation time to the entire image simulation chain.

As one of the motivations for this study had been triggered by the need to guide the QA tests for oral CBCT, choosing existing QA phantoms was straightforward, although they have relatively simple structures. More specific phantoms can be useful for further assessment of the detector simulation by use of the measured MTF and NNPS data. The voxel-based phantom geometry was adopted in both the simulation and validation for its convenience in generalization, i.e. can be easily implemented with complex computational anatomical phantoms. Monte Carlo simulations for the dose and scatter estimation were realized separately. First, it was difficult to keep track of the statistical uncertainty for both dose and scatter distributions at the same time. Second, the scatter images were conveniently obtained on a projection-by-projection basis, whereas for dose calculation each particle on the phase space was transported for all angular projections before moving onto the next such that the energy deposition can be grouped into the correct initial history. Additionally, the phantom could have been tailored in particular ways to accommodate the dose calculation scheme, such as implanting a micro-matrix of bone marrow voxels and coding some special subroutines for skeletal dosimetry (Walters *et al* 2009), which would not be needed in image simulation.

Although the resolution and noise properties of the flat panel detector were carefully included, the image signals were produced with perfect energy integrating efficiency, which was a simplification. In theory, it should be possible to simulate the detector in greater detail, i.e. continue the Monte Carlo radiation transport inside of the detector and calculate the dose delivered to each sensor element (Badano and Sempau 2006). Unfortunately, detailed information of the detector is normally unavailable. In this regard, a viable alternative would be estimating the energy absorption based on the thickness of the conversion screen layer and the incident angle of x-ray photons. In modeling the Accuitomo system, this should have little effect on the final image quality because the cone angle is relatively small, let alone any local difference that might have been introduced to the

sparse scatter distributions can be easily smeared out by the fitting process. Apart from this aspect, the detector simulation can be more complicated on larger CBCT systems that are equipped with anti-scatter grids. Full simulation of the radiation transport within the nested grid space is surely feasible. However, ignoring further particle interactions with the grid itself, an analytical direction filtering procedure just prior to the signal detection would be sufficient to model the function of the grid.

Another complication with the detector simulation part is about matching the absolute pixel values. Before applying the detector NNPS, the simulated images remained linear and were manually scaled such that pixel values lay in the same range as those in the real images. This should be equivalent to calibrating the pixel value with measured incident dose at the detector entrance plane, but might not be the case if the linearity of the imaging system had been severely compromised. Moreover, the scaling does not lead to a perfect match with the experimental data and is a further factor influencing the reconstructed image quality.

In determining the bow-tie filter, the flood field profile simulated with ideal detector response was compared iteratively against the measured one, where the normalized intensity curves were mainly used. This approach was only valid on one condition: that the signal intensity in real images stays strictly proportional to the magnitude of incident energy fluence. A dramatic change of the detector gain over 2D, especially to the horizontal direction, would have induced error in the bow-tie dimension established to the simulation model. However, this is unlikely to be the case because the dose calculation results, using the modeled radiation field, also show agreement with experimentally measured data. As for the detector dependence on the energy spectrum, no substantial difference was observed among the normalized intensity curves acquired with different tube potentials, suggesting that its influence on the simulation model was minimal.

III.F. Conclusion

A hybrid technique has been developed to simulate the entire chain of an oral CBCT system and validated in terms of dose, scatter and images. The bowtie filtration was estimated using an iterative approach and the non-flat radiation fields for various exposure settings were mediated via phase spaces. The measured resolution and noise characteristics of the flat panel detector were accounted by filtering the simulated projection images in Fourier domain. The modeled radiation source with different beam qualities was calibrated for Monte Carlo dose calculations. A convenient indirect approach was adopted to investigate the scattered radiation. The QA phantoms delivered with the system and the built-in QA protocols were used to assess the quality of reconstructed images. Overall, the simulation data agree well with the experimentally acquired data, suggesting that the methods used in simulation are valid and the simulation model is accurate. The hybrid simulation technique can be applied to larger CBCT systems as well.

Chapter

IV. Application: System Design

IV.A. Introduction

Bowtie filters are widely applied in current multi-slice computed tomography (MSCT) and cone beam computed tomography (CBCT) to modulate the output of the radiation source (Ding *et al* 2007, Graham *et al* 2007, Mail *et al* 2009, Boone 2010, Menser *et al* 2010). The term *bowtie* applies to a class of filter shapes featuring bilateral symmetry with a thickness that increases with the distance from the center of the radiation field. Bowtie filters compensate for the difference in beam path length through the axial plane of the object such that a more uniform fluence can be delivered to the detector. Owing to this effect, they lower the risk of signal overflow in peripheral detector elements, thus relaxing the requirement on the dynamic range of the detector and allowing better contrast detectability (Beutel *et al* 2000). The use of bowtie filters is known to give a reduction in radiation dose at the periphery of the imaging field of view (FOV) (Graham *et al* 2007, Mail *et al* 2009). They have also been found effective in reducing scatter, a major cause of image artefacts. Furthermore, they have the potential to flatten the scatter distribution, which is beneficial for post-processing scatter correction strategies (Bootsma *et al* 2011). Usually, the thickness of a bowtie filter is variable within the axial plane but stays constant over the third dimension that corresponds to the longitudinal FOV. The large CBCT units for use in image-guided radiotherapy often have different bowtie filters switchable between different exposure settings.

Although the benefits have been well recognized, bowtie filters may not be so useful for systems with a relatively small FOV. In dedicated CBCT of the head and neck, where the FOVs are typically less than 20 cm in diameter, flat filtration is commonly applied (Miracle and Mukherji 2009a). The advantages and disadvantages of bowtie filtration for such systems have not been explored. It therefore remains an open question whether the findings regarding bowtie filters in large CBCT systems are still valid, and if so, what improvements in terms of dose and scatter management can be achieved.

The filters applied on dedicated head and neck CBCT systems are fixed and incorporated within the source assembly, which makes it difficult to assess the effects of different filtration by practical measurement. Computer simulation methods offer a more convenient approach, allowing exploration of parameters for given imaging system beyond its nominal design (Tkaczyk *et al* 2004, Menser *et al* 2010, Bootsma *et al* 2011). In a previous paper, we reported a hybrid technique to simulate the complete imaging chain of CBCT (Zhang *et al* 2011). The current paper describes an application of the hybrid simulation with the objective of modeling a dedicated head and neck CBCT system with only flat filtration, designing and optimizing bowtie filters under a given set of presumptions, and assessing the resulting system performance. We chose to investigate the Scanora 3D CBCT system (Soredex, PaloDEX Group, Finland).

IV.B. Materials and methods

In this section, we first introduce the Scanora 3D system and review the outline of the hybrid simulation technique. Next, the simulation model established with the original flat filtration is described, with a focus on measures taken to cope with the so-called *offset* scanning geometry. Then, we propose an approach to design and optimize bowtie filters. Phantoms to be used for evaluation of the system performance are presented last.

IV.B.1. Scanora 3D CBCT system

The Scanora 3D applies an offset scanning technique, which is implemented nowadays as a solution to the growing demand of large FOVs on the one hand and the cost-prohibitive flat panel detectors on the other hand (Menser *et al* 2010, Wang 2002). It allows the CBCT system to reconstruct a FOV of some nominal volume using a detector of roughly half the size compared to that in a symmetrical setup. In this geometry, the flat panel detector is offset with respect to the rotation axis, such that the

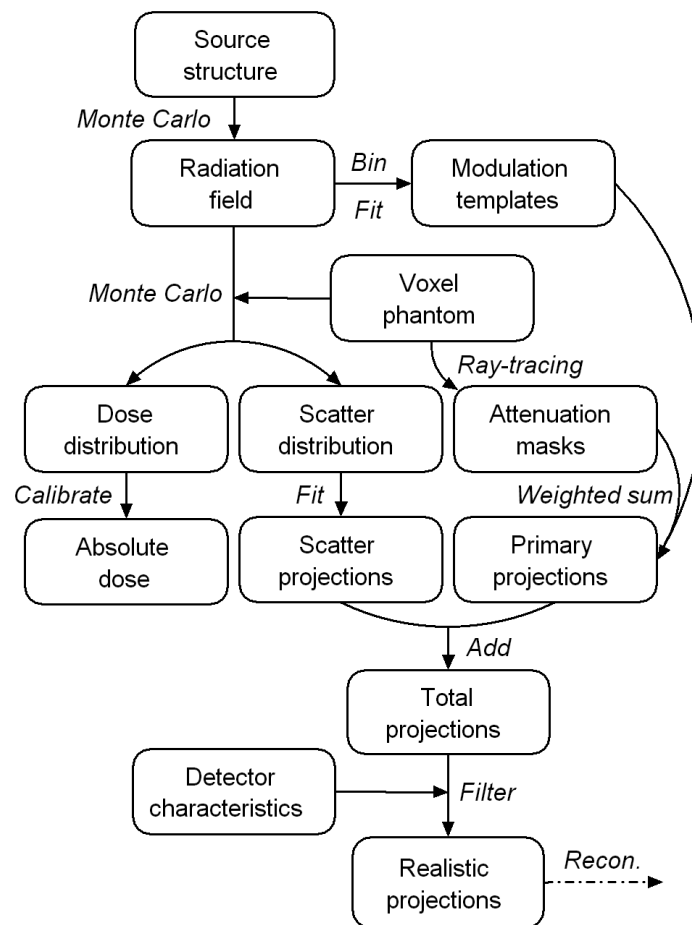


Fig. 4.2 Flowchart of the hybrid simulation technique for CBCT.

IV.B.2. Hybrid simulation technique

The simulation technique accounts for the complete imaging chain of a CBCT system via a hybrid approach (Zhang *et al* 2011). The model starts with the x-ray generation, filtration, and collimation, delivers a cone-beam radiation field, continues with angular projections through a 3D voxel phantom, calculates the dose distributions in pre-defined regions of interest, produces primary and scatter images separately, applies the measured resolution and noise characteristics of the flat panel detector, followed by the image pre-processing procedures, resulting in a sequence of 2D projection data ready for volumetric reconstruction. The flowchart of the simulation is presented in Fig. 4.2. This technique is hybrid by including both dose and image related aspects of the imaging process, splitting the system structure into source, projection and detector, combining deterministic and stochastic methods, making use of the measured detector characteristics as well as different acceleration and variance reduction techniques.

The BEAMnrc/EGSnrc code system was employed for the Monte Carlo part (Rogers *et al* 2009, Kawrakow *et al* 2009). In simulating the radiation source, the so-called *phase space* was used to keep track of the beam dataflow by recording the characteristics of individual photons at selected planes between the tube, the filters and the collimators. The phase space generated after the collimators, i.e. the output phase space, carries all information of the resulting radiation field. We then

derived *modulation templates* by projecting the output phase space to the detector position, binning photon data by energy, and fitting each template in two directions across the detector using polynomials. For the Scanora, the energy bin was set for every 5 keV in this study. Each template represents the photon distribution within the corresponding energy interval. The spatial difference among different templates reflects the variation of x-ray spectrum across the radiation field, which is important when merging the analytically calculated mono-energetic primary projection data (attenuation masks).

The resolution and noise characteristics of the detector were described using the modulation transfer function (MTF) and the noise power spectrum (NPS), both of which were measured using standard methods (IEC 2003). Each simulated projection image was filtered with the MTF and NPS in the frequency domain. The NPS characterized the noise appearance (texture) while the noise magnitude was set pixelwise from the signal mean-variance relationship measured for the imaging system (Saunders and Samei 2003).

Further details about the hybrid simulation technique can be found in Zhang *et al* (2011).

IV.B.3. Simulation model for original filtration design with the offset scanning geometry

The simulation model was first established with the original flat filtration design of the Scanora system. The small rotation of the x-ray tube about the anode to cathode axis, as shown in Fig. 4.1, was handled by tilting up the phase space generated at the tube window with a special source routine of BEAMnrc (Rogers *et al* 2009).

Given the offset scanning geometry and the truncated FOV with respect to the patient size, it is essential that the pixel values near the border of each simulated projection image are accurate, especially at the inner side. Two steps were taken to ensure this. The first concerns the fitting procedure in smoothing the scatter distribution, where the robustness of fitting near the edges of each projection was improved by providing additional data beyond the image border. To do so, the scatter signals were always collected with a sufficiently large detector dimension, namely twice as large as the actual one. The size of the radiation field was kept unchanged, which ensured the scatter distribution was realistic. The fitting was then performed over the large range and the images were truncated to the actual dimension afterwards. The second step concerns the application of the MTF in the frequency domain, an operation equivalent to the convolution of each projection image (in the spatial domain) with the system point spread function. The (unknown) pixel values beyond the image border are important to the accuracy of the convolution near those positions. Therefore, each 2D projection image was padded with void margins before applying the MTF, i.e. pixels beyond the image border were assumed to be zero. The influence of these margins was next compensated in the image pre-processing procedure, where the projection data were normalized against the flood image that had been filtered with the MTF in the same manner.

The image pre-processing pipeline of the Scanora system consists of dark field correction, bad pixel correction, flood field normalization, and logarithm conversion. The first two steps were not needed with our simulation approach. Before being used for normalization, the simulated flood image had to be fitted in both directions to guarantee that no noise was induced due to the limited number of x-rays from the source simulation, since noise was solely determined by the application of NPS. The flood image was also filtered with the MTF, as mentioned above, in order to better cope with the border conditions. Finally, the projection images were compiled into the same format as routine images of the Scanora system for reconstruction using the incorporated software.

IV.B.4. Development of bowtie filters

The principle upon which bowtie filters are designed remains a proprietary technology of the CT manufacturers. It is known that Polymethyl methacrylate (PMMA), Polytetrafluoroethylene (Teflon), aluminum, and copper are commonly adopted materials, while the exact dimension can differ between

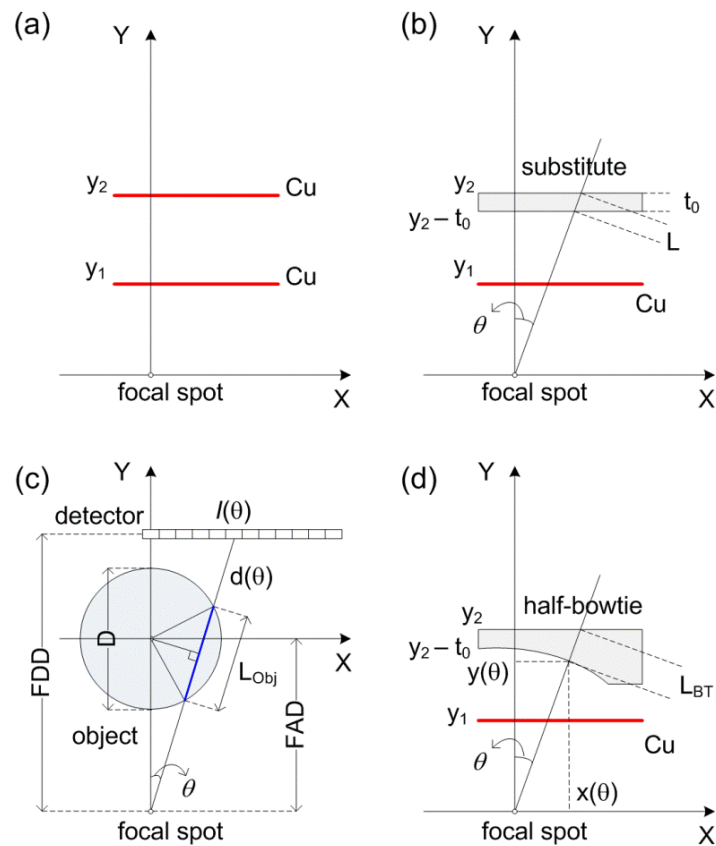


Fig. 4.3 Development of bowtie filter for the Scanora system: (a) positions of the original flat copper filters, (b) substitution of the second copper sheet with an aluminum plate, (c) attenuation by a water cylinder, and (d) variable bowtie thickness.

systems (even for the same manufacturer), depending on the image acquisition geometry and the range of exposure settings. The practical design may have many criteria, including the beam shaping effect, beam hardening effect, dose reduction, scatter management, noise uniformity, contrast detectability, and so forth. Searching for an optimal bowtie filter suggests an iterative procedure with the simulation which evaluates a design criterion or some combination of criteria and adjusts the bowtie dimension until a preset condition is satisfied. Optimizing the noise uniformity in reconstructed images, as suggested in (Wunderlich and Noo 2007), would be one of the aims, but demands exact parameter settings of the reconstruction algorithm. In the present study, we aimed for uniform flux intensity at the detector, with the idea of relaxing the requirement on the dynamic range of the detector. Uniform signal intensity should also lead to uniform noise in the projection image.

Considering the integrity of the original system, the bowtie filter was expected to replace the second added filter, which was originally a 0.1 mm flat copper sheet, while leaving the remaining source structure untouched. As shown in Fig. 4.3(a), y_1 and y_2 represent the distances of the two flat filters to the focal spot in the original design. We restrict ourselves to the axial plane of the FOV. The bowtie filter should reside on $(y_1, y_2]$ with a flat surface at y_2 such that the holder for the second flat filter could still be used. Given the low beam quality and the tube current limitation of the Scanora, copper was not considered a suitable material for the bowtie filter. Furthermore, a less attenuating material would allow easier machining to the desired (variable) thickness and still fit into the available space. Therefore, we first substituted the copper filter with a flat plate of the potential bowtie material

while the output x-ray spectrum should remain the same, as shown in Fig. 4.3(b). To obtain the equivalent substituting thickness t_0 , the phase space generated behind the first copper filter was transported through the plate by Monte Carlo simulation, in which the value of t_0 could be iteratively adjusted.

The offset scanning geometry of the Scanora suggests a *half-bowtie* filter. Let θ be the beam angle with respect to the y-axis, the thickness of the bowtie filter for $\theta \leq 0$ was held constant to be t_0 . To define the dimension for $\theta > 0$, a cylindrical object with diameter D was simulated at the rotation center, as shown in Fig. 4.3(c). Let I be the attenuated beam intensity as a function of θ , then it follows from the Beer-Lambert law that

$$\frac{I(\theta)}{I(0)} = \exp(\bar{\mu}_{Obj} D - \bar{\mu}_{Obj} L_{Obj}(\theta)) \quad (\text{Eq. 4.1})$$

for

$$\theta \in \left[0, \arcsin \frac{D}{2FAD} \right]$$

where FAD is the focal spot to rotation axis distance, $\bar{\mu}_{Obj}$ is the average attenuation coefficient for the object, and L_{Obj} is the beam path length traversed within the object, determined by

$$L_{Obj}(\theta) = 2\sqrt{\left(\frac{D}{2}\right)^2 - (FAD \cdot \sin \theta)^2} \quad (\text{Eq. 4.2})$$

Note that $L_{Obj}(0)=D$. Corrected for the spatial variation of photon fluence according to the inverse square law, Eq. 4.1 becomes

$$\frac{I(\theta)}{I(0)} = \exp(\bar{\mu}_{Obj} D - \bar{\mu}_{Obj} L_{Obj}(\theta)) \cdot \frac{d^2(0)}{d^2(\theta)} \quad (\text{Eq. 4.3})$$

where $d(\theta)$ stands for the total beam path length at θ . That is

$$\frac{I(\theta)}{I(0)} = \exp(\bar{\mu}_{Obj} D - \bar{\mu}_{Obj} L_{Obj}(\theta)) \cdot \cos^2 \theta \quad (\text{Eq. 4.4})$$

The bowtie filter should equalize the attenuation profile such that $I(\theta)$ stays equal to $I(0)$, requiring

$$\exp\left[\left(\bar{\mu}_{Obj} D + \bar{\mu}_{BT} t_0\right) - \left(\bar{\mu}_{Obj} L_{Obj}(\theta) + \bar{\mu}_{BT} L_{BT}(\theta)\right)\right] \cdot \cos^2 \theta = 1 \quad (\text{Eq. 4.5})$$

where L_{BT} specifies the angular length of filtration, as shown in Fig. 4.3(d), and $\bar{\mu}_{BT}$ is the average attenuation coefficient for the bowtie filter. Note that $L_{BT}(0)=t_0$. Rearranging Eq. 4.5 leads to

$$L_{BT}(\theta) = t_0 + \frac{\bar{\mu}_{Obj}}{\bar{\mu}_{BT}} (D - L_{Obj}(\theta)) + \frac{2 \ln(\cos \theta)}{\bar{\mu}_{BT}} \quad (\text{Eq. 4.6})$$

Inserting Eq. 4.2 into Eq. 4.6, L_{BT} is written as:

$$L_{BT}(\theta) = \frac{\bar{\mu}_{Obj}}{\bar{\mu}_{BT}} \left[D - 2\sqrt{\left(\frac{D}{2}\right)^2 - (FAD \cdot \sin \theta)^2} \right] + \frac{2 \ln(\cos \theta)}{\bar{\mu}_{BT}} + t_0 \quad (\text{Eq. 4.7})$$

Coordinates of the bowtie surface can be found by

$$\begin{aligned} x(\theta) &= y_2 \cdot \tan \theta - L_{BT}(\theta) \cdot \sin \theta \\ y(\theta) &= y_2 - L_{BT}(\theta) \cdot \cos \theta \end{aligned} \quad (\text{Eq. 4.8})$$

With Eq. 4.8, it is possible to sample the exact bowtie dimension at discrete θ and fit the curving surface with polynomials. The bowtie thickness to angles beyond the range θ is defined to continue as a plateau.

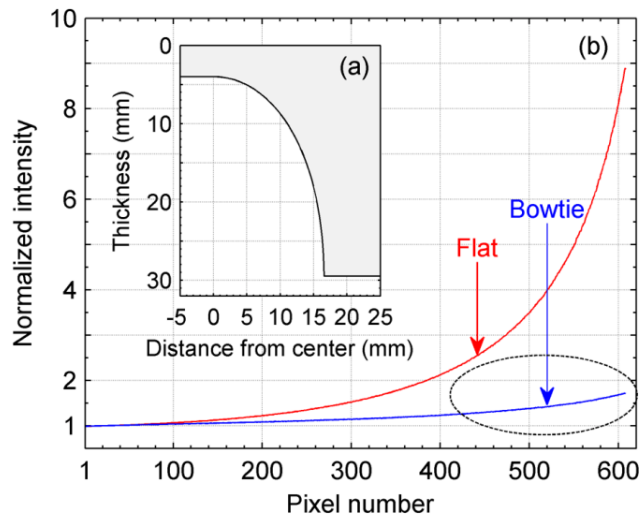


Fig. 4.4 (a) Initial bowtie dimension calculated for $D=16$ cm. (b) Intensity profile with the presence of the object.

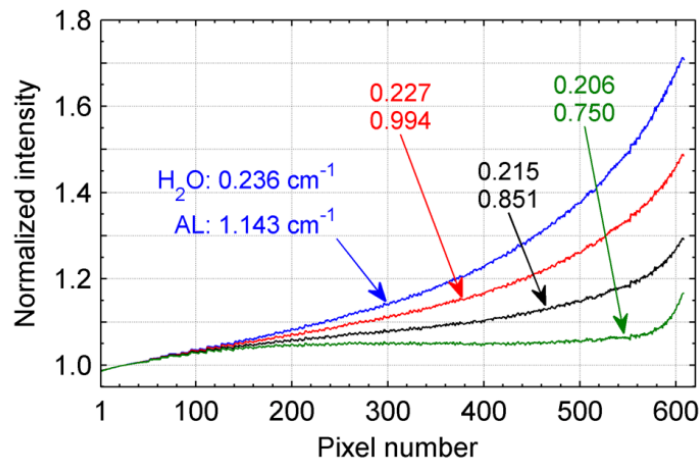


Fig. 4.5 Intensity profiles with the presence of the object in optimizing the bowtie dimension for $D=16$ cm by iteratively correcting the calculated average attenuation coefficient for the object as well as for the bowtie filter.

Choosing aluminum to be the material for the bowtie filter, t_0 was found to be 4.0 mm. The object was assumed to be homogeneous water cylinders, with diameter D approximating sizes of the human head. The values of $\bar{\mu}_{obj}$ and $\bar{\mu}_{BT}$ were first determined by weighting the mono-energetic photon attenuation coefficients with the output x-ray spectrum under the original flat filtration, which were 0.236 cm^{-1} and 1.143 cm^{-1} , respectively. Then, the initial dimension of a bowtie filter can already be calculated for a given D . That for $D=16$ cm is plotted in Fig. 4.4(a) as a function of distance from the central beam. The intensity profile of the corresponding projection image with the presence of the object is shown in Fig. 4.4(b). It can be observed that the bowtie filter manages to flatten the intensity profile, with a reduction factor of ~ 9 approaching the periphery. The slight increase near the outer side is due to the beam hardening effect within the object as well as within the bowtie filter, suggesting an increase of the average beam quality ($\bar{\mu}$) for use in deriving the bowtie dimension. Therefore, the

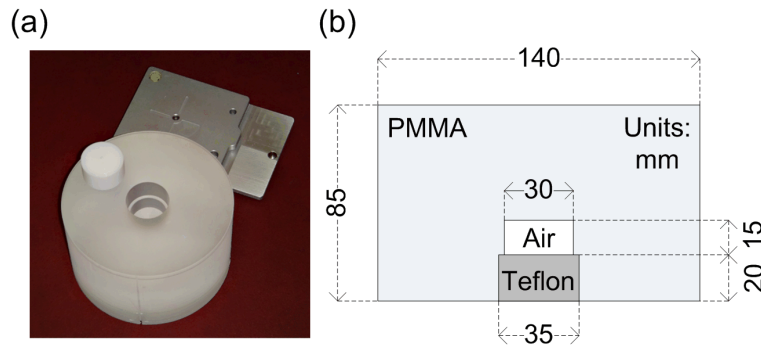


Fig. 4.6 (a) The QA phantom and the phantom holder supplied with the Scanora system; (b) Dimensions of the QA phantom in lateral view.

bowtie dimension was next optimized by iteratively reducing the values of $\bar{\mu}_{Obj}$ and $\bar{\mu}_{BT}$, as shown in Fig. 4.5. In this study, optimization process terminated at $\bar{\mu}_{Obj} = 0.206$ and $\bar{\mu}_{BT} = 0.750 \text{ cm}^{-1}$, when the relative standard deviation of the resulting intensity profile falls below 3%.

IV.B.5. Simulation of bowtie filtration

Since no component module in the BEAMnrc was available for describing the shape of bowtie filters, a separate EGSnrc code for such geometry was developed and integrated within the source simulation model.

The bowtie filter had an Al-equivalent thickness for $\theta \leq 0$ as compared to the original flat filter, i.e., the beam hardening effect remained identical after the substitution. However, the output x-ray fluence may still have been changed. To maintain the output x-ray fluence in the central beam direction, the number of electron bombardments simulated for the x-ray tube had to be increased until the output photon fluence towards the inner side of the projection matched that of the original filtration. This corresponds to increasing the tube current on a real imaging system.

Given the typical size of adult human heads, three bowtie filters were considered in our investigation, with dimensions optimized for $D=14, 16$ and 18 cm.

IV.B.6. Phantoms

Performance of the CBCT system was evaluated by scanning different test phantoms. First, the quality assurance (QA) phantom supplied with the Scanora system was used, a PMMA cylinder with a small cylindrical air cavity and a cylindrical Teflon insert. The dimensions are shown in Fig. 4.6. It was positioned at the rotation center, where the diameter of the phantom completely fits the large FOV. This phantom was used for comparing the experimental and simulated image data for flat filtration and then to assess the impact of bowtie filters. In the experimental acquisition, the positioning is assisted by a specific phantom holder and the positioning lights. In the simulation, phantom positioning was precise because of its ideal geometric setting. To account for any small discrepancy of the phantom placement when comparing the reconstructed images, the experimental image was to be registered to its simulation counterpart with a 3D rigid transform.

In further simulations, two computational anatomical phantoms were used. One was the *Zubal* head phantom made available by techniques described in (*Zubal et al 1994*). This phantom is based on segmented data from transaxial magnetic resonance (MR) images, representing the typical anatomy of the upper half of a human head with 125 identified organs and sub-organ structures. The phantom data were computerized in a 3D array of $1.1 \times 1.1 \times 1.4 \text{ mm}^3$ voxels. Unfortunately, the lower half of the

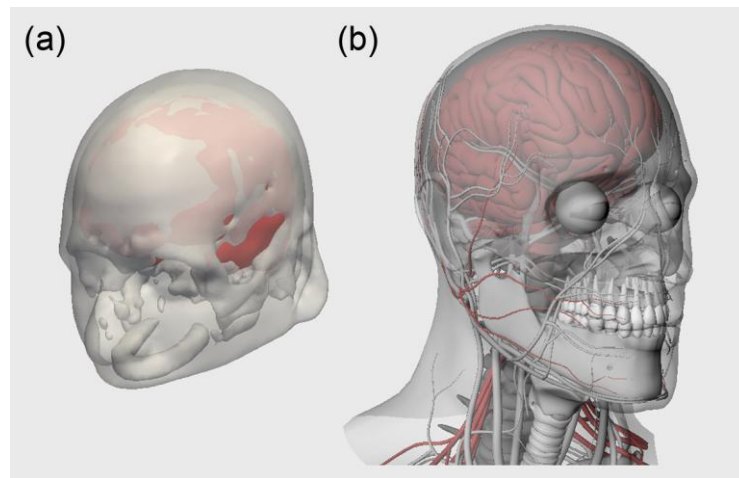


Fig. 4.7 (a) The 3D views of (a) the skin, skull and brain of the Zubal head phantom and (b) the head and neck anatomy of the Plasticboy phantom.

head is not available—a clear limitation of the phantom. To investigate the case of oral CBCT examinations, we employed a so-called *Plasticboy* phantom (Plasticboy Pictures CC 2009), a 3D computer graphics phantom that relies on assembled triangular mesh models to represent the human organ system with a high fidelity. The head and neck part of the phantom was adopted in this study as it has a detailed depiction of the human dentition. The phantom was voxelized with an isotropic resolution of 0.65 mm for implementation with the simulation model. Figure 4.7 provides a 3D view of the two phantoms. Data of mass density and elemental composition for different organs and tissues were taken from ICRP (2002). The large FOV was simulated with a focus on the facial sinus for the Zubal phantom and on the mandible for the Plasticboy phantom.

IV.C. Assessment and results

System performance for different filtrations was assessed in terms of the output radiation field, the dose delivered to the object, the scatter distribution in projection images, and the reconstructed image quality. Interpretations of the results is threefold: comparison between the experimentally measured data and the data simulated with the original flat filtration, which shows the accuracy of the simulation model; comparison between the simulation data for flat filtration and the data for bowtie filtration, which shows the potential influence of bowtie filters; comparison among the simulation data for different bowtie dimensions, which shows the system dependence on the considered range of variations for bowtie dimensions.

IV.C.1. Radiation field

The modulation imposed by the bowtie filters as well as the original flat filter was first examined in terms of the beam shaping effect. This information is represented via the signal intensity profile of the flood field. Figure 4.8 shows normalized mean horizontal profiles of the measured experimental flood image, the simulated flood image with the original flat filter and the flood images simulated with different bowtie filters. It can be seen that the data produced by the simulation counterpart of the original flat filtration agrees well with the experimental data, which in part confirms that the source simulation model was accurate. Some discrepancy can be noted at the outer side of the projection image, which is probably due to slight differences in collimator placement of the Scanora system and their nominal positions used in simulation. As expected, the bowtie filters strongly reduce photon

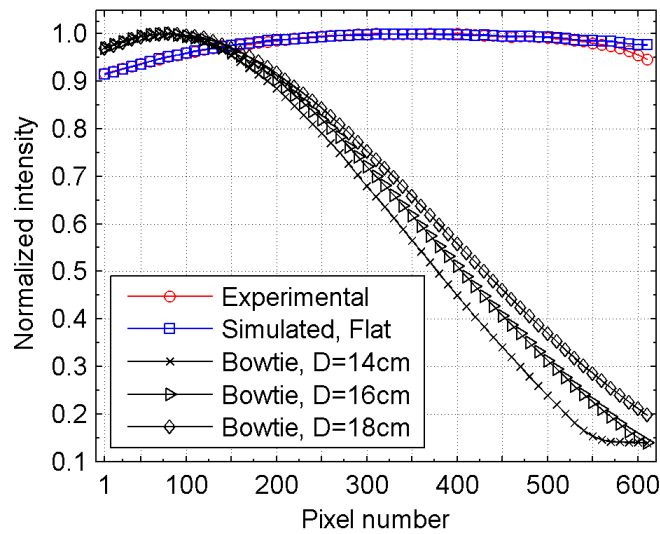


Fig. 4.8 Normalized intensity profile over the horizontal direction for the experimental flood image and the flood images simulated with different filtrations.

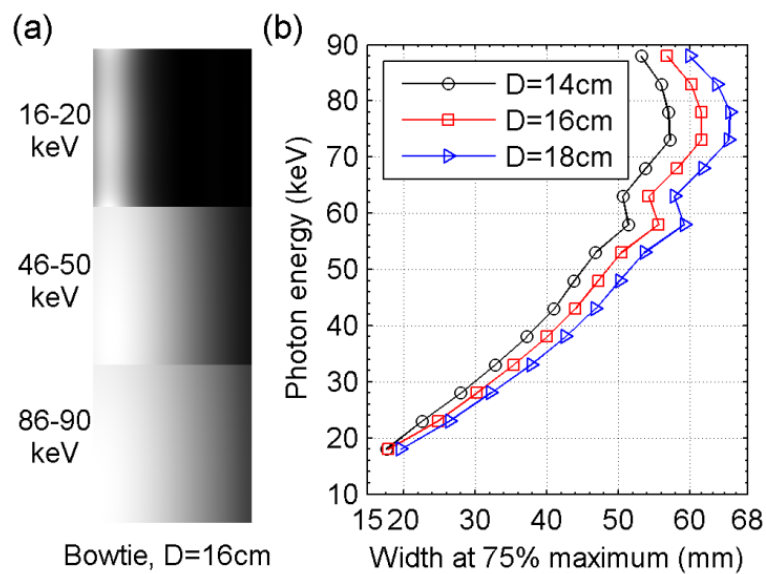


Fig. 4.9 (a) Examples of the photon fluence distribution characterized by the modulation templates for a bowtie filter; (b) Width at 75% maximum of the horizontal profile of the modulation templates at different energy bins and for different bowtie dimensions.

fluence towards the periphery of the FOV. The peak intensity arrives closer to the inner side of the projection with bowtie filtration than with flat filtration. Of note is that about 25 pixels at the beginning of the profile correspond to the overlap region across the rotation axis. With the flat filter, the deviation of the peak fluence from the central beam direction is mainly due to the heel effect. These are open field profiles, without an object in the beam. They may be contrasted with the curve in Fig. 4.4(a) for a simulated scan of a 16 cm diameter phantom, which demonstrates the flattened radiation profile for the bowtie filter case. Dynamic range requirements at the field periphery are reduced by a factor of ~ 5 .

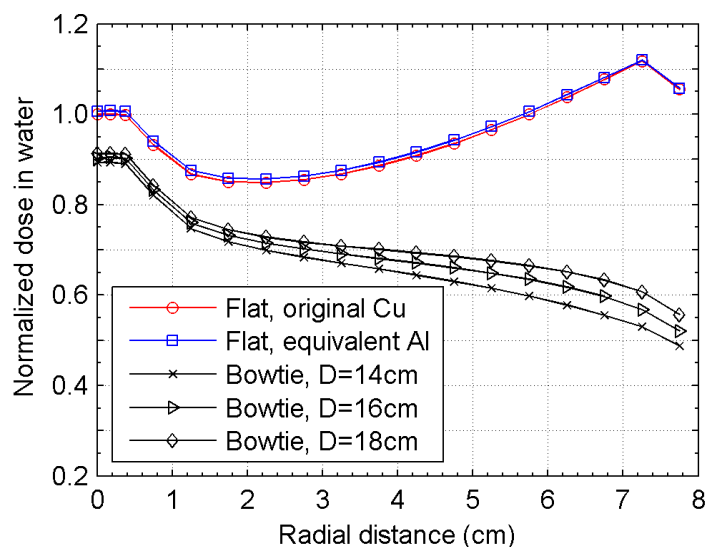


Fig. 4.10 Normalized dose distribution as a function of the radial distance within a 16 cm diameter water cylinder imaged at the rotation center using different filtrations.

The radiation field was next examined in terms of the spatial variation of the output x-ray spectrum. This variation was due to differences in beam hardening effect at different beam angles, which is obvious in case of bowtie filtration. The modulation templates derived from the output phase space are able to characterize the photon distribution as a function of energy at all positions of the flood field. The information contained in the modulation templates is equivalent to that of a pixelwise spectral analysis. Fig. 4.9(a) shows the photon fluence distribution in the flood field at three selected energy bins with bowtie filtration optimized for $D=16$ cm. It can be observed that the gradient over the horizontal direction varies greatly with the photon energy. To evaluate the beam hardening effect in a quantitative manner, the width at three quarters of the maximum of the horizontal profile, $\sigma_{0.75}$, was obtained from the modulation templates for each energy bin and for different bowtie dimensions, as shown in Fig. 4.9(b). The $\sigma_{0.75}$ for the original flat filtration is far beyond the imaging area since the photon fluence profile has nearly a flat distribution. This stresses the importance of accounting for the spatial variation of the spectrum when merging the analytically calculated mono-energetic attenuation masks, as shown in Fig. 4.2.

IV.C.2. Dose

The effect of different filtrations was further examined by investigating the dose distribution. Monte Carlo dose estimates were calculated as a function of radial distance within a 16 cm diameter water cylinder, of height 10 cm, that was positioned along the rotation axis with the bottom 1 cm below the rotation center. Figure 4.10 shows the dose profile averaged over the axial direction for the simulated original flat filtration, the substituting flat filtration, and the bowtie filtration optimized for different D . The data were normalized to the result at the central position under the original flat filtration. The close agreement between the results for the original flat filtration and the substituting flat filtration suggests that the intermediate step taken to replace the flat copper sheet with a flat aluminum plate in developing the bowtie filter was valid. The dose reduction effect by bowtie filters is increasingly prominent from the center to the periphery of the FOV, namely from 8.7% to 53.8%. The reduced dose around the center is attributed to the reduced scatter radiation from the peripheral to the central regions. The difference between different bowtie dimensions is exhibited mainly over the peripheral half of the radius, where the largest difference is 14.6%.

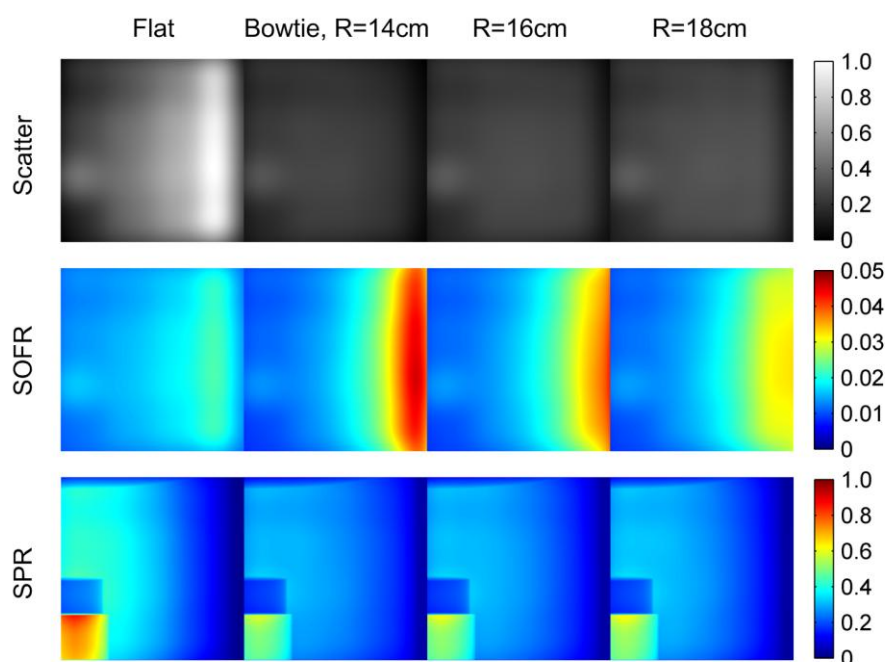


Fig. 4.11 Profile of scatter distribution, scatter-to-open field ratio (SOFR), and scatter-to-primary ratio (SPR) in the projection image of the QA phantom simulated with different filtrations.

IV.C.3. Scatter

The scatter distribution in projection images was assessed via the QA phantom. Figure 4.11 shows the profile of scatter distribution, the scatter-to-open field ratio (SOFR), and the scatter-to-primary ratio (SPR) in one projection of the QA phantom imaged with different filtrations. The scatter distribution was presented by normalizing the scatter signals against the maximum over the imaging area. With the original flat filtration, the scatter signals are stronger near the outer side. On the contrary, scatter distribution was largely flattened by the bowtie filters. The differences for different bowtie filters imply that the bowtie dimension could be optimized in terms of scatter-uniformity while taking into account the size of the object to be imaged. The SOFR was obtained by normalizing the scatter projection image against the flood projection image. Differences are mainly exhibited near the outer side, where the flood intensity is greatly reduced by bowtie filters, and the differences due to different bowtie dimensions are up to 44.3%. The SPR was obtained by dividing the scatter projection image with the corresponding primary projection image. For all types of filtrations, the SPR decreases from the center to the periphery, corresponding to the variation of beam path length traversed by the phantom. The bowtie filters reduce SPR in general, with the greatest reduction near the inner side and for high attenuating regions, namely up to 37.6% for the Teflon insert region. Influence at the outer side is less evident, due to reduced primary signal. For the relatively low SPR near the outer side, the difference among different bowtie dimensions is up to 59.5%.

IV.C.4. Image quality

Reconstructed image quality was assessed with the computational anatomical phantoms as well as the QA phantom. Reconstruction parameters were kept the same as in patient cases. For the QA phantom, the experimentally acquired projection data and the data simulated with flat and different bowtie filtrations were reconstructed for comparison. Figure 4.12 plots the mean profiles over axial planes for

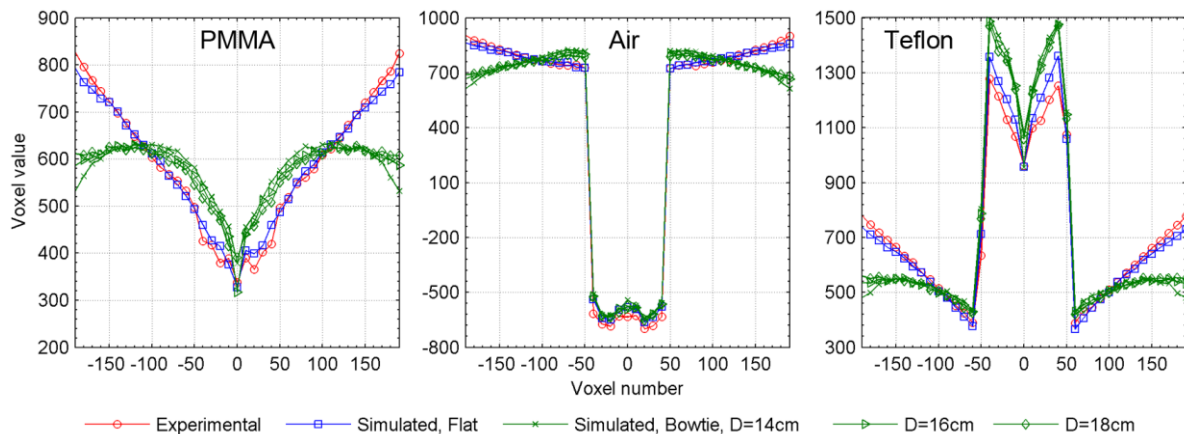


Fig. 4.12 Mean profile at different sections of the reconstructed axial image of the QA phantom under different filtrations.

the homogenous PMMA section, the air cavity section, and the Teflon insert section. Note that the voxel value of the reconstructed image by the Scanora system is not precisely calibrated to the *Hounsfield Units* scale. The agreement between the experimental data and the simulation data for the original flat filtration provides further evidence that the simulation model is accurate. For the PMMA section, it can be seen that the *cupping* artefact is quite strong, with $>50\%$ decrease of the voxel value from the periphery to the center of the FOV. This artefact is mainly due to scatter and the beam hardening effect (Schulze *et al* 2011). The bowtie filtration limits such artefact and flattens the profile, lowering peripheral voxel values by $\sim 25\%$ and raising voxel values in the central half by $\sim 10\%$. It is interesting to note that the bowtie filter optimized for $D=14\text{cm}$, the same as the diameter of the QA phantom, shows slight over-reduction near the edge of the FOV. This is because the QA phantom has a different attenuation property than that assumed in developing the bowtie dimension, which was homogeneous water. The influence of bowtie filtration on the air cavity and the Teflon insert section is also mainly on the surrounding PMMA area, although the voxel value of Teflon is increased by $\sim 5\%$.

Projection data for the Zubal and the Plasticboy phantom were simulated with the original flat filtration and with the bowtie filtration optimized for $D=16\text{ cm}$. Results for the Zubal phantom are shown in Fig. 4.13. It can be observed that the bowtie filtration results in comparable noise appearance, contrast resolution, and artefact pattern to the flat filtration. Qualitatively, the contract-to-noise ratio (CNR) for the selected bony region against the soft-tissue region, as indicated in Fig. 4.13(c), is 7.61 for the flat filtration and 7.88 for the bowtie filtration. Increase in CNR using the bowtie filtration is $<5\%$. Given the favorable representation of the oral anatomy, reconstruction results for the Plasticboy phantom are presented using the panoramic view, as shown in Fig. 4.14. The panoramic images were derived from the reconstructed volume via free-form curve extraction across the axial slices. We chose to place the curve over the jaw bones. Similar results are found. The bowtie filtration reduces the range of voxel values across the image with $\sim 10\%$ lower peak values around the incisors.

IV.D. Discussion

The focus of this study was on computer simulation as this enabled us to investigate an extensive modification to the filtration of a commercial imaging system. For larger CBCT systems as in image-guided radiotherapy, bowtie filtration is an optional exposure setting and the effect has been thoroughly investigated via experimental measurements (Graham *et al* 2007, Mail *et al* 2009).

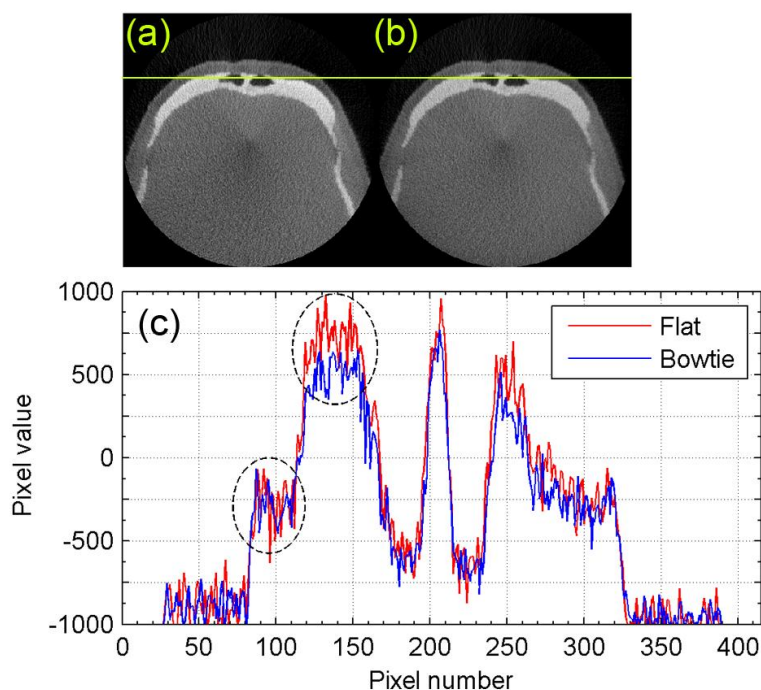


Fig. 4.13 A typical reconstructed axial image of the Zubal phantom with (a) the original flat filtration and (b) the bowtie filtration, and (c) comparison of a selected line profile across the image. The yellow line in (a) and (b) indicates the position of the profile and the dashed circles in (c) indicate the selected region for use in CNR calculation.

Voxel phantoms developed using the segmentation data of medical images are increasingly popular in Monte Carlo-based dosimetry studies. Image simulation, as another important application, usually has a higher requirement on the voxel resolution. As demonstrated in this study, the resolution of the MR-based Zubal phantom showed to be sufficiently fine for use in simulating images. For the oral and maxillofacial complex, the Plasticboy phantom would be a promising choice, where the anatomical models designed solely with computer graphics techniques were assumed sufficiently faithful.

Whereas we have observed specific effects due to the use of bowtie filtration, they could be more evident for larger FOVs. It would therefore be interesting to modify the system at a larger scale by increasing the size of the radiation field, which may give a critical size above which the bowtie filtration should be recommendable. Bowtie filtration has been implemented on some other CBCT systems with similar applications as routinely done with the Scanora. Some systems with bowtie filtration are associated with even smaller cone angles. Therefore, it could also be an interesting simulation study to inversely apply the simulation assessment for these systems, namely to predict the impact of dropping the bowtie filter, replacing it with a flat one, or varying the bowtie dimensions.

There are several limitations to the hybrid simulation model established to the Scanora system when assessing the effect of bowtie filtration. Firstly, the scatter generated within the source simulation model, particularly by the bowtie filter, was not taken into account. A practical solution to tackle this issue would be back-projecting the output phase space towards the focal spot position and labeling the deflecting photons prior to the projection simulation. However, the difference is expected to be minimal, considering the small FOV of the Scanora. Secondly, the advantage of bowtie filtration in relaxing the dynamic range of the detector is difficult to validate, although the flux intensity has been normalized. The exact contribution in this aspect depends on the detector of the actual system,

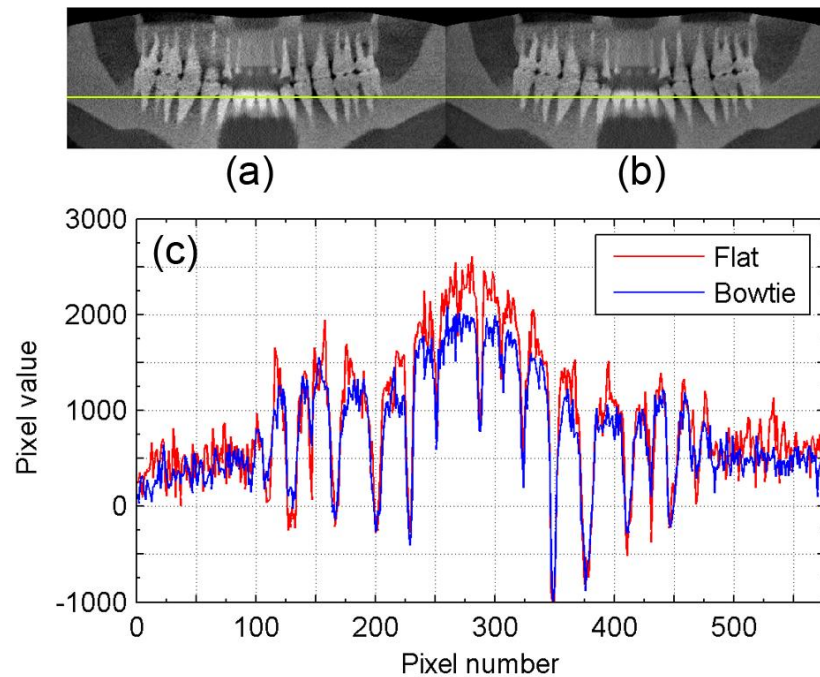


Fig. 4.14 A panoramic view derived from the reconstructed image of the Plasticboy phantom with (a) the original flat filtration and (b) the bowtie filtration, and (c) comparison of a selected line profile across the panoramic view. The yellow line in (a) and (b) indicates the position of the profile.

where more information is needed. Thirdly, the scatter and the primary projection images were collected with a perfect and constant energy absorbing efficiency in simulation before application of the detector MTF and NPS. This may remove part of the modulation effect by bowtie filters. Finally, the reconstruction was conducted using the existing commercial software provided with the imaging system and hence is not designed specifically for use with the projection data acquired under bowtie filtration. The existing scatter correction and artefact reduction measures may conflict with the presence of a non-flat radiation field. A further step would be exploring custom reconstruction for the data considered here, which takes into account the reduced scatter as well as the increased primary signal and noise uniformity. However, investigating new image reconstruction techniques was not considered within the scope of the present study.

IV.E. Conclusion

This simulation study systematically explored the potential use of bowtie filtration for a dedicated head and neck CBCT system. With regard to the offset geometry, Monte Carlo simulation of the radiation field and characterization of the source modulation must adequately cover the FOV of interest. A generally applicable formulation based on normalizing the signal intensity at the x-ray receptor was explicitly given to derive and optimize the dimensions of a bowtie filter. Compared to the original flat filtration, simulation results predicted that the bowtie filtration has a dose reduction of up to 53.8% at the periphery of a 16 cm diameter water cylinder. Even though the FOV was just 140×75 mm, bowtie filtration was useful for scatter management, reducing the scatter-to-primary ratio (SPR) by up to 37.6% for a 14 cm diameter PMMA phantom. The comparable image results found for the computational anatomical phantoms suggest modification to the image pre-processing and the reconstruction for application of bowtie filtration. This hybrid simulation study demonstrated an approach that is useful for exploring and proposing design changes for CBCT systems.

Chapter

V. Application: Dose Evaluation

V.A. Introduction

The introduction of cone beam computed tomography (CBCT) to oral and maxillofacial radiology with dedicated imaging systems has been continuously elevating the use of radiation in this field (De Vos *et al* 2009, Miracle and Mukherji 2009b). Diagnostic imaging used to rely on two-dimensional (2D) modalities, mainly the intra-oral and panoramic radiography, where the associated radiation dose is negligibly low as compared to imaging modalities involving multiple x-ray exposures. For surgeries requiring three-dimensional (3D) image guidance, the conventional computed tomography (CT) was resorted to but this was only performed when it was absolutely necessary. Pediatric patients, for example, were normally kept away from CT. Now, the dedicated CBCT systems provide a relatively easy and convenient access to 3D imaging, thus are widely chosen in clinical practice. While expediting the diagnostic and surgical procedures, they have also drawn a largely increased concern on the radiation risk. Accordingly, massive dose evaluation efforts have been made in justifying the replacement of 2D radiography with CBCT and in comparing the dose delivered by CBCT with that by conventional CT (Ludlow and Ivanovic 2008, Suomalainen *et al* 2009).

For a summary of the dosimetry studies related to dedicated oral and maxillofacial CBCT, the readers are referred to Pauwels *et al* (2012) and the references therein. The reported dosimetric approaches fall in two categories:

1. Make use of the reference quantities, such as the computed tomography dose index (CTDI), the dose-area product (DAP) and the entrance surface dose. These are standardized indicators for the amount of radiation, which can be measured and utilized in combination with proper conversion factors to derive risk-related estimates. The methodologies for such measurements are inherited from the classical radiography and CT, although the feasibility for use in CBCT remains questionable so far.
2. Rely on physical anthropomorphic phantoms loaded with the thermoluminescent dosimeters (TLDs). Since this is a direct way to obtain information that is fairly close to the patient dose, such measurements have been actively carried out and reported in literature over recent years.

However, the complication for oral and maxillofacial CBCT lies in the fact that the dedicated imaging systems are usually provided with a wide range of exposure setting, including the operational tube potential and current, the size and position of the imaging field of view (FOV), the image acquisition speed and resolution, the exposure time and so forth. On the one hand, this has been an advantage in satisfying various case-specific requirements. On the other hand, the dose results and the conclusions based on individual measurements can hardly be useful without taking the exact imaging protocol into account. Systematic measurement would be appreciated, while it implies rather labor-intensive work, especially given the high uncertainty in practice.

The state-of-the-art approach for dose assessment in x-ray imaging procedures is Monte Carlo modeling with computational anatomical phantoms. This technique has been thoroughly investigated in CT dosimetry and is fundamental to patient dosimetry in image-guided radiotherapy (Ding *et al* 2008, Gu *et al* 2009, Lee *et al* 2011). The challenge is to accurately characterize the beam quality as well as the radiation field in establishing the simulation model. The increased availability of computational anatomical phantoms has been an important reason for the widespread application of this approach (Zaidi and Tsui 2009). However, to our best knowledge, it has not been explored for radiation dosimetry in dedicated oral and maxillofacial CBCT. In a previous study, we developed a hybrid simulation technique for CBCT and validated it in terms of dose, scatter and image quality with application to an oral CBCT system (Zhang *et al* 2011). The simulation of the radiation source and a part of the rotational projection simulation are based on the Monte Carlo technique. Flexibility of the simulation model in configuring the exposure setting makes it well-suited for systematic dose evaluation

The objective of this study is to explore the approach of Monte Carlo modeling for dose calculations in dedicated oral and maxillofacial CBCT, to assess the dose distribution and to investigate the dose influential factors. Two very different CBCT systems in daily clinical use were selected for investigation. The simulation model was calibrated with an experimental procedure such that the dose estimates can be correlated with the operational tube load. Special measures were taken in order to accommodate the dose calculation schema, including the organ dose, the effective dose and the dose profile. The calculation was demonstrated using four computational phantoms of the human head and neck and for typical cases of CBCT examination. The results were also compared to the experimentally measured data.

V.B. Materials and methods

V.B.1. CBCT systems

For Monte Carlo dose calculations, the image acquisition geometry, the radiation source structure and the exposure setting of the CBCT system are the most important information for establishing the simulation model. The 3D Accuitomo 170 (J. Morita, Japan) system and the Scanora 3D (Soredex-PaloDEX, Finland) system that are available in the oral imaging clinic of our hospital were chosen for investigation. These two CBCT systems both use the flat panel detector technology but are different in many aspects. The Accuitomo uses a symmetric setup, where the central beam stays perpendicular to the center of the flat panel detector during the scanning. The Scanora employs a so-called ‘offset’ geometry, where the detector is positioned offset to the center of rotation and a large part of the FOV is scanned in only half of the rotation (180° plus the fan angle). The magnification of the object to the projection image is constant on the Scanora but can be different with the Accuitomo. The Accuitomo uses a bowtie filter while only flat filters are used with the Scanora. The Accuitomo offers nine FOVs, ranging from 40×40 to 170×120 mm, denoted as diameter \times height. The Scanora provides three FOVs: 60×60 mm (small), 100×75 mm (medium) and 145×75 mm (large). The tube potential with the Accuitomo is adjustable from 60 to 90 kV while it is fixed to 90 kV with the Scanora. The operating range for tube current is from 1.0 to 10.0 mA for the Accuitomo and from 4.0 to 12.5 mA for the Scanora. Both systems support different scanning modes, in which the exposure time, the number of projections and the reconstructed image resolution can be different. The exposure is continuous with the Accuitomo whereas pulsed with the Scanora. The Scanora provides also an panoramic imaging program and an extended large FOV based on two rotations, which however were not considered in the present study.

V.B.2. Phantoms

Computational anatomical phantoms were used in the simulation to represent the object (patient) undergoing the CBCT examination. We made use of the head and neck part of four voxel-based phantoms in this study:

- The ICRP reference phantoms for adult male and female (ICRP 2009). These phantoms were developed using the segmentation data of CT images. Post-segmentation adjustment was performed to match the reference anatomical characteristics (ICRP 2002). They were intended for radiation dosimetry applications, thus consist of most organs that have been identified as radiosensitive. The voxel resolution is $2.137 \times 2.137 \times 8.0$ mm³ for the male and $1.775 \times 1.775 \times 4.84$ mm³ for the female phantom (coronal \times sagittal \times vertical). It is worth mentioning that the composition of the trabecular bone (spongiosa) is provided with explicit mass ratios of the red bone marrow, yellow bone marrow and mineralized tissue
- The Zubal phantom (Zubal *et al* 1994). This phantom was based on two separate CT scans of the head and the torso of an adult male and was created by attaching the segmentation data of one image set to that of the other, where compression and interpolation were

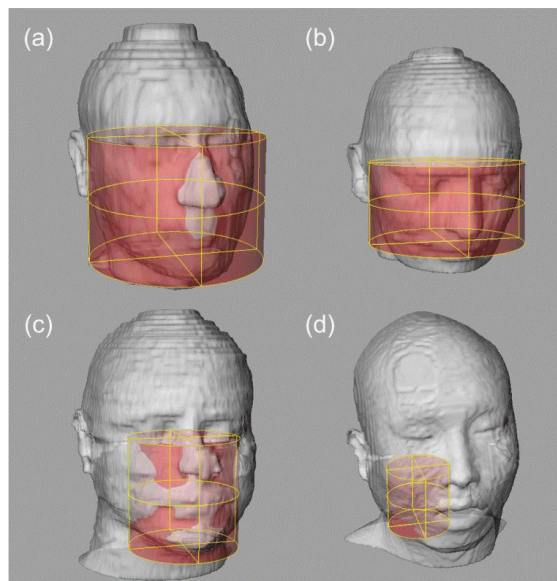


Fig. 5.1 Outlines of the head and neck computational phantoms in 3D with examples of imaging FOVs: (a) ICRP reference male phantom with FOV 170×120 mm, (b) ICRP female phantom with FOV 145×75 mm, (c) Zubal phantom with FOV 100×100 mm and (d) VCH phantom with FOV 60×60 mm.

performed to yield a uniform voxel dimension of 4.0 mm. In this study, we used only the segmentation data of the head CT images, which in fact start from the neck. The original 5-mm slice thickness was preserved and the pixel resolution in plane was adapted from 0.5 mm to 1.5 mm, resulting in a voxel size of $1.5 \times 1.5 \times 5.0$ mm³.

- The VCH phantom (Zhang *et al* 2008). The phantom was developed on basis of the visible Chinese human dataset, where transaxial color photographic images were obtained from successive cryosections of a whole-body cadaveric specimen for adult male. The sectioning interval was 0.2 mm and the pixel resolution of the photographs was 0.1×0.1 mm². Main body structures were segmented manually or using semi-automatic methods. The final phantom was created by resampling the segmentation data to an isotropic voxel resolution of 2.0 mm across the entire body. In this study, the head and neck part of the phantom was used.

It was decided to leave out the shoulders and everything below for each phantom, which would otherwise stand in the rotation trajectory of the paired source and detector. In clinical practice, the patient is normally asked to sit upright with a straight neck and relaxed shoulders. This, however, may not be the case when the phantoms were created. In the present study, the head and neck part was cut from the original phantoms as close as possible to above the shoulders. Figure 5.1 shows the phantom outlines in 3D with example FOVs. It can be seen that the head of the female phantom is lowered too much so a part of the chin had to be dropped with the neck and shoulders. We kept it in this way for the moment and tried not to place the imaging FOV to low in our simulation. Main structures available in the phantoms and the calculated organ masses are summarized in Table 5.1. Sub-organ structures and some organs of similar tissue properties have been merged.

V.B.3. Monte Carlo simulation model

The previously developed CBCT simulation model accounts for the complete imaging chain with a validated hybrid technique (Zhang *et al* 2011). The Monte Carlo part was realized with the BEAMnrc/EGSnrc code system (Rogers *et al* 2009, Kawrakow *et al* 2009). It started from the

Table 5.1 Organ masses (g) of the computational head and neck phantoms.^a

Organ	Ref. male	Ref. female	Zubal	VCH
Blood vessels	0.9	6.1	54.7	42.3
Bone	1308.4	982.3	1464.3	702.0
Cortical	724.4	488.3		
Trabecular	584.0	494.0		
Brain	1449.8	1300.0	1767.0	1061.6
Cartilage	16.0	15.8	98.3	1.6 ^a
Extrathoracic tissue	38.9	17.1	21.9 ^b	94.2 ^c
Eyes	15.0	15.0	21.9	13.1
Fat	1048.4	886.1	44.6	717.2
Lachrymal glands			2.6	2.6
Lymphatic nodes	8.1	3.6		
Muscle	1217.7	402.0	1487.0	550.1
Oral mucosa	35.8	22.4		94.6 ^d
Pituitary gland	0.6	0.6		0.6
Salivary glands	85.0	70.0		87.5
Skin	343.0	185.4	962.0	215.2
Spinal cord	10.2	4.2	28.6	
Teeth	50.0	40.0	62.1	60.2
Tongue	42.3	41.5	50.6	48.5
Tonsils	3.0	3.0		
<i>Total^e</i>	5676.8	3995.2	6092.5	4282.8

^a Only the cartilage around the ears.

^b Only the pharynx.

^c Including the entire larynx, pharynx and nasal vestibule.

^d Represented by the entire gum.

^e Including also the air inside body and unspecified soft tissues.

impinging electrons to the anode target in the x-ray tube, where the nominal focal spot sizes and target angles were modeled. Efficiency of the x-ray production was improved by use of the directional Bremsstrahlung splitting (DBS) in combination with the Bremsstrahlung cross-section enhancement (BCSE). Filtration and collimation were modeled according to the specifications provided by the manufacturers. Dimensions of the bowtie filter applied with the Accuitomo system were figured out via an iterative approach. The beam dataflow across the tube, filters and collimators as well as the final source output was tracked by use of the so-called 'phase space'. The phase space generated at the position the source exit, namely the output phase space, recorded the position, direction, charge and so forth information for every outgoing particle.

The output phase space was next transformed over the source rotation trajectory to form a rotational radiation field. In projection simulation, particles on the phase space were continued for Monte Carlo radiation transport through the 3D voxel phantom. The positioning of the FOV was realized by translating the phantom about the rotation center under 3D guidance as show in Fig. 5.1, where the determined coordinates of the FOV as relative to the phantom were passed to the simulation

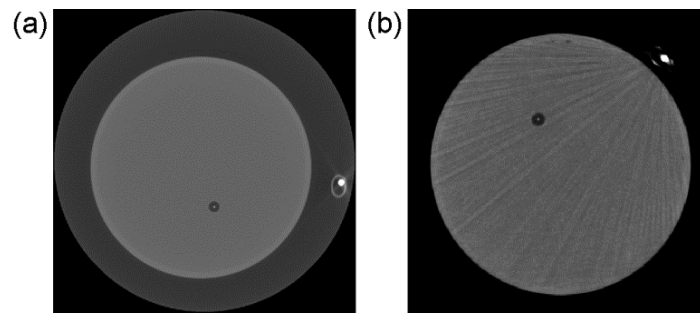


Fig. 5.2 The reconstructed axial image of the ionization chamber in the water phantom as obtained during the calibration measurement with (a) Accuitomo FOV 170×120 mm and (b) Scanora FOV 145×75 mm. The small circle with metal-like intensity present outside of the phantom is the connection cable and the waterproof sleeve of the chamber. The placement of the water phantom relative to the FOV and the position of the chamber therein is relatively free.

model. Dose calculations were realized by registering the energy deposition in predefined regions of interest (ROIs), which can be a single voxel or a voxel group. The dose result was averaged for each such ROI and reported in units of μGy . The dose statistical uncertainty was evaluated on a history-by-history basis (Walters *et al* 2002). One primary history refers to one electron bombardment on the anode target, including all descendent particles and their associated interactions. The statistical uncertainty was reported in terms of the relative standard deviation.

V.B.4. Monte Carlo calibration

With a real imaging system, the operational tube current and the effective exposure time can influence the dose magnitude for each imaging protocol. With Monte Carlo simulation, the calculated dose is proportional to the number of simulated particles. A straightforward way to obtain the *absolute* dose would be correlating the electric charge across the simulated x-ray tube with that in an actual exposure. Unfortunately, this correlation has been compromised due to the use of DBS and BCSE. One can of course simulate the radiation source without either of these techniques, but the computational efficiency would have been prohibitively poor. Therefore, the simulated source output, mediated by the phase space, is expected to have the same spectral and spatial distribution with the real one, while the number of x-rays can still be largely different. This may need to several cases in projection simulation:

- A relatively sparse phase space may have to be *recycled*, i.e. every particle contained in the phase space is transported more than once before moving onto the next. The times of transport (times of recycle plus one) for each particle must be the same in order to be unbiased.
- A very large phase space may not have to be completely used. A certain number of particles is already enough to represent the characteristics of the entire phase space. For consistency, this must be kept the same at different projection angles.
- Given the relatively low angle-dependence of dose distribution, the number of simulated projections may not necessarily be the same as it is in reality (Ding *et al* 2008, Gu *et al* 2009). However, the projections must be evenly distributed over the range of rotation in order to equalize the contribution from each angle.

In practice, such settings should be made with consideration of both the dose statistics and the computational efficiency.

Given all these complications as well as any other possible discrepancy between the simulation model and the real imaging system, dose calibration is required. Previously, we showed a simple

Table 5.2 Protocols to position the imaging FOV in oral and maxillofacial CBCT.

FOV (mm)	Protocol
Accuitomo	
170 × 120	Dentomaxillofacial/Craniomaxillofacial
100 × 100	Oral, Jaws
60 × 60	Localized, Molar
Scanora	
145 × 75	Maxillofacial
100 × 75	Oral, Jaws
60 × 60	Localized, Molar

calibration method based on the kerma free-in-air at the rotation center and examined the accuracy of the derived dose estimates (Zhang *et al* 2011). In this study, the calibration was performed specifically for dosimetry in body tissues. The approach is similar to that proposed by Ding *et al* (2008) and the ‘in-phantom’ method described by Ma *et al* (2001). It was carried out with two parallel procedures:

- A FC65-G farmer-type ionization chamber with a coupled electrometer system (IBA Dosimetry, Germany) was used to measure the dose in water at an arbitrary point within a cylindrical water phantom undergoing a typical CBCT scan. The position to place the water phantom was also arbitrary but preferably within the imaging FOV, as shown in Fig. 5.2. Both the chamber and the electrometer had been calibrated recently by an accredited dosimetry laboratory. The provided absorbed dose in water calibration factor for the diagnostic beam quality was applied to convert the electric charge reported by the electrometer to the dose which would have been received by water in the volume as occupied by the chamber. Corrections were made for the temperature in water and the air pressure at the time of measurement. Next, the dose was normalized with the electric charge across the tube. The measured absorbed dose in water, denoted by $D_{W,msr}$, was then in units of $\mu\text{Gy mAs}^{-1}$.
- The reconstructed images obtained during the measurement were used to set up the computerized water phantom and the ionization chamber for a counterpart Monte Carlo simulation. Not only can the placement of the chamber and the water phantom but also their dimensions could be retrieved from the image. Greater care should be taken if the phantom goes beyond the FOV, especially for small FOVs. A practical solution was to follow the small-FOV scan immediately with a large-FOV scan, where the first scan was for measuring the dose whereas the second scan was only for obtaining the image. Absorbed dose in water was calculated for the volume where the active end of the chamber had been present. The results were normalized against the product of transported primary histories, the simulated projection angles and the times of transport for the phase space at each angle. The Monte Carlo calculated absorbed dose in water, denoted by $D_{W,MC}$, was then in units of $\mu\text{Gy hist}^{-1} \text{ ang}^{-1} \text{ trans}^{-1}$.

The Monte Carlo calibration factor was next obtained by

$$f_{MC} = \frac{D_{W,msr}}{D_{W,MC}} \quad (\text{Eq. 5.1})$$

Table 5.3 Tissue weighting factors for use in calculation of the effective dose.

	Whole-body ICRP103	Head and neck phantoms			
		Ref. male	Ref. female	Zubal	VCH
Named tissues	0.88	0.03600	0.03497	0.04024	0.03657
Bone surface	0.01	0.00127	0.00138	0.00130	0.00106
Brain	0.01	0.01	0.01	0.01	0.01
Red bone marrow	0.12	0.01385	0.01291	0.01476	0.01464
Salivary glands	0.01	0.01	0.01	0.01	0.01
Skin	0.01	0.00088	0.00067	0.00418	0.00087
Others ^a	0.72	0.00	0.00	0.00	0.00
Remainder tissues	0.12	0.01927	0.01836	0.01101	0.01922
Extrathoracic tissue	0.00923	0.00911	0.00850	0.01	0.00923
Lymphatic nodes	0.00923	0.00054	0.00042	0.00050	0.00046
Muscle	0.00923	0.00039	0.00021	0.00051	0.00030
Oral mucosa	0.00923	0.00923	0.00923	0.00	0.00923
Others ^b	0.08308	0.00	0.00	0.00	0.00
<i>Total</i>	1.00	0.05527	0.05333	0.05126	0.05579

^a Bladder, breast, colon, gonads, liver, lung, oesophagus, stomach and thyroid.

^b Adrenals, gall bladder, heart, kidneys, pancreas, prostate (male), small intestine, spleen, thymus and uterus/cervix (female).

The value of f_{MC} was unique for each simulated phase space, i.e. for each tube potential and each FOV of the imaging system. The estimate of the dose delivered to a body tissue, in units of $\mu\text{Gy mAs}^{-1}$, was calculated by

$$\hat{D}_T = f_{MC} \cdot D_{T,MC} \quad (\text{Eq. 5.2})$$

where $D_{T,MC}$ represents the Monte Carlo calculated dose using the computational anatomical phantoms and is normalized in the same manner as $D_{W,MC}$. The simulated projection angles and the times of phase space transport in phantom simulations may not be necessarily the same to those in simulations for calibration.

V.B.5. Dose calculation schema

The protocol to position the FOV in typical cases of examination is summarized in Table 5.2. As in clinical applications, the large FOVs were simulated for the entire dentomaxillofacial region or even the craniomaxillofacial region, medium FOVs for either the maxillofacial region or the oral region and small FOVs for specific dental sites.

Organ dose was obtained by defining the ROIs on an organ-by-organ basis for the phantoms. The effective dose was derived as the weighted sum of the absorbed dose in a number of specific organs by taking into account different radiation types and the radiosensitivity of different tissues (ICRP 2007). The recommended radiation weighting factor for photons in assessing the effective dose is unity so it was implicitly always included. The recommended tissue weighting factors are organ-specific, which could lead to several complications in practice:

- For organs that are not available in the phantoms, appropriate surrogates may have to be used.

- Some organs, such as the muscles and the skin, are distributed over the entire body, so the tissue weighting factors have to be fractioned for applications involving only the head and neck.
- Special measures have to be taken for skeletal dosimetry since it is associated with high tissue weighting factors and the skeletal structures may not be directly available in the phantoms.

Table 5.3 shows the assignment of tissue weighting factors in this study. The value for organs that do not belong to the head and neck anatomy was set to be zero, while the value for partially presented organs was fractioned by the corresponding organ mass in the entire body. Because the whole-body information is not available for the Zubal phantom, this was performed with respect to the reference mass ratios (ICRP 2002). The tongue was used as a surrogate for the salivary glands in the Zubal phantom. The lymphatic nodes, which were not available in the Zubal and the VCH phantom, were substituted by the fat tissue and the whole-body mass ratio was estimated to be 0.05. The weighting factor for the oral mucosa was split and evenly transferred to all the organs in the ‘remainder’ for the Zubal phantom. It was worth mentioning that the thyroid is not present in the head and neck part for any of the four phantoms, so not included in the calculation of effective dose. For pediatric patients, this cannot be ignored because a large part of the neck will be covered within the imaging FOV (Theodorakou *et al* 2012). However, for adults, the thyroid dose is only due to long-distance scattered radiation and should not make any substantial difference to the effective dose after the application of tissue weighting factors.

The dose received by the entire bone was used as a conservative estimate for the bone surface. Although the bone marrow was segmented explicitly with the original datasets of the Zubal and the VCH phantom, it is still difficult to be sufficiently accurately represented under the voxel resolution that is currently available with the phantoms. The dose to red bone marrow (RBM), therefore, was obtained via the so-called ‘3-Factor’ approach (Zankl *et al* 2002, Kramer *et al* 2003):

$$\hat{\varepsilon}_{RBM} = \varepsilon_{Mix} \cdot r_{RBM} \cdot \frac{\left(\frac{\mu_{en}}{\rho}(E_p) \right)_{RBM}}{\left(\frac{\mu_{en}}{\rho}(E_p) \right)_{Mix}} \cdot S(E_p) \quad (\text{Eq. 5.3})$$

where $\hat{\varepsilon}_{RBM}$ is the estimate of the energy deposited in the RBM, ε_{Mix} the energy deposited within the skeletal mixture containing the RBM, r_{RBM} the mass ratio of the RBM to the mixture, $\frac{\mu_{en}}{\rho}$ the mass energy absorption coefficient for the RBM and the mixture, and S the correction factor of photoelectron dose enhancement for the bone site under consideration. The values of $\frac{\mu_{en}}{\rho}$ and S are

specific to the photon energy E_p that leads up to the energy deposition. The $\frac{\mu_{en}}{\rho}$ data were taken from

Hubbell and Seltzer (2004) and the S data were based on King and Spiers (1985). Linearly interpolation was applied for evaluation at continuous photon energies. The skeletal mixture for the reference phantoms was considered to be the spongiosa, which were in our simulation averaged over the head and neck and assumed to have a uniform distribution of RBM. For the Zubal and the VCH phantom, the entire bone was taken as the skeletal mixture, including both the trabecular and the cortical tissue. The proportion of red bone marrow was assumed to be consistent with the reference values (ICRP 2002). Averaging the skeletal mixture allowed the 3-Factor approach to be implemented on an organ-by-organ basis instead of a voxel-by-voxel basis, thus the Monte Carlo dose calculation for the RBM stayed in line with that for other organs.

Table 5.4 The Monte Carlo dose calibration factors for selected exposure settings.

Tube potential (kV)	FOV (mm)	Calibration factor (hist ang trans mAs ⁻¹)
Accuitomo		
60	170 × 120	9.606e+13
70	170 × 120	1.552e+14
80	170 × 120	2.283e+14
90	170 × 120	3.055e+14
90	100 × 100	2.146e+14
90	60 × 60	8.494e+13
Scanora		
90	145 × 75	1.975e+14
90	100 × 75	1.514e+14
90	60 × 60	8.917e+13

For an easier implementation of the 3-Factor approach, Kerma Approximation was made throughout the projection simulations, i.e. the secondary electrons were discarded once they were given birth and all of their carried energy was assumed to be deposited locally. Given the limited electron range in biological tissues for the diagnostic energy regime, this should have negligible influence on dose distribution, especially to internal organs (ICRP 2007). Kerma Approximation speeded up the simulation and more importantly allowed us to ignore the secondary electrons, which could also enter the skeletal mixture from surrounding tissues and contribute to the dose in the RBM. Energy deposition, therefore, may occur in the skeletal mixture by only three scenarios, where great care must be taken in determining the values of ε_{Mix} and the associated E_p :

- Photoelectric absorption. The triggering photon energy should be taken for both E_p and ε_{Mix} , since the generated photoelectron is to be stopped immediately from radiation transport under Kerma Approximation.
- Compton scatter. E_p is the energy of the photon right before the interaction and ε_{Mix} should be E_p minus the energy of the secondary photon.
- Low-energy cutoff. The photon gets killed as its energy falls below the predefined threshold in simulation. E_p and ε_{Mix} are both assigned with the energy of this photon. The threshold was set to be 10 keV throughout our simulations.

Dose profiles were calculated by defining the ROIs on a voxel-by-voxel basis. This is similar to the prediction of 3D dose distribution for treatment planning in image-guided radiotherapy, except that general-purpose phantoms have been used in this study instead of patient-specific phantoms. The latter are usually based on the inherent correlation between the pixel values in acquired CT images (the CT numbers) and the tissue parameters, which can be heterogeneous within each organ or structure. However, the phantoms employed in this study were defined organ by organ, thus have a homogeneous tissue properties within each organ. We have focused on the planar dose distribution, but the method is obviously easily applicable to 3D.

Since the calibration managed to correlate the Monte Carlo calculation to the electric charge across the x-ray tube, dose results were all applied with the corresponding calibration factor to be expressed in terms of the *dose rate*, i.e. in units of $\mu\text{Gy mAs}^{-1}$. The applicability of the calibration factor to dose profiles is obvious because the calibration was also based on point dose.

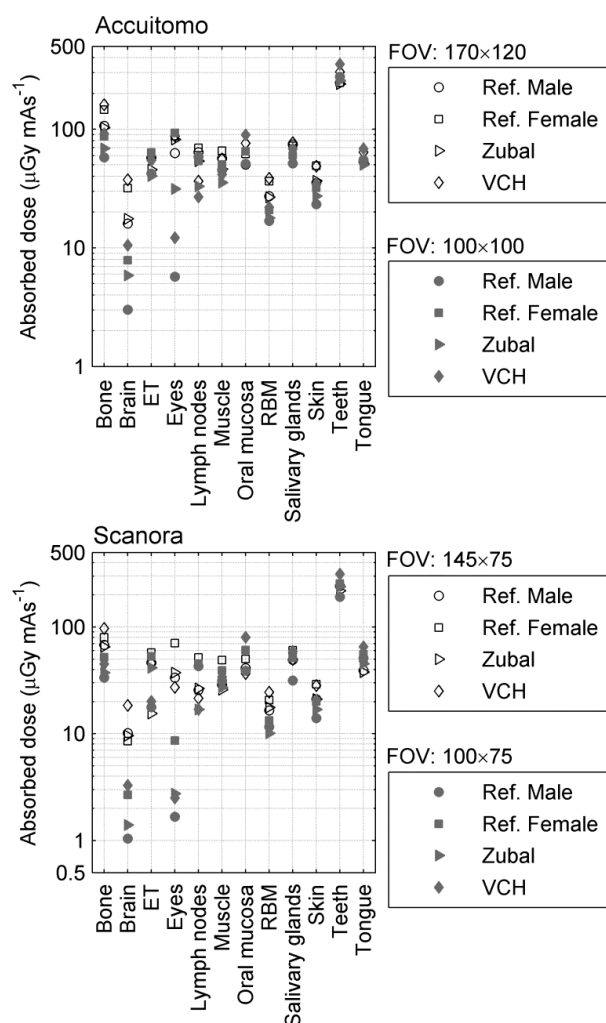


Fig. 5.3 Organ absorbed doses calculated for different phantoms with the large and the medium FOV of the Accuitomo (upper) and the Scanora (lower) at 90 kV. 'ET' and 'RBM' stand for the extrathoracic tissue and the red bone marrow, respectively.

V.C. Results

V.C.1. Calibration factors and dose statistical uncertainty

The dose calibration factors of the Monte Carlo simulation model for selected exposure settings are listed in Table 5.4. The dose statistical uncertainty should include both the calibration uncertainty and the uncertainty reported by the dose calculation. The former one can be evaluated with repetitive measurements in calibration. Considering the uncertainty of the chamber (2% for the chamber calibration factor) as well as the environmental factors, it was estimated to be <5%. The latter one is actually controlled by the length of simulation. By simulating $>2 \times 10^6$ primary histories per projection and a constant angular interval of 1.0 degree, the dose uncertainty was able to be reduced <0.5% for the organs in most cases. Therefore, the overall statistical uncertainty for the organ doses and the effective doses should be ~5%. The dose profiles were calculated with $\sim 1 \times 10^7$ primary histories per

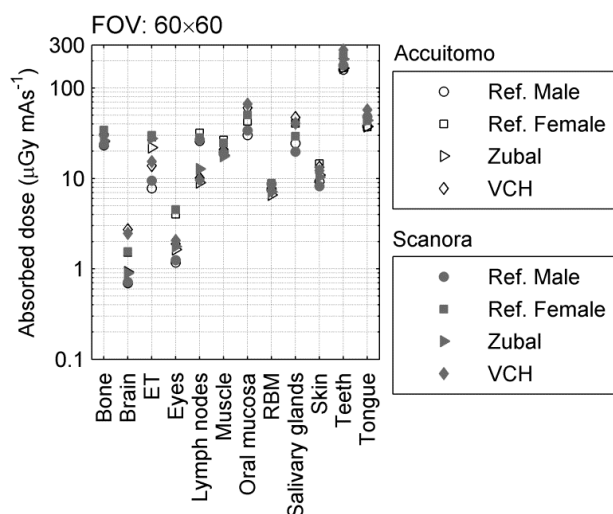


Fig. 5.4 Organ absorbed doses calculated for different phantoms with FOV 60 × 60 mm of the two CBCT systems at 90 kV.

Table 5.5 Effective doses (μGy mAs⁻¹) calculated for the phantoms with selected FOVs of the two systems at 90 kV.

FOV (mm)	Ref. male	Ref. female	Zubal	VCH
Accuitomo				
170 × 120	2.496	2.898	1.870	3.182
100 × 100	1.780	2.267	1.463	2.584
60 × 60	0.767	1.237	0.792	1.346
Scanora				
145 × 75	1.757	2.072	1.089	1.944
100 × 75	1.099	1.842	1.171	1.797
60 × 60	0.785	1.219	0.921	1.346

projection. The dramatically high uncertainty (>100%) resulted at some individual positions could be seen as noise when observing the overall dose distribution pattern.

V.C.2. Organ and effective doses

Calculated organ absorbed doses for the phantoms with a large and a medium FOV and a tube potential of 90 kV are graphed in Fig. 5.3. For the Accuitomo, relative standard deviation of the organ dose for different phantoms is 3-41% with FOV 170 × 120 mm and 12-112% with FOV 100 × 100 mm. For the Scanora, it is 6-46% with FOV 145 × 75 mm and 12-82% with FOV 100 × 75 mm. The largest deviation is showed for the eyes, which is close to the edge of the simulated FOV. The substituting organs for use in calculating the effective dose show no dramatic difference than the named organs, thus would not affect the effective dose. The doses to the oral mucosa, the teeth and the tongue are mostly higher with the medium FOV, since it is more focused on the oral region than with the large FOV. In general, organ doses delivered by the Scanora system are of a slightly larger variation compared to those by the Accuitomo, probably due to the offset scanning geometry.

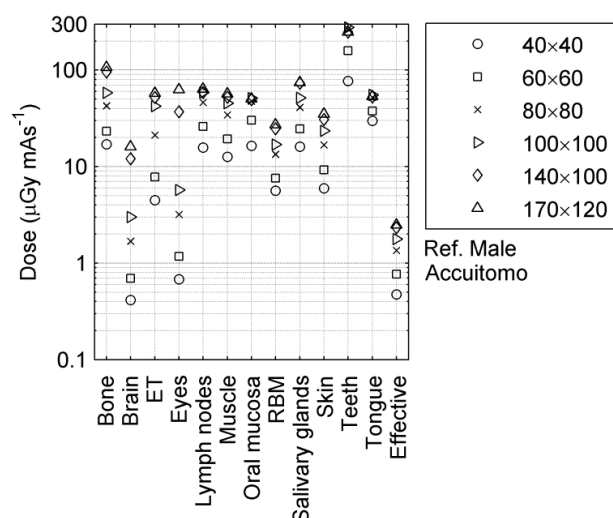


Fig. 5.5 Comparison of the organ absorbed dose and the effective dose for the reference male phantom calculated with different FOVs of the Accuitomo at 90 kV.

The only identical FOV between the Accuitomo and the Scanora system is the FOV 60×60 mm. Comparison of the organ absorbed dose in such scenario is provided in Fig. 5.4. Of note is that the position of the FOV with respect to the phantom was exactly the same for the two systems. The organ dose deviation is 10-55% between the systems and among different phantoms. For the muscle and the skin, the Accuitomo always delivers a higher dose than the Scanora, while for the extrathoracic tissue, eyes, oral mucosa, RBM, teeth and tongue, it is always higher with the Scanora. The largest variation was found for the brain and the eyes, since they are completely outside of the FOV.

Calculated effective doses for the phantoms under a tube potential of 90 kV and selected FOVs are provided in Table 5.5. The missing neck of the reference female phantom does not result in substantially low effective doses. The effective doses associated with the Scanora are about 20-40% lower than the Accuitomo in the large and the medium FOV, which is in part owing to the offset scanning of the Scanora system. The phantoms receive comparable effective doses with FOV 60×60 mm for two systems. Generally, the effective doses are higher with a larger FOV, except that a lower effective dose is delivered to the Zubal phantom with Scanora FOV 100×75 mm than with FOV 145×75 mm. This might be due to the position of the medium FOV, which is more focused on organs with a high tissue weighting factor, such as the salivary glands. Dose variation among different phantoms with the same FOV of the same CBCT system is up to 30%, in terms of the relative standard deviation. The causation includes the difference on both the phantom anatomy and the position of the FOV. It also implies great dose variation among individual patients.

Figure 5.5 shows a further dose comparison for the reference male phantom under six different FOVs of the Accuitomo ranging from 40×40 mm to 170×120 mm. Absorbed doses for some organs that were not used in calculating the effective dose are also presented. The positions of FOVs 40×40 , 80×80 and 140×100 mm were identical to those of FOVs 60×60 , 100×100 and 170×120 , respectively. The effective dose and most organ doses increase with the size of the FOV. The highest organ absorbed dose is for the teeth with the FOVs 80×80 and 100×100 mm that focus on and cover the entire dentition. The relative standard deviation of the effective dose is $>50\%$. The largest deviation on the organ absorbed dose is found for the brain and the eyes, which are both $>100\%$. Organs with a relatively more uniform distribution, such as the bone, lymphatic nodes and muscles, are associated with smaller dose deviation in general.

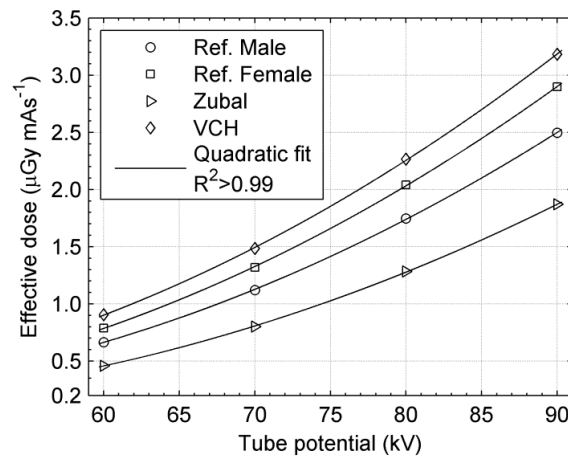


Fig. 5.6 Calculated effective doses with Accuitomo FOV 170×120 mm at different tube potentials.

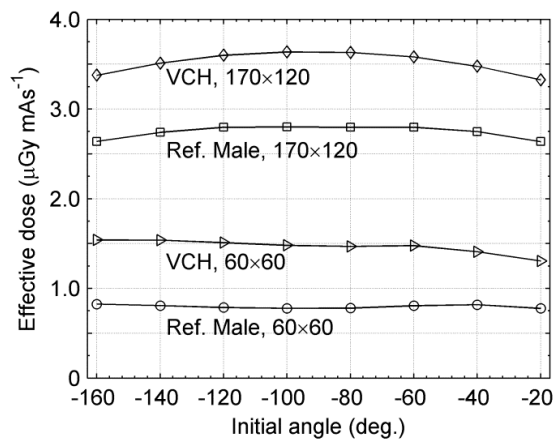


Fig. 5.7 The effective doses calculated for the reference male and the VCH phantom with the half-rotation mode of the Accuitomo at 90 kV from different initial angles.

The Accuitomo system has offered an opportunity to investigate the dose dependency on the operating tube potential. The effective doses calculated for the phantoms with FOV 170×120 mm at 60, 70, 80 and 90 kV are shown in Fig. 5.6. The increase of the effective dose with the tube potential can be roughly described with a quadratic polynomial model. The effective doses at 90 kV are >3 times higher than those at 60 kV. The dose difference among different phantoms is comparable at different tube potentials, which is $\sim 25\%$ in terms of the relative standard deviation.

Compared to the offset design of the Scanora, the Accuitomo also provides a setup for application in low-dose scenarios, which is the *half-rotation* scan. In such mode, the exposure is only performed in 180° , which leads to a concern that the start point of the exposure may influence the dose distribution in patients. We use the initial angle of the source with respect to the central coronal axis of the phantom to represent the start point of the exposure. For instance, an initial angle of -90° forms a symmetrical exposure over the anterior side of the phantom and from one lateral direction to the other. The variation of the effective dose for the reference male and the VCH phantom with two FOVs at 90 kV is shown in Fig 5.7. The relative standard deviation for the reference male phantom is $\sim 2\%$ with FOV 60×60 mm and $\sim 3\%$ with FOV 170×120 , while it is $\sim 5\%$ and $\sim 3\%$ for the VCH phantom. Such small variation suggests that the initial angle as relative to the patient could be

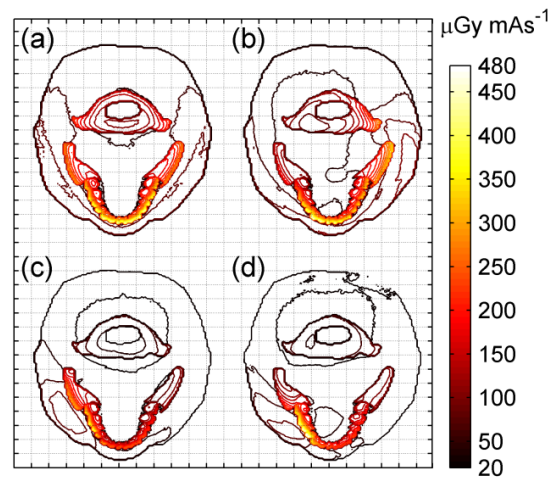


Fig. 5.8 Dose profiles calculated for a typical axial plane of the Zubal phantom with (a) Accuitomo FOV 170×120 mm, (b) Scanora FOV 145×75 mm, (c) Accuitomo FOV 60×60 mm and (d) Scanora FOV 60×60 mm at 90 kV.

determined without too much consideration on the dose whereas more in regard of the resulting image quality.

V.C.3. Dose profiles

Dose profiles were calculated with the largest FOV and FOV 60×60 mm at 90 kV of the two systems using the Zubal phantom, which has the highest resolution over the axial plane. Figure 5.8 shows the dose distribution in form of contour profiles for a typical axial plane across the mandible. It can be observed that the bony tissue receives higher dose than the surrounding soft tissue. Good symmetry with respect to the coronal axis is exhibited for Accuitomo FOV 170×120 mm, while the dose is inclined to one side for Scanora FOV 145×75 mm. Since the FOV in such cases was positioned around the middle of the left and right halves, this asymmetric dose distribution for the Scanora is surely due to its offset scanning geometry, where the half-projection field is relatively close to the left half (patient perspective) of the maxillofacial region from anterior incident angles. As the source approaches posterior positions, it faces but becomes relatively distant to the right half of the maxillofacial region and more attenuated by the back side of the head. With FOV 60×60 mm, the focus was put on the localized molar region, where the highest dose was found as expected. The dose distribution is comparable over the jaw bone for the two systems. Of note is that the dose delivered to the far end of the traversal region by the Scanora appears to be vanishingly low.

V.C.4. Comparison with experimentally measured dose data

The comparison of the Monte Carlo dose estimates with the experimentally measured data was difficult because:

- The difference between the physical and computational phantoms was difficult to evaluate.
- The exact positioning of the FOV in physical measurement remains obscure in literature, unlike in our simulations where the positioning was precisely made under the guidance in 3D visualization.
- The CBCT systems may have been undergoing continuous update over time, which is an added complication in comparing the experimental and simulated results.

Therefore, case-by-case comparison was not feasible and we had to focus only on the dose range.

The data of organ and effective dose reported by Pauwels *et al* (2012) cover a wide range of oral CBCT systems and imaging protocols. They were measured by use of two physical anthropomorphic phantoms loaded with TLDs and are provided in terms of the absolute dose corresponding to each specific exposure setting. We have normalized the data with the corresponding tube current and exposure time such that they are in the same units as in this study. Given the materials and methods in obtaining the dose, the experimental study is more focused on the variation among different CBCT systems while our simulation study is better in dose accuracy and reproducibility and in accounting for the difference of phantoms. The measured effective dose range with large FOVs and maxillofacial imaging protocols is 1.3-22.0 $\mu\text{Gy mAs}^{-1}$, that with medium FOVs and dentoalveolar or single jaw protocols is 0.6-6.2 $\mu\text{Gy mAs}^{-1}$ and that with small FOVs and localized dental imaging protocols is 0.2-0.5 $\mu\text{Gy mAs}^{-1}$. A total of fourteen different CBCT systems were involved and each measurement was based on a few selected systems and exposure settings. The data provided in Table 5.5 are considered to be comparable in imaging protocols to those categorized in the experimental measurement, where the Monte Carlo calculated effective dose ranges are 1.1-3.2, 1.1-2.6 and 0.8-1.3 $\mu\text{Gy mAs}^{-1}$, respectively. The calculated range shows a slightly lower bound than the measured one for large FOV protocols but is within the measured range for medium FOV protocols. The calculated dose range goes above the measured range for the localized protocol, which might be explained by the very different size and positioning of the small FOVs. Overall, the measured ranges appear to be much wider than those simulated with different computational phantoms, suggesting that the system difference of CBCT is a more important factor for dose variation than anatomical difference of the patients.

V.D. Discussion

The established simulation model offers an accurate and flexible means to acquire the dose information associated with oral and maxillofacial CBCT. The dose calculations are not limited to typical cases of CBCT examination but can be extended to systematic or any custom assessment for different systems and imaging protocols. One potential way to improve the Monte Carlo modeling approach is about the phantom. In addition to the anatomical phantoms as demonstrated in this study, the medical internal radiation dose (MIRD)-based stylized phantoms (Bouchet *et al* 1999) and more anatomical phantoms representing various human groups (Zaidi and Tsui 2009) can be used in the same manner. Phantom resolution and the anatomical realism are important factors to be considered. Phantoms based on the boundary representation method, for instance, are free of the problems that occurred from the rigid separation of the head and neck from the trunk (Na *et al* 2010). The ability of spatial deformation may help in adjusting the gesture. It also provides convenience to manipulate the existing phantom by adding pathological features, such as to describe an implant case by modifying a dental site with an artificial substitute. Techniques that may help in characterizing the oral and maxillofacial anatomy, a complex mixture with bony tissue, soft tissue and air cavities, could also be potentially very useful.

The Monte Carlo simulations in this study were grouped by phantom or by FOV and were carried out on a computing cluster. Considerations on computational efficiency of the simulation have been carefully addressed in Zhang *et al* (2011). Calculating the dose distribution is of lower expenses than simulating images. Once the source data are ready, good dose statistics can be achieved over short Monte Carlo simulations as needed in obtaining the coarse scatter projection images. Including dose calculation to the estimation of scatter distribution adds no substantial time during the projection simulation. Kerma Approximation has been made as required by the 3-Factor approach for skeletal dosimetry. At the meanwhile, it speeds up the simulation by cutting off the transport of secondary electrons. The side effect on dose distribution is supposed to be greater in high-energy scenarios and more obvious to the superficial organ, which is the skin. The difference in the skin dose, with and without Kerma Approximation, was found to be <0.4% with the large FOVs of the two CBCT system

at 90 kV. The influence to the effective dose should be negligible. The 3-Factor approach itself could be validated if only the phantom resolution was sufficiently high for detailed representation of the trabecular tissue. A fashionable alternative is to substitute each voxel of the trabecular bone with a so-called ‘micro-matrix’, where the bone marrow distribution is described with a higher voxel resolution than that of the rest body parts (Walters *et al* 2009). However, ample evidence has been reported in literature for the accuracy of the 3-Factor approach (Zankl *et al* 2002, Kramer *et al* 2003), so we have only focused on its implementation in the simulation model.

V.E. Conclusion

The approach of Monte Carlo modeling for radiation dosimetry has been explored in this study with application to two dedicated oral and maxillofacial CBCT systems. The simulation model and the experimental calibration procedure are flexible and can be directly applied to dosimetric studies of CBCT in general. The calculated organ and effective doses for four computational anatomical phantoms show large variation among different imaging protocols. Systematic dose investigation would be easily achievable in the same manner. The ability to obtain the dose profile as a part of 3D dose estimation is also shown. Comparing to the experimental measurements using physical phantoms, the Monte Carlo modeling approach has great advantage in efficiency as well as in statistical accuracy.

Chapter

VI. Application: Image Quality

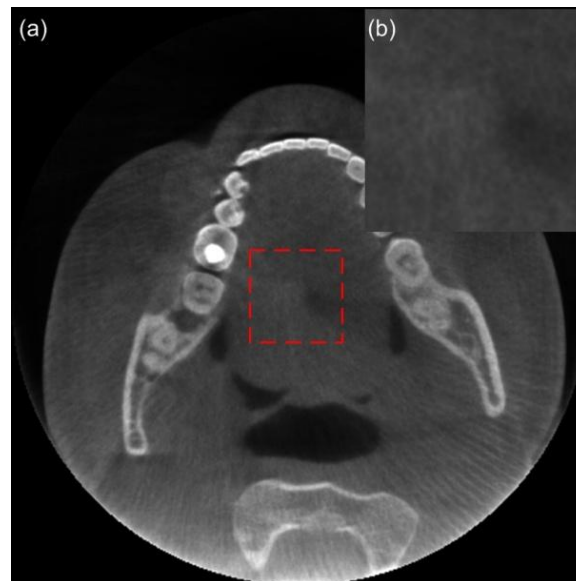


Fig. 6.1 (a) Example of the central artefact with offset CBCT, as indicated by the dashed red square; (b) the enlarged view of the artefact region.

VI.A. Assessment of central artefact in cone beam CT with offset scanning geometry

VI.A.1. Introduction

Scatter has been recognized as one of the major sources for image artefacts in x-ray CT (Joseph and Spital 1982, Kanamori *et al* 1985). Photons undergoing Compton and/or Rayleigh scatter within the matter may deviate from their initial paths, contaminate the intensity measurements for use in image reconstruction, and lead to various image artefacts and poor contrast detectability. This effect is even worse in cone beam CT (CBCT), where a relatively large size flat panel detector (FPD) is used (Endo *et al* 2001, Siewerdsen and Jaffrany 2001). Naturally, reducing the signals from scattered radiation, by means of a pre-processing design such as antiscatter grids, should be able to improve the image quality (Siewerdsen *et al* 2004, Kyriakou and Kalender 2005). Accurate estimation of the scatter distribution, on the other hand, is also helpful when combined with different post-processing scatter correction algorithms (Jarry *et al* 2006, Zbijewski and Beekman 2006). However, it is still interesting and equally important to know whether a certain kind of image artefact is related to scatter and if it is so, how they are related, before any scatter reduction or correction attempt.

One type of artefact that remains ambiguous till now is the artefact that appears specifically around the central axis of the reconstructed imaging field of view (FOV). As shown in Fig. 6.1, this artefact is usually presented as a circular region with abnormal intensity variation. It has only been found in CBCT which is associated with a so-called *offset* image acquisition geometry. Offset CBCT geometry is widely implemented nowadays as a solution to the growing demand of large FOV versus the cost-prohibitive FPDs (Wang 2002). It allows the CBCT system to reconstruct an image of the same cylindrical volume with a detector of roughly half the size compared to that in a symmetrical mode. Practically, the detector is positioned offset to the center of rotation, providing a setup where a large part of the FOV to the periphery is scanned in only 180° (plus the fan angle) while a small central region is covered by all angular projections (half-projections). This results in a rupture of x-ray transmission data relating opposite angles and raises difficulties for image reconstruction. To tackle this issue, classical reconstruction algorithms have to be modified (Valton *et al* 2006, Hansis *et*

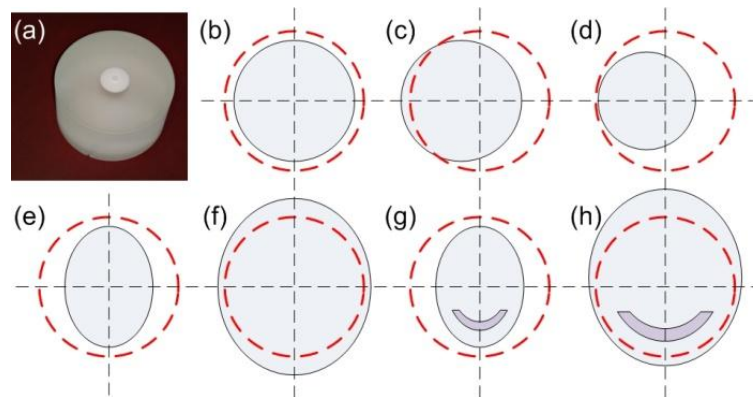


Fig. 6.2 (a) QA phantom supplied with the Scanora 3D system; (b)-(h) Axial views of phantom and placement in the cases designed for the simulation experiment, where the dashed red circle represents the diameter of the FOV.

Table 6.1. Specification of the cases designed for the simulation experiment.

Case No.	Cylinder cross-section		Materials	Position	FOV truncation
	Shape	Dimension (mm)			
1	Circular	14.0 × 14.0	PMMA	Rotation center	No
2	Circular	14.0 × 14.0	PMMA	10 mm left to rotation center	Yes
3	Circular	12.0 × 12.0	PMMA	10 mm left to rotation center	No
4	Elliptical	14.0 × 11.2	PMMA	Rotation center	No
5	Elliptical	20.0 × 16.0	PMMA	Rotation center	Yes
6	Elliptical	14.0 × 11.2	PMMA + Al	Rotation center	No
7	Elliptical	20.0 × 16.0	PMMA + Al	25 mm anterior to rotation center	Yes

al 2010). The central artefact is likely to be the remaining intensity imbalance when greater shading artefacts between the left/right halves have been wiped off. One may therefore suspect that the asymmetric scatter distribution is disturbing the theoretical assumptions behind the reconstruction technique and causes such problem.

The purpose of this study is to assess the central image artefact associated with an offset CBCT geometry. The relationship between the artefact and the scattered radiation as well as other potential factors was investigated by use of a hybrid simulation model and various computational phantoms. Different image reconstruction techniques were considered. This work looked into the problem from a dedicated CBCT system in daily clinical use of head and neck imaging. The methods and findings should be valid to offset CBCT systems in general.

VI.A.2. Materials and methods

It was hypothesized that the central artefact in offset CBCT imaging is caused by and only by the rotationally asymmetric distribution of scatter. To evaluate this, three predictions were examined:

- (1) Symmetric objects produce no such artefact when placed symmetrical within the axial plane, i.e. strictly at the rotation center;
- (2) The central artefact is produced by symmetric objects in asymmetrical positions, e.g. shifted away from the rotation center, or asymmetric objects at any position;
- (3) Scatter-free projection data of (2) are free of the central artefact after image reconstruction.

The offset CBCT setup considered in the present study is based on the Scanora 3D CBCT system (Soredex-PaloDEX, Finland). It is a dedicated system for application in head and neck imaging, particularly for oral and maxillofacial regions as well as for regions relative to the ear, nose,

Table 6.2 The central artefact is present (+) or not (–) within the reconstructed image for different cases of the simulation experiment.

	Recon.	Cases						
		1	2	3	4	5	6	7
With scatter	ART	–	+	+	+	+	+	+
Without scatter	ART	–	–	–	–	–	–	–
With scatter	FBP	–	–	–	–	–	–	–
Without scatter	FBP	–	–	–	–	–	–	–

and throat. The operating tube potential is fixed at 90 kV while the current can be adjusted in a range from 4.0 to 12.5 mA. The total beam filtration, in terms of aluminum-equivalent thickness, is ~ 7.7 mm. The focal spot to rotation axis and to detector distances are ~ 419 mm and ~ 650 mm, respectively. The FPD has an active imaging area of 608×616 pixels (horizontal \times vertical), with a pixel size of $200 \times 200 \mu\text{m}^2$. The center of FPD is offset by ~ 55 mm with respect to the perpendicular beam direction, leaving a width of ~ 5 mm as the overlap between opposite half-projections. The largest FOV, with a cylindrical volume of $145 \text{ mm} \times 75 \text{ mm}$ (diameter \times height), and the standard reconstruction resolution, with an isotropic voxel dimension of $350 \mu\text{m}$, were considered in this study. Each rotational scan consists of 225 evenly populated half-projections over 360° .

The simulation technique follows a validated hybrid approach (Zhang *et al* 2011). Briefly, the Monte Carlo technique was responsible for simulating the x-ray generation, filtration and collimation. The source output was dumped to a so-called phase space and was transformed along the source trajectory to produce the rotational cone beam radiation field. The object to be imaged was represented in a voxelized fashion. The primary projections were analytically obtained by ray-tracing (Siddon 1985). The scatter projections were based on short Monte Carlo simulations followed by an iterative fitting process (Colijn and Beekman 2004). The magnitude of the primary and the scatter data was correlated by the phase space. By merging the primary and scatter components or using the primary data only, influence of the scattered radiation was able to be investigated. Projection images were next filtered with the measured detector resolution and noise characteristics, in terms of the modulation transfer function (MTF) and the noise power spectrum (NPS), respectively. Both the MTF and the NPS were measured with standardized methods (IEC 2003). The filtering processes were conducted in the frequency domain. While the NPS was used in characterizing the correlation of the image noise, the noise magnitude was determined according to the signal mean-variance relationship measured from the imaging system. Then, the sequence of projection data underwent a similar pre-processing pipeline as on the real system and was ready for image reconstruction. The reconstruction was performed with the commercial software integrated with the Scanora 3D system, where an algebraic iterative reconstruction technique (ART) was used by default. To assess the specificity of the central artefact to different reconstruction methods, the filtered back-projection (FBP) reconstruction was additionally carried out for comparison.

In evaluating the hypothesis, simple geometric phantoms were utilized. These phantoms were variants of the physical cylinder phantom supplied with each Scanora 3D unit, which is used in routine quality assurance (QA) practices. Figure 6.2 shows the QA phantom and the cases designed for the simulation experiment. We focused on the axial plane and the detailed case information is summarized in Table 6.1. Based on the original dimension of the QA phantom, which is 140 mm in diameter and 85 mm in height, the cross-section of the computational phantoms was made either circular or elliptical, while the height was always set to be sufficiently larger than the longitudinal FOV. Then, a perfect symmetrical scenario can be created by placing a circular cylinder phantom strictly at the rotation center (case 1), in which the simulation needed to be conducted only once and the data were replicated for different projection angles. Asymmetry was formed by shifting the circular cylinder phantom away from the rotation center (cases 2 and 3) and by use of an elliptical

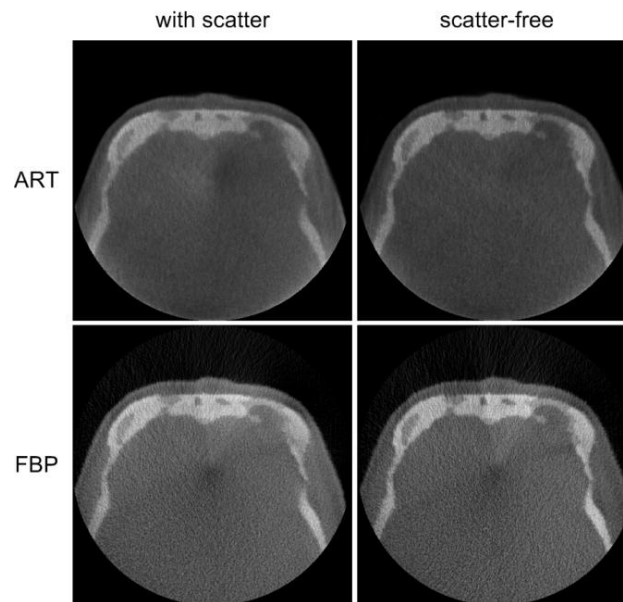


Fig. 6.3 Reconstructed image with the Zubal phantom.

cylinder phantom (cases 4-7). Cross-section dimensions of the cylinders were varied with respect to the diameter of the FOV in order to assess the influence of truncation (cases 3 vs. 2 and cases 5 vs. 4). The cross-section of the elliptical cylinder phantom, when scaled up from $14.0 \text{ mm} \times 11.2 \text{ mm}$ to $200 \text{ mm} \times 160 \text{ mm}$ (major \times minor axis), is comparable to the shape of an adult human head (cases 4 to 5 and cases 6 to 7). An arc aluminum insert was modeled to approximate the lower jaw bone, which also increased the degree of asymmetry (cases 6 and 7). In order to speed up the simulation, a coarse isotropic voxel dimension of 2 mm was adopted in cases 2-7.

As a further examination, we made use of the Zubal phantom, a voxel-based computational phantom for the human head and brain (Zubal *et al* 1994). The phantom was developed using the segmentation data of transaxial magnetic resonance (MR) images. The voxel resolution was $1.1 \times 1.1 \text{ mm}^2$ within the axial plane and 1.4 mm across the vertical direction. The implementation of this phantom with the simulation model represented a more heterogeneous and better realistic scenario compared to case 7. Given the size of the phantom, FOV truncation always existed in the axial plane. The phantom is only available for the upper half of the head, so the simulation was focused on the cranial region as well as the frontal sinus region, although the Scanora 3D system is not dedicated in visualization of neurological structures.

VI.A.3. Results and discussion

Table 6.2 summarizes whether or not the central artefact is present within the central axial slice of the reconstructed volume for the geometric phantoms. Case 1 represents the perfect symmetry scenario. No central artefact is observed with ART or FBP. Cupping artefact is still found for the FBP, which is a combined result of the scattered radiation as well as the beam hardening effect. Cases 2 and 3 show results for the circular cylinder phantom in a shifted position. Images reconstructed with ART show the artefact when scatter data is included and the artefact disappears when the scatter is removed. No such artefact is exhibited by FBP, neither with nor without scatter. No particular difference is found between cases 2 and 3, suggesting the central artefact is independent of FOV truncation. Results of the elliptical cylinder phantom additionally prove the asymmetry by an elliptical shape can already lead to the central artefact, even though the phantom has still mirror

symmetry with respect to the x - y axes. Next, it indicates the increased extent of FOV truncation does not add much to that of the central artefact, comparing cases 4 and 5. On the contrary, higher asymmetry of the object itself, by a mandible-shaped aluminum insert and eccentric FOV (case 7), brings in a stronger central artefact.

The reconstructed images of the Zubal phantom with and without scatter are shown in Fig. 6.3. The results are consistent with that of the evaluation using geometric phantoms. It also demonstrates the ability and flexibility of the simulation technique for use in highly realistic image simulation with computational anatomical phantoms.

VI.A.4. Conclusion

The hypothesis has been proved. It confirms that asymmetric distribution of the scatter tends to cause artefacts around the center of the reconstructed image in CBCT with an offset geometry. This effect is particularly evident in case of the algebraic iterative reconstruction. Truncation of the imaging FOV for large objects is not quite related to the central artefact. Increased asymmetry, by either the object's structure or eccentric placement, may lead to stronger appearance of the central artefact. The central artefact under offset CBCT imaging is, therefore, to be classified into the category of scatter-induced artefacts. Computer simulation, as adopted in this study, can be a generally efficient approach to investigate the performance of CBCT, and more in particular for its reconstruction algorithms.

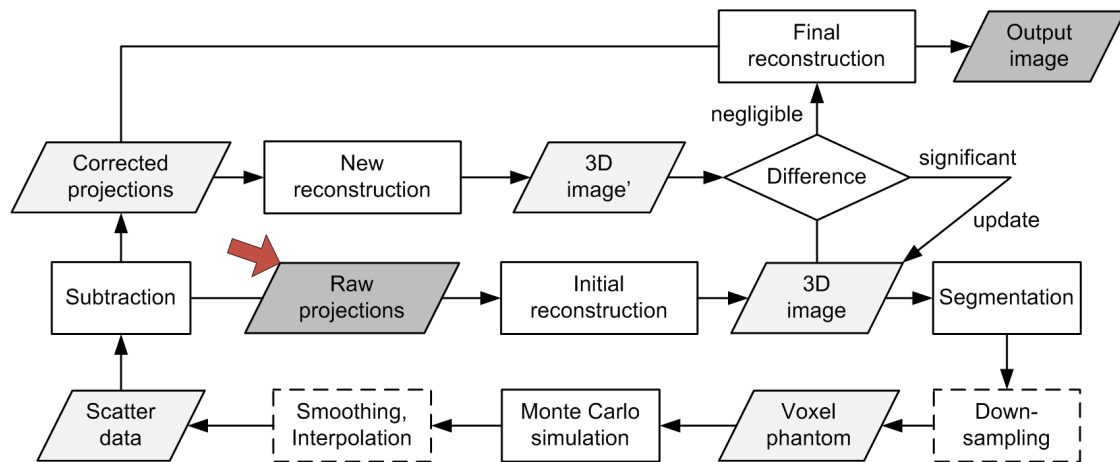


Fig. 6.4 Flowchart of a typical Monte Carlo scatter correction algorithm for CBCT. Dashed boxes represent optional steps.

VI.B. Model-based volume restoration for Monte Carlo scatter correction in cone beam CT with limited field of view

VI.B.1. Introduction

X-ray photons undergoing Compton and/or Rayleigh scatter in computed tomography (CT) scan may deviate from their initial direction, contaminate the measurement of x-ray transmission at the receptor, disturb the image reconstruction process, and lead to various artefacts and poor contrast detectability (Joseph and Spital 1982, Kanamori *et al* 1985). This effect is more severe in cone beam computed tomography (CBCT), where a truly two-dimensional (2D) receptor—flat panel detector (FPD)—is used and the relative amount of scatter signal becomes higher due to the increased imaging area (Siewerdsen and Jaffray 2001). To tackle this issue, both hardware and software techniques have been introduced (Ruhrschopf and Klingenbeck 2011a). Collimation of the radiation field and the application of anti-scatter grids, for instance, are efficient approaches to reduce the scatter prior to image processing. Post-processing scatter correction algorithms are also used, which require accurate estimation of the scatter distribution (Ruhrschopf and Klingenbeck 2011b). Among different strategies to do so, the Monte Carlo scatter correction has been a hot topic in recent CBCT investigations (Jarry *et al* 2006, Zbijewski and Beekman 2006).

Figure 6.4 shows the flowchart of a typical Monte Carlo scatter correction algorithm for CBCT. It starts from the raw data, i.e. the image sequence acquired over different angular projections, including both primary and scatter signals. Direct reconstruction—the *initial reconstruction*—results in a three-dimensional (3D) image that may contain scatter artefacts. By converting this image into a 3D voxel phantom and importing it to a Monte Carlo simulator, scatter information can be retrieved for each projection. Then, correction can be made by subtracting the Monte Carlo simulated scatter data from the raw data on a projection-by-projection basis. Reconstruction of the corrected data—the *new reconstruction*—is expected to result in a 3D image with largely suppressed scatter artefacts. Since the voxel phantom had been created from the original 3D image that may have suffered from scatter artefacts, its fidelity to the image object may have been compromised, affecting the accuracy of the scatter estimates. Another cycle of Monte Carlo simulation with updated phantom data according to the output of the new reconstruction may improve the results. In this way, the scatter accuracy as well as the resulting image quality can be continuously improved with an iteratively

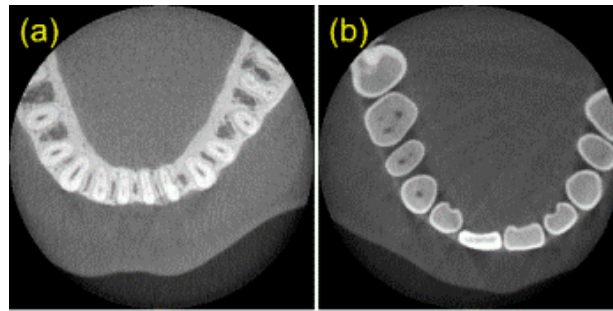


Fig. 6.5 Two patient images from 6×6 cm oral CBCT scan.

updated phantom. The algorithm terminates when the 3D image shows no substantial difference to that of the previous cycle. Owing to the inherent low-frequency characteristic of scatter distribution, the Monte Carlo simulated scatter data are usually subject to interpolation and smoothing (Colijn and Beekman 2004). Because a coarse voxel phantom will not affect the overall scatter distribution, the initial and the new reconstructions to obtain and update the phantom could be performed with a lower resolution than the final reconstruction to obtain the final 3D image and the phantom could be further down-sampled before importing to the Monte Carlo simulator. Additionally, the Monte Carlo simulation could be accelerated on its own by use of appropriate variance reduction techniques (Mainegra-Hing and Kawrakow 2010).

In such algorithms, the voxel phantom is created from the reconstructed 3D image. Simple threshold segmentation is often employed to classify and define the regions of bony tissue, soft tissue and air. Further segmentation would add more details to the phantom whereas the influence on scatter estimation should be negligible. In comparison, the general morphological information over the axial plane, such as the size and shape of the object, are of greater importance to scatter distribution. This leads to a problem for CBCT scan with limited field of view (FOV), where the resulting image is truncated. This kind of image can only lead to an incomplete phantom of the patient and would result in false scatter estimation via the Monte Carlo simulation. Therefore, for the scatter correction to be successful, it is crucial to predict the missing part which is situated outside of the FOV during the scan. Bertram *et al* (2008) proposed a method based on the raw projection data. The volume of the object was extended beyond the FOV by iteratively deforming a 3D mesh model, which is composed of water and expected to approximate the x-ray transmission of the entire object in every angular projection. This approach has been validated for abdominal CBCT, where the missing part is mainly soft tissue. However, it may not be applicable to cases involving more complex structures. Besides, the iterative mesh deformation may substantially increase the total time needed for scatter correction.

This study proposes a novel approach to restore the volume of the object (patient) in CBCT with limited FOV for Monte Carlo scatter correction. It makes use of the image registration technique and requires a standard model of the object (patient). The approach is evaluated for dedicated CBCT of the head and neck, where heavy truncation is very common.

VI.B.2. Materials and methods

Two cases of adult patients imaged with the 3D Accuitomo 170 CBCT system (J. Morita, Japan) were selected for investigation. Both scans had been performed with a tube potential of 90 kV, a tube current of 5.0 mA and a FOV of 60×60 mm (diameter \times height). The FOV had been focused on local sites of the dentition. Each scan comprised 512 effective projections that were evenly distributed over 360° . Each projection image consisted of 400×400 pixels, with a pixel size of $254 \times 254 \mu\text{m}^2$. The central axial slice of the reconstructed image is shown in Fig. 6.5.

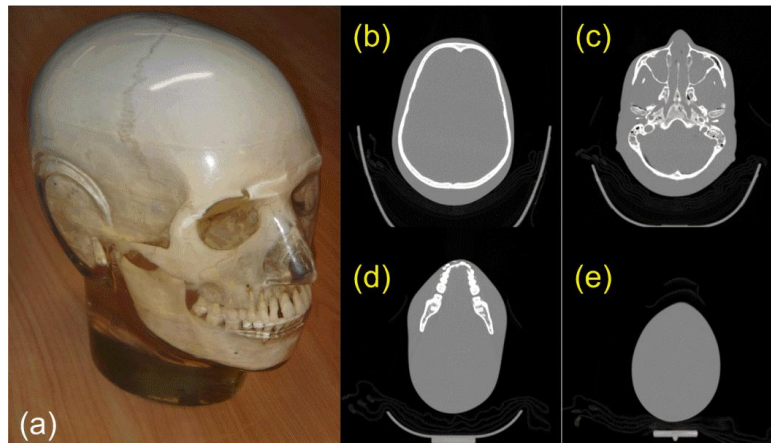


Fig. 6.6 (a) An artificial human head and neck phantom used as the *model* in this work. Selected axial slices of the corresponding MSCT scan at different levels: (b) cranial, (c) skull base, (d) jaw bone and (e) neck.

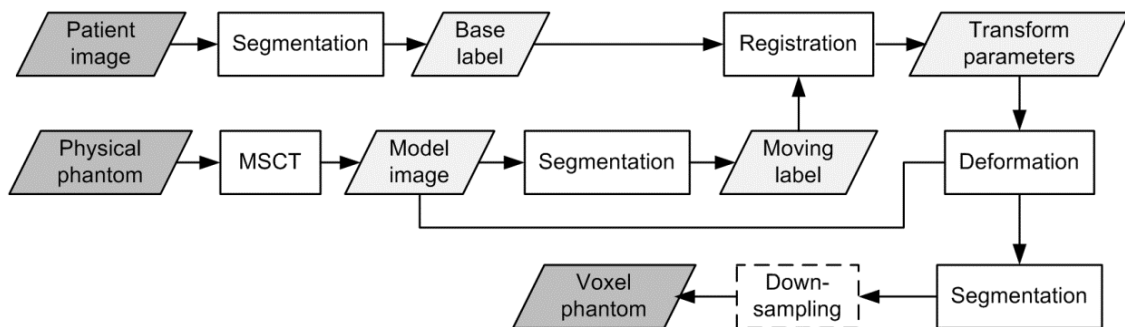


Fig. 6.7 Flowchart of the model-based volume restoration approach for Monte Carlo scatter correction in CBCT with limited FOV.

To create a voxel phantom which not only preserves the patient information shown in the reconstructed image but also accounts for the region beyond the FOV, a standard model of the patient was prepared. In this study, the model was based on a physical phantom as shown in Fig. 6.6(a). The phantom represents typical morphological characteristics of the head and neck for human adults. It has a highly simplified anatomy, where the skeleton is made by a cadaveric sample while the rest is homogeneous tissue-equivalent plastic. The phantom was scanned with multi-slice computed tomography (MSCT) using sufficiently large FOV and sufficiently high resolution. The resulting 3D image showed the complete model and had an image quality high enough to be considered artefact-free. Selected axial slices of the model image are shown in Fig. 6.6(b)-(e).

The next step is to register the 3D image of the model to that of the patient. Image registration is the process of determining the spatial transform that maps points of the object from one image to homologous points in the second image (Ibanez *et al* 2005). The patient and the model are two different objects, so the registration aimed to achieve such a transform to the largest possible extent. For continuity in space, the entire model had to be deformed while matching the corresponding structure to that shown in the limited FOV of the patient. Hypothesis of this approach was that given the inherent natural correlation between the regions within and beyond the FOV, the registered model image should be a fair estimate for the morphology of the patient. In our cases, the jaw bones were set to be the labels in registration, i.e. the primary goal was to align the jaw bones presented in the model and the patient images. This was under the assumption that the general size and shape of the patient,

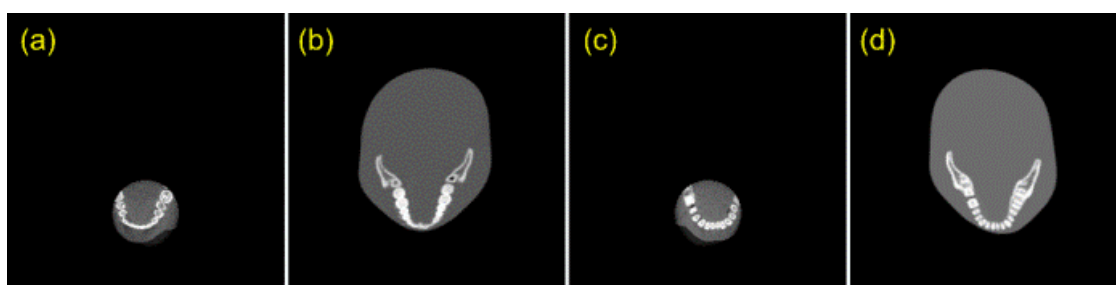


Fig. 6.8 Patient images padded up to a large dimension in plane and the corresponding model image after registration. (a) and (b): patient case 1. (c) and (d): patient case 2.

especially around the head and neck, depend largely on the skeleton. The label registration also minimized the influence of artefacts presented in the patient image, because only a small distinctive part (the bone) of the image was used in determining the transform. The deformation explored in registration was described by an Affine transform, which includes the rotation, scaling, shearing and translation in 3D. The registration is conducted in physical space using coordinates of the patient image as reference, so the registered model image was able to reside exactly at the position where the patient underwent the CBCT scan.

Flowchart of this model-based approach for volume restoration of the patient image is shown in Fig. 6.7. In Monte Carlo scatter correction, the voxel phantom derived from the registered model image was used as a substitute for the incomplete patient image. Since the patient image was not directly used in creating the phantom, iterative updating of the phantom was not needed and the Monte Carlo simulation was only performed for one cycle. The Monte Carlo simulator for the Accutomo CBCT system was available from a previous study (Zhang *et al* 2011), which accurately characterized the radiation field and scanning geometry. Scatter distribution was estimated for 120 equally spaced angular projections. The data was smoothed with the Richardson-Lucy fitting (Colijn and Beekman 2004) and interpolated for 512 angles. The scatter magnitude with respect to the raw projection data was calibrated via a simple procedure: Projection images, including both the primary and the scatter signals, were simulated for a series of objects with different attenuating properties; A linear scaling formula can be found by matching these simulated images to each corresponding experimental image; The simulated scatter data, using this scaling formula, should match the scatter data contained in the raw projection of the patient; The scaling parameters are specific to the selected exposure setting.

VI.B.3. Results and discussion

Figure 6.8 shows the registration results, where the patient images were padded up to a large dimension in axial plane in order to fit in the entire model. The image center in physical space was kept at the center of the original patient image. The idea of registration between a model and a real patient image can also be found for quality assessment of oral CBCT images (Loubele *et al* 2008), while it is more difficult in our case because of the large discrepancy on the size of the FOV. It can be observed that the model image suffers from unrealistic shearing during the registration, while the skeletal regions seem to match. This effect might be due to the large difference between the model and the patient from the beginning. It could therefore be beneficial to use more specific models for different patient groups, such as pediatric, adult, male, female, obese, etc. This also implies the need for choosing the most suitable transform and for adding more restrictions on the deformation.

In order to preclude the influence of other scatter correction strategies that may have been implemented in the commercial reconstruction program of the system, the filtered back-projection (FBP) algorithm as originally proposed by Feldkamp *et al* (1984) was used. The comparison of the

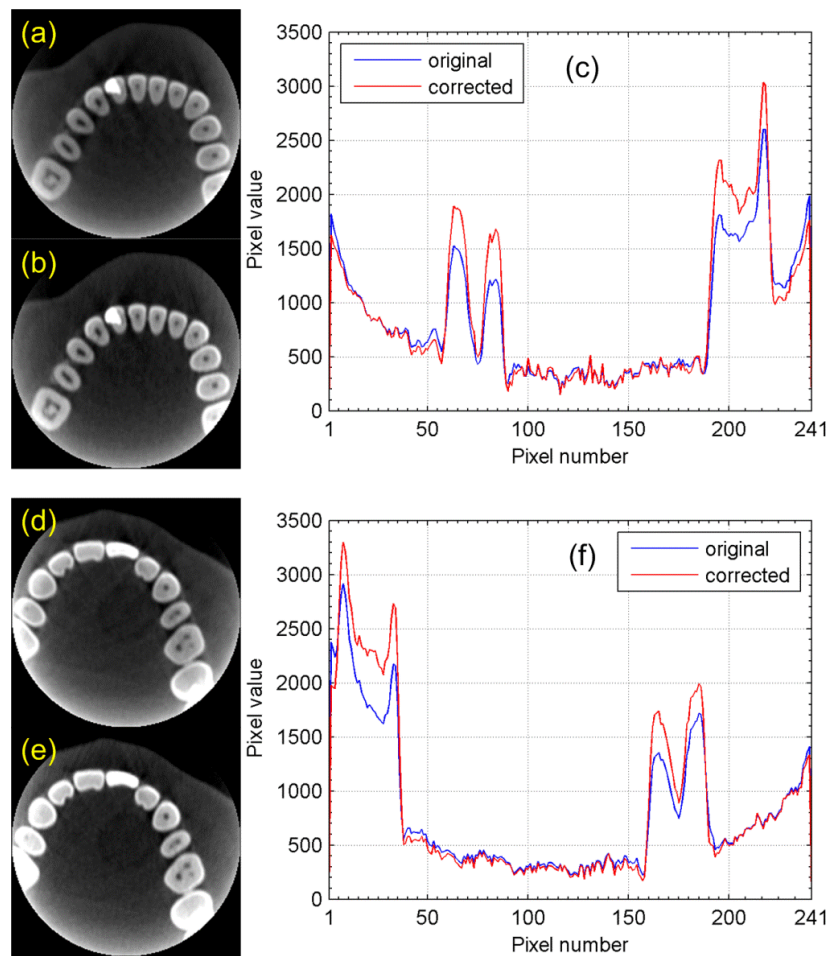


Fig. 6.9 Comparison of the reconstructed images with and without Monte Carlo scatter correction using the model-based volume restoration. (a)-(c): patient case 1. (d)-(f): patient case 2.

resulting image quality with and without Monte Carlo scatter correction is shown in Fig. 6.9. The reconstructed images have an isotropic voxel resolution of $250\ \mu\text{m}$ and are not in the Hounsfield Units (HU) scale. It can be observed that the scatter correction helps in reducing the streak artefacts around the teeth. The profiles show that the corrected images have up to 15% higher contrast resolution between the bony and the soft tissue regions. This represents a substantial improvement in image quality. No additional artefact has been found due to the remaining discrepancy between the patient and the registered model (restored volume).

VI.B.4. Conclusion

This study proposes a model-based approach to restore the volume of patient image for Monte Carlo scatter correction in CBCT with limited FOV. The approach largely exploits the low-frequency characteristic of scatter distribution and approximates the patient morphology beyond the FOV by deforming a standard model using image registration techniques. Preliminary results suggest this approach is feasible in challenging applications of dedicated CBCT of the head and neck. Potential ways to further explore the usefulness and efficacy of this approach have also been pointed out.

Concluding Summary

This doctoral study investigated the dedicated cone beam CT (CBCT) for head and neck imaging from a physics point of view and via the computer simulation approach. The objective was to develop an accurate, efficient and flexible simulation tool and to apply it for quality assurance, system evaluation and optimization. The simulation tool was expected to be applicable to CBCT in general. The objective has been fulfilled with five chapters as described in the thesis: a preliminary study, an in-depth study about the simulation technique and three applications. It should be noted that these applications were only selected examples. While delivering numerical, image and phantom data, this doctoral study has a greater value in introducing, exploring and demonstrating new methodologies for medical imaging research.

Preliminary Study (Chapter II)—Basic steps and components for CBCT simulation were worked out in this chapter, where the system structure and the image acquisition geometry were modeled using the Monte Carlo technique. Special attention was paid to the object undergoing the CBCT scan. Considering that computational phantoms for small experimental animals are important in medical imaging and radiation dosimetry researches, we took the rat as an example. Among different methods, the boundary representation method by use of non-uniform rational B-splines (NURBS) was adopted to develop a rat computational phantom based on the previously obtained segmentation data for cryo-sectional color photographic images of an adult male Sprague–Dawley rat. Continuous two-dimensional contours for a total of 14 major structures were outlined from the downscaled anatomical atlas, corresponding to a voxel size of $0.2 \times 0.2 \times 0.2 \text{ mm}^3$, and stacked to reconstruct the 3D shapes. The NURBS model was then appropriately fitted through the surface of each organ. Monte Carlo CBCT simulation was performed focusing on the thorax region to demonstrate the usefulness of the computational phantom in radiological imaging. The integrated whole-body geometry was presented with smooth internal and exterior boundaries. Organ centroid coordinates and volume information were tabulated for future comparison purposes. The rat phantom can be used in 3D dose calculation and for other computational applications as well. We learned also how the CBCT simulation could be improved for efficiency and for better characterization of the imaging process.

Hybrid Simulation Technique (Chapter III)—We proposed a hybrid technique to simulate the complete chain of an oral CBCT system for the study of both radiation dose and image quality. The model was developed around a 3D Accutomo 170 unit (J Morita, Japan) with a tube potential range of 60–90 kV. The Monte Carlo technique was adopted to simulate the x-ray generation, filtration and collimation. Exact dimensions of the bowtie filter were estimated iteratively using experimentally acquired flood images. Non-flat radiation fields for different exposure settings were mediated via so-called *phase spaces*. Primary projection images were obtained by ray tracing at discrete energies and were fused according to the 2D energy modulation templates derived from the phase space. Coarse Monte Carlo simulations were performed for scatter projections and the resulting noisy images were smoothed by Richardson–Lucy fitting. Resolution and noise characteristics of the flat panel detector were included using the measured modulation transfer function (MTF) and the noise power spectrum (NPS), respectively. The Monte Carlo dose calculation was calibrated in terms of kerma free-in-air about the isocenter, using an ionization chamber, and was subsequently validated by comparison against the measured air kerma in water at various positions of a cylindrical water phantom. The resulting dose discrepancies between the measured and the calculated data were found $<10\%$ for most cases. Intensity profiles of the experimentally acquired and simulated projection images of the water phantom showed comparable fractional increase over the common area as changing from a small to a

large field of view, suggesting that the scatter was accurately accounted. Image validation was conducted using two small phantoms and the built-in quality assurance protocol of the system. The reconstructed simulated images showed high resemblance on contrast resolution, noise appearance and artefact pattern in comparison to experimentally acquired images, with <5% difference for voxel values of the aluminum and air insert regions and <3% difference for voxel uniformity across the homogeneous PMMA region. The detector simulation by use of the MTF and NPS data exhibited a big influence on noise and the sharpness of the resulting images. The hybrid simulation technique is flexible and therefore has wide applicability for CBCT related questions.

Application to System Design (Chapter IV)—The hybrid simulation approach offers an opportunity of exploring the CBCT system beyond its provided setting or design, as a direct way to system optimization. Our study as described in this chapter focused on the source structure—the filtration—of the system. Bowtie filtration is widely adopted in current multi-slice computed tomography (MSCT) and cone beam computed tomography (CBCT) to modulate the output of the radiation source. Our aim was to formulate and optimize the shape of bowtie filter and quantify the influence on system performance for a dedicated head and neck CBCT system with an offset scanning geometry, by use of a validated hybrid simulation technique. The system uses 90 kV tube potential and the largest field of view (FOV) is 140 × 75 mm. Three bowtie filters were developed to produce uniform flux intensity in the projection image of cylindrical objects of diameter 14, 16 and 18 cm. The influence of these simulated filters was compared to the original flat filtration in terms of the output radiation field, the dose delivered to the object, the scatter distribution in projections and the quality of the reconstructed image. Compared against flat filtration, dose reduction for the bowtie case, examined as a function of radial distance within a 16 cm diameter water cylinder, varied from 8.7% at the center to 53.8% at the periphery. Scatter reduction, quantified using scatter-to-primary ratio (SPR) in projection images, was up to 37.6% for a 14 cm diameter PMMA phantom. Using the supplied routine image reconstruction, bowtie filtration resulted in comparable noise appearance, contrast resolution and artefact pattern for computational anatomical phantoms, with <5% difference in contrast-to-noise ratio (CNR), which suggests modification to the image pre-processing and the reconstruction is required. The hybrid simulation approach can be used to explore the impact of proposed system component and design changes.

Application to Dose Evaluation (Chapter V)—Radiation dose is an important issue to be considered for medical imaging modalities that are based on ionizing radiation. The objective of this study was to explore Monte Carlo modeling for dose calculations in dedicated cone beam oral and maxillofacial CT, to assess the dose distribution and to investigate the dose influential factors. The simulation model was established for two very different CBCT systems dedicated in oral and maxillofacial imaging. The radiation field and the beam quality for various exposure settings were accurately characterized. An experimental calibration procedure based on a relatively free dose-in-water measurement was introduced, which managed to correlate the Monte Carlo dose estimates with the operational electric charge across the x-ray tube. Dose calculations were performed with the head and neck part of four computational anatomical phantoms undergoing typical CBCT examinations. Great care has been taken in setting up the imaging geometry and in accommodating the dose calculation schema. The simulation results compared favorably to the dose range reported by experimental measurement with physical anthropomorphic phantoms. The doses are highly dependent on the operating tube potential as well as the size and position of the field of view. Organ doses and the effective doses show >100% and up to 30% differences, respectively, among the phantoms under the same exposure setting of the same CBCT system, suggesting large dose difference among patients. Point dose distribution has also been obtained for assessing the dose profile in-plane. Overall, dedicated cone beam CT of the oral and maxillofacial region is associated with large dose variation. The approach of Monte Carlo modeling is flexible and well-suited for efficient dose evaluation.

Application to Image Quality (Chapter VI)—Scatter remains a major cause of image artefacts in CBCT. The hybrid simulation technique provides an efficient way to track the scattered radiation, predict the scatter distribution and separate the scatter signal from primary signal. This study consists of two parts, looking into the scatter associated with CBCT scan from two different perspectives. Part A: Assessment of the central artefact in offset CBCT. The *central artefact* is commonly seen in cone beam CBCT with an offset scanning geometry. This study evaluates the hypothesis that such artefact is caused by the rotationally asymmetric distribution of scatter. Predictions were examined by use of the hybrid simulation model in a simple experiment. The model was parameterized according to the Scanora 3D CBCT system (Soredex-PaloDEX, Finland). Computational cylinder phantoms of different cross-sections and internal structures were simulated under various symmetric and asymmetric settings. The integrated commercial software tool was employed for image reconstruction. Results confirmed that the scatter was the source of the central artefact. It was also found that the artefact was particularly apparent with the algebraic iterative reconstruction. The degree of asymmetry, by either the object's structure or eccentric placement, was much more influential than the effect of the truncated FOV. These findings were also illustrated with a computational anatomical phantom of the adult human head. Part B: A model-based volume restoration approach for Monte Carlo scatter correction in image reconstruction of CBCT with limited FOV. Among various post-processing strategies to correct the scatter, the Monte Carlo simulation technique has been useful in accurately estimating the scatter distribution. This technique, however, requires a 3D computational phantom of the patient, which is typically obtained from the reconstructed 3D image and is not fully available for CBCT scans with limited FOV. This study proposes a novel approach to restore the volume of patient in such cases by use of a standard patient model and image registration techniques. As demonstrated for the 6×6 cm oral CBCT scan, a full-field model image, created from a physical head and neck phantom of human adults, was registered to the truncated patient image and then successfully imported to Monte Carlo simulation for scatter estimation. Scatter correction was achieved by subtracting the Monte Carlo scatter data from the raw data on a projection-by-projection basis. Comparing to the original data, the reconstructed image with scatter correction showed reduced streak artefacts and an improved contrast resolution of up to 15% between the soft and bony tissue. This volume restoration approach exploits the low-frequency characteristic of the scatter distribution. It can be further optimized and implemented in practice.

Advantages, limitations and computational complexity—The hybrid simulation technique accounts for the complete imaging chain of a CBCT system. It starts with the x-ray generation, filtration and collimation, delivers a cone beam radiation field, continues with angular projections through a 3D voxel phantom, calculates the dose distributions in pre-defined regions of interest, produces primary and scatter images separately, applies the measured characteristics of the flat panel detector, follows the image pre-processing procedures and results in a sequence of 2D projection data ready for volumetric reconstruction. This technique is hybrid by including both dose and image related aspects of the imaging process, splitting the system structure into source, projection, and detector, combining deterministic and stochastic methods, making use of the measured detector characteristics as well as different acceleration and variance reduction techniques.

Although the resolution and noise properties of the flat panel detector were carefully included, the image signals in angular projections were produced with perfect energy integrating efficiency, which was a simplification. In theory, it should be possible to simulate the detector in greater detail, i.e. continue the Monte Carlo radiation transport inside of the detector and calculate the dose delivered to each sensor element. Unfortunately, detailed information of the detector is normally unavailable. In this regard, a viable alternative would be estimating the energy absorption based on the thickness of the conversion screen layer and the incident angle of x-ray photons. In modeling the dedicated head and neck CBCT systems, this should have little effect on the final image quality because the cone angle is relatively small, let alone any local difference that might have been introduced to the sparse

scatter distributions can be easily smeared out by the fitting process. Apart from this aspect, the detector simulation can be more complicated on larger CBCT systems that are equipped with anti-scatter grids. Full simulation of the radiation transport within the nested grid space is surely feasible. However, ignoring further particle interactions with the grid itself, an analytical direction filtering procedure just prior to the signal detection would be sufficient to model the function of the grid.

In determining the bowtie filter of the Accuitomo system, the flood field profile simulated with ideal detector response was compared iteratively against the measured one, where the normalized intensity curves were mainly used. This approach was only valid on one condition: that the signal intensity in real images stays strictly proportional to the magnitude of incident energy fluence. A dramatic change of the detector gain over 2D, especially to the horizontal direction, would have induced error in the bowtie dimension established to the simulation model. However, this is unlikely to be the case because the dose calculation results, using the modeled radiation field, also show agreement with experimentally measured data. As for the detector dependence on the energy spectrum, no substantial difference was observed among the normalized intensity curves acquired with different tube potentials, suggesting that its influence on the simulation model was minimal.

There are several limitations to the hybrid simulation model established to the Scanora system when assessing the effect of the proposed bowtie filtration. Firstly, the scatter generated within the source simulation model, particularly by the bowtie filter, was not taken into account. A practical solution to tackle this issue would be back-projecting the output phase space towards the focal spot position and labeling the deflecting photons prior to the projection simulation. However, the difference is expected to be minimal, considering the small FOV of the Scanora. Secondly, the advantage of bowtie filtration in relaxing the dynamic range of the detector is difficult to validate, although the flux intensity has been normalized. The exact contribution in this aspect depends on the detector of the actual system, where more information is needed. Thirdly, the scatter and the primary projection images were collected with a perfect and constant energy absorbing efficiency in simulation before application of the detector MTF and NPS. This may remove part of the modulation effect by bowtie filters. Finally, the reconstruction was conducted using the existing commercial software provided with the imaging system and hence is not designed specifically for use with the projection data acquired under bowtie filtration. The existing scatter correction and artefact reduction measures may conflict with the presence of a non-flat radiation field. A further step would be exploring custom reconstruction for the data considered here, which takes into account the reduced scatter as well as the increased primary signal and noise uniformity.

The computational efficiency is an important factor to be considered when developing computational tools, which are usually quantified in terms of central processing unit (CPU) time, random access memory (RAM) size, etc. However, the simulation technique that we developed is more about the 'method to simulate' (efficacy) rather than the 'speed to simulate' (efficiency). The system information for dedicated head and neck CBCT is much less available than that for larger CBCT systems, such as those for use in image-guided radiotherapy, so we first had to search and combine proper methods in different steps in order to work out the full simulation chain.

With the directional Bremsstrahlung splitting (DBS) and the Bremsstrahlung cross-section enhancement (BCSE) measures in simulating the radiation source, the x-ray generation is still the most time-consuming process and produces large-size phase-space data. Fortunately, it has only to be simulated once for each considered tube potential. Subsequent filtration and collimation simulation is much faster, except for the iterative search on non-flat absorber dimensions. This again has to be performed only once. Primary projections are based on the analytical ray tracing, thus can be finished per angle and per energy in a rather short time, namely orders of seconds. The simulation speed for scatter projections is highly dependent on the phantom complexity as well as on the required dose statistics and the smoothness of the scatter distribution. Owing to the scatter acceleration measure, only coarse Monte Carlo simulations are needed. The total time to simulate scatter projection images

is therefore not much more than that required by dose calculations. However, Monte Carlo simulations for the dose and scatter estimation were realized separately. First, it was difficult to keep track of the statistical uncertainty for both dose and scatter distributions at the same time. Second, the scatter images were conveniently obtained on a projection-by-projection basis, whereas for dose calculation each particle on the phase space was transported for all angular projections before moving onto the next such that the energy deposition can be grouped into the correct initial history. Fitting the scatter distribution and applying the detector MTF and NNPS add no substantial computation time to the entire image simulation chain.

Future Outlook—Given the limitations that we found in implementation and application of the hybrid simulation technique, this doctoral study might be extended in various directions:

We have compared different phantom representation methods in Chapter I. However, the voxel-based approach was always adopted to describe the image object in simulation of the angular projections. Such geometry is convenient for implementation with currently available Monte Carlo codes. Voxel-based representation is also easier for generalization, i.e. can always be used to describe very complex (anatomical) structures. However, such convenience is achieved at the cost of computation time. To improve the computational efficiency, different methods have been proposed to describe the geometry in Monte Carlo simulation, such as the triangular mesh geometry (Badal *et al* 2009). Therefore, it will be interesting to benchmark the simulation results from different geometric representations and compare the associated computational complexity and efficiency. Similarly, it is also of interest to compare different physics implementations in various Monte Carlo code systems.

Another potential way to expand the present study is also about the phantom. In addition to the geometric contrast phantom and the anatomical phantoms as demonstrated in this study, the medical internal radiation dose (MIRD)-based stylized phantoms (Bouchet *et al* 1999) and more anatomical phantoms representing various human groups (Zaidi and Tsui 2009) can be used in the same manner, for both dose evaluation and the evaluation of image quality. Phantom resolution and the anatomical realism are important factors to be considered. Phantoms based on the boundary representation method, for instance, are free of the problems that occurred from the rigid separation of the head and neck from the trunk as shown in Chapter V. The ability of spatial deformation may help in adjusting the gesture (Na *et al* 2010). It also provides convenience to manipulate the existing phantom by adding pathological features, such as to describe an implant case by modifying a dental site with an artificial substitute. Techniques that may help in characterizing the oral and maxillofacial anatomy, a complex mixture with bony tissue, soft tissue and air cavities, could also be potentially very useful. This may also add clinical relevance to application of the simulation technique.

In Chapter VI, part A, the simulation approach was adopted to answer an interesting question, ‘Whether or not the central artefact in offset CBCT is caused by scatter’. In order to do so, a hypothesis was proposed, with three subsequent predictions to examine. The emphasis was on the simulation experiment that we designed, where so-called ‘symmetrical’ and ‘asymmetrical’ scenarios were created in the simulated imaging setting. The simulation allowed us to identify and investigate the influence of scatter (apart from the primary signals). However, since there is no way to separate or get rid of the scatter in a real imaging setting, clinical images can only be used to show the problem (the central artefact as in Fig. 6.1), but infeasible to be compared with the simulated images. The appearance of central artefact has been quite obvious, so we only made qualitative (instead of quantitative) analysis to simply check if the artefact is shown or not. Therefore, it might be interesting to find a measure that can be used on both simulated and experimentally acquired image to quantify and compare the artefact and the image quality in a more systematic manner.

Difference reconstruction methods, including the filtered back-projection (FBP) and the algebraic reconstruction technique (ART) were mentioned in our study, but both are incorporated with the commercial imaging system, where we had no access to any specific parameter setting. It would be very helpful for image quality analysis if we have such access or even custom reconstruction tools.

Next to that of the scatter, influence of the reconstruction to the central artefact in offset CBCT can be investigated. As suggested also in Chapter IV, a custom reconstruction, which takes into account the reduced scatter as well as the increased primary signal and noise uniformity, can be used to further assess the effect of the proposed bowtie filtration.

In Chapter VI, Part B, a volume restoration approach was proposed to tackle the problem of limited FOV for implementation of the Monte Carlo scatter correction in CBCT. It would have been a strong validation if we could use it to correct artefact described in Part A. Unfortunately, the CBCT imaging system that we chose for investigation were two different systems: Scanora for Part A, which uses an offset geometry, and Accuitomo for Part B, where we have access to the raw data. Access to the raw data is a precondition to Monte Carlo scatter correction, so we had to focus on the Accuitomo and use a couple of patient cases to illustrate the efficacy and efficiency of the volume restoration as well as the scatter correction technique. However, it is of interest to apply the simulation, the volume restoration and the scatter correction technique to a CBCT system where data are more available to test the performance.

As mentioned above, the hybrid simulation technique has been optimized for efficiency in different ways. However, it might be further improved with the support of more advanced computer techniques, such as the parallel computing and the Graphics Processing Unit (GPU)-based computing techniques. A review of these techniques in current medical physics researches can be found in Pratz and Xing (2011). This may help the simulation approach to be applied in a practical clinical setting.

Apart from the dedicated CBCT systems for head and neck imaging and the CBCT systems integrated with the linear accelerator for use in image-guided radiotherapy, CBCT has also been applied in dedicated breast imaging (Chen and Ning 2002, Chen *et al* 2008). It is of interest to apply the proposed hybrid simulation technique in this study to dedicated breast CBCT, investigate dose and image related aspects and compare with similar techniques that have been introduced to such systems. Furthermore, CBCT has also been increasingly integrated in hybrid dual-modality systems for use in nuclear medicine imaging, such as SPECT-CT and PET-CT systems (IAEA 2008). In addition to making use of the simulation technique in similar applications, it might be possible to explore new modeling approaches for the acquired co-registered CT and nuclear medicine image data, especially for image-based patient-specific dosimetry (Stabin 2006).

Bibliography

- Ali E S M and Rogers D W O 2007 Efficiency improvements of x-ray simulations in EGSnrc user-codes using bremsstrahlung cross-section enhancement (BCSE) *Med. Phys.* 34:2143–54
- Ali E S M and Rogers D W O 2008 Benchmarking EGSnrc in the kilovoltage energy range against experimental measurements of charged particle backscatter coefficients *Phys. Med. Biol.* 53:1527–43
- Andreo P 1991 Monte Carlo techniques in medical radiation physics *Phys. Med. Biol.* 36:861–920
- Agostinelli S *et al* 2003 GEANT4—a simulation toolkit *Nucl. Instrum. Methods Phys. Res. A* 506:250–303
- Ay M R and Zaidi H 2005 Development and validation of MCNP4C-based Monte Carlo simulator for fan- and cone-beam x-ray CT *Phys. Med. Biol.* 50:4863–85
- Badal A *et al* 2009 penMesh—Monte Carlo radiation transport simulation in a triangle mesh geometry *IEEE Trans. Med. Imag.* 28:1894–901
- Badano A and Sempau J 2006 MANTIS: combined x-ray, electron and optical Monte Carlo simulations of indirect radiation imaging systems *Phys. Med. Biol.* 51:1545–61
- Berger M J *et al* 2010 XCOM: Photon Cross Section Database v1.5 (Gaithersburg, MD: National Institute of Standards and Technology) <http://physics.nist.gov/xcom>
- Bertram M *et al* 2008 Monte Carlo scatter correction for cone-beam computed tomography with limited scan field-of-view *Proc. SPIE* 6913:69131Y
- Beutel J *et al* 2000 Handbook of medical imaging: Volume 1. Physics and psychophysics (Bellingham, WA: SPIE)
- Bitar A *et al* 2007 A voxel-based mouse for internal dose calculations using Monte Carlo simulations (MCNP) *Phys. Med. Biol.* 52:1013–25
- Boone J M 2010 Method for evaluating bow tie filter angle-dependent attenuation in CT: Theory and simulation results *Med. Phys.* 37:40–8
- Bootsma G J *et al* 2011 The effects of compensator and imaging geometry on the distribution of x-ray scatter in CBCT *Med. Phys.* 38:897–914
- Bouchet L G *et al* 1999 MIRD Pamphlet No. 15: radionuclide S values in a revised dosimetric model of the adult head and brain *J. Nucl. Med.* 40:62S–101S
- Brown F B (ed) 2003 MCNP—A general Monte Carlo N-particle transport code (version 5) *Report LA-UR-03-1987* (Los Alamos National Laboratory, Los Alamos, NM)
- Caon M 2004 Voxel-based computational models of real human anatomy: A review *Radiat. Environ. Biophys.* 42:229–35
- Chen B and Ning R 2002 Cone-beam volume CT breast imaging: Feasibility study *Med. Phys.* 29:755–70
- Chen L *et al* 2008 Feasibility of volume-of-interest (VOI) scanning technique in cone beam breast CT—a preliminary study *Med. Phys.* 35:3482–90
- Colijn A P and Beekman F J 2004 Accelerated simulation of cone beam x-ray scatter projections *IEEE Trans. Med. Imag.* 23:584–90
- Colijn A P *et al* 2004 Experimental validation of a rapid Monte Carlo based micro-CT simulator *Phys. Med. Biol.* 49:4321–33
- Ding G X *et al* 2007 Characteristics of kilovoltage x-ray beams used for cone-beam computed tomography in radiation therapy *Phys. Med. Biol.* 52:1595–615
- Ding G X *et al* 2008 Accurate patient dosimetry of kilovoltage cone-beam CT in radiation therapy *Med. Phys.* 35:1135–44

- De Vos W *et al* 2009 Cone-beam computerized tomography (CBCT) imaging of the oral and maxillofacial region: a systematic review of the literature *Int. J. Oral Maxillofac. Surg.* 38:609–25
- Dobbins J T III *et al* 2006 Intercomparison of methods for image quality characterization: II. Noise power spectrum *Med. Phys.* 33:1466–75
- Doi K 2006 Diagnostic imaging over the last 50 years: research and development in medical imaging science and technology *Phys. Med. Biol.* 51:R5–27
- Downes P *et al* 2009 Monte Carlo simulation and patient dosimetry for a kilovoltage cone-beam CT unit *Med. Phys.* 36:4156–67
- Endo M *et al* 2001 Effect of scattered radiation on image noise in cone beam CT *Med. Phys.* 28:469–74
- Fahrig R *et al* 2006 Dose and image quality for a cone-beam C-arm CT system *Med. Phys.* 33:4541–50
- Feldkamp L A *et al* 1984 Practical cone-beam algorithm *J. Opt. Soc. Am.* A1:612–9
- Fishman G S 1995 Monte Carlo: concepts, algorithms, and applications (New York: Springer)
- Gu J *et al* 2009 The development, validation and application of a multi-detector CT (MDCT) scanner model for assessing organ doses to the pregnant patient and the fetus using Monte Carlo simulations *Phys. Med. Biol.* 54:2699–717
- Guerrero M E *et al* 2006 State-of-the-art on cone beam CT imaging for preoperative planning of implant placement *Clin. Oral Investig.* 10:1–7
- Gupta R *et al* 2006 Ultra-high resolution flat-panel volume CT: fundamental principles, design architecture and system characterization *Eur. Radiol.* 16:1191–205
- Graham S A *et al* 2007 Compensators for dose and scatter management in cone-beam computed tomography *Med. Phys.* 34:2691–703
- Han E *et al* 2006 Revisions to the ORNL series of adult and pediatric computational phantoms for use with the MIRD schema *Health Phys.* 90:337–56
- Hansis E *et al* 2010 Iterative reconstruction for circular cone-beam CT with an offset flat-panel detector *IEEE Nucl. Sci. Symp. Conf. Rec.* 2228–31
- Horner K *et al* 2009 Basic principles for use of dental cone beam computed tomography: consensus guidelines of the European Academy of Dental and Maxillofacial Radiology *Dentomaxillofac. Radiol.* 38:187–95
- Hounsfield G N 1980 Nobel Award address: computed medical imaging *Med. Phys.* 7:283–90
- HPA 2010a Guidance on the safe use of dental cone beam CT *HPA Report CRCE-010* (Health Protection Agency, UK)
- HPA 2010b Recommendations for the design of x-ray facilities and the quality assurance of dental cone beam CT systems *HPA Report RPD-065* (Health Protection Agency, UK)
- Hubbell J H and Seltzer S M 2004 Tables of X-Ray Mass Attenuation Coefficients and Mass Energy-Absorption Coefficients v1.4 (Gaithersburg, MD: National Institute of Standards and Technology) <http://physics.nist.gov/xaamdi>
- IAEA 2008 Clinical applications of SPECT/CT: New hybrid nuclear medicine imaging system *International Atomic Energy Agency IAEA-TECDOC-1597*
- ICRP 2002 Basic anatomical and physiological data for use in radiological protection: reference values *International Commission on Radiological Protection Publication 89*
- ICRP 2007 The 2007 recommendations of the International Commission on Radiological Protection *International Commission on Radiological Protection Publication 103*
- ICRP 2009 Adult reference computational phantoms *International Commission on Radiological Protection Publication 110*
- ICRU 1984 Stopping powers for electrons and positrons *International Commission on Radiation Units and Measurements Report 37*

- ICRU 1989 Tissue substitutes in radiation dosimetry and measurement *International Commission on Radiation Units and Measurements Report 44*
- IDS 2011 The 34th International Dental Show (Cologne, Germany) <http://www.ids-cologne.de>
- IEC 2003 Medical electrical equipment—characteristics of digital x-ray imaging devices: part 1. Determination of the detective quantum efficiency *International Standard IEC 62220-1* (Geneva: International Electrotechnical Commission)
- Ibanez L *et al* 2005 The ITK software guide (second edition, updated for ITK version 2.4) <http://www.itk.org>
- Jaffray D A and Siewerdsen J H 2000 Cone-beam computed tomography with a flat-panel imager: Initial performance characterization *Med. Phys.* 27:1311-23
- Jarry G *et al* 2006 Characterization of scattered radiation in kV CBCT images using Monte Carlo simulations *Med. Phys.* 33:4320-29
- Joseph P M and Spital R D 1982 The effects of scatter in x-ray computed tomography *Med. Phys.* 9:464-72
- Kalender W A 2006 X-ray computed tomography *Phys. Med. Biol.* 51:R20-43
- Kanamori H. *et al* 1985 Effects of scattered x-rays on CT images *Phys. Med. Biol.* 30:239-49
- Kyriakou Y and Kalender W 2007 Efficiency of antiscatter grids for flat-detector CT *Phys. Med. Biol.* 52:6275-93
- Kawrakow I *et al* 2004 Large efficiency improvements in BEAMnrc using directional bremsstrahlung splitting *Med. Phys.* 31:2883-98
- Kawrakow I *et al* 2009 The EGSnrc code system: Monte Carlo simulation of electron and photon transport *NRCC Report PIRS-701* (Ottawa: National Research Council)
- King S D and Spiers F W 1985 Photoelectron enhancement of the absorbed dose from x-rays to human bone marrow: experimental and theoretical studies *Brit. J. Radiol.* 58:345-56
- Konijnenberg M W *et al* 2004 A stylized computational model of the rat for organ dosimetry in support of perclinical evaluations of peptide receptor radionuclide therapy with ^{90}Y , ^{111}In , or ^{177}Lu *J. Nucl. Med.* 45:1260-9
- Kramer R *et al* 2003 All about MAX: a male adult voxel phantom for Monte Carlo calculations in radiation protection dosimetry *Phys. Med. Biol.* 48:1239-62
- Lai C-J *et al* 2009 Reduction in x-ray scatter and radiation dose for volume-of-interest (VOI) cone-beam breast CT—a phantom study *Phys. Med. Biol.* 54:6691-709
- Lee C *et al* 2007 Hybrid computational phantoms of the male and female newborn patients: NURBS-based whole-body models *Phys. Med. Biol.* 52:3309-33
- Lee C *et al* 2011 Organ doses for reference adult male and female undergoing computed tomography estimated by Monte Carlo simulations *Med. Phys.* 38:1196-206
- Ljungberg M *et al* 1998 Monte Carlo calculations in nuclear medicine: Applications in diagnostic imaging (Bristol, UK: Institute of Physics Publishing)
- Loubele M *et al* 2008 Comparative study of image quality for MSCT and CBCT scanners for dentomaxillofacial radiology applications *Radiat. Prot. Dosim.* 129:222-6
- Loubele M *et al* 2009 Comparison between effective radiation dose of CBCT and MSCT scanners for dentomaxillofacial applications *Eur. J. Radiol.* 71:461-8
- Ludlow J B and Ivanovic M 2008 Comparative dosimetry of dental CBCT devices and 64-slice CT for oral and maxillofacial radiology *Oral Surg. Oral Med. Oral Pathol. Oral Radiol. Endod.* 106:106-14
- Ma C M *et al* 2001 AAPM protocol for 40-300 kV x-ray beam dosimetry in radiotherapy and radiobiology *Med Phys.* 28:868-93
- Mah J K *et al* 2010 Practical applications of cone-beam computed tomography in orthodontics *J. Am. Dent. Assoc.* 141:7S-13S
- Mail N *et al* 2008 An empirical method for lag correction in cone-beam CT *Med. Phys.* 35:5187-96

- Mail N *et al* 2009 The influence of bowtie filtration on cone-beam CT image quality *Med. Phys.* 36:22-32
- Mainegra-Hing E and Kawrakow I 2010 Variance reduction techniques for fast Monte Carlo CBCT scatter correction calculations *Phys. Med. Biol.* 55:4495-507
- Menser B *et al* 2010 Use of beam shapers for cone-beam CT with off-centered flat detector *Proc. SPIE* 7622:762233 1-12
- Min P 2009 Binvox: 3D mesh voxelizer (v1) <http://www.cs.princeton.edu/~min/binvox/>
- Miracle A C and Mukherji S K 2009a Conebeam CT of the head and neck: part 1. Physical principles *Am. J. Neuroradiol.* 30:1088-95
- Miracle A C and Mukherji S K 2009b Conebeam CT of the head and neck: part 2. Clinical applications *Am. J. Neuroradiol.* 30:1285-92
- Moore C J *et al* 2006 Developments in and experience of kilovoltage X-ray cone beam image-guided radiotherapy *Brit. J. Radiol.* 79:566-78
- Na Y H *et al* 2010 Deformable adult human phantoms for radiation protection dosimetry: anthropometric data representing size distributions of adult worker populations and software algorithms *Phys. Med. Biol.* 55:3789-811
- Orth R C *et al* 2009 C-arm cone-beam CT: general principles and technical considerations for use in interventional radiology *J. Vasc. Interv. Radiol.* 20:S538-44
- Pauwels R *et al* 2012 Effective dose range for dental cone beam computed tomography scanners *Eur. J. Radiol.* 81:267-71
- Peixoto P H R *et al* 2008 Photon and electron absorbed fractions calculated from a new tomographic rat model *Phys. Med. Biol.* 53:5343-55
- Peter J *et al* 2000 Analytical versus voxelized phantom representation for Monte Carlo simulation in radiological imaging *IEEE Trans. Med. Imag.* 19:556-64
- Plasticboy Pictures CC 2009 Plasticboy anatomy models <http://www.plasticboy.co.uk/store/about.html>
- Prax G and Xing L 2011 GPU computing in medical physics: A review *Med. Phys.* 38:2685-97
- Rogers D W O 2006 Fifty years of Monte Carlo simulations for medical physics *Phys. Med. Biol.* 51:R287-301
- Rogers D W O *et al* 2009 BEAMnrc users manual *NRCC Report PIRS-0509(A)revK* (Ottawa: National Research Council)
- Ruhrschopf E P and Klingenbeck K 2011a A general framework and review of scatter correction methods in cone-beam CT. Part 1: Scatter compensation approaches *Med. Phys.* 38:4296-311
- Ruhrschopf E P and Klingenbeck K 2011b A general framework and review of scatter correction methods in cone-beam CT. Part 2: Scatter estimation approaches *Med. Phys.* 38:5186-99
- Salvat F *et al* 2003 PENELOPE, A Code System for Monte Carlo Simulation of Electron and Photon Transport (Issy-les-Moulineaux, France: OECD Nuclear Energy Agency)
- Samei E *et al* 2006 Intercomparison of methods for image quality characterization: I. Modulation transfer function *Med. Phys.* 33:1454-65
- Saunders R S Jr and Samei E 2003 A method for modifying the image quality parameters of digital radiographic images *Med. Phys.* 30:3006-17
- Schulze R *et al* 2011 Artefacts in CBCT: a review *Dentomaxillofac. Radiol.* 40:265-73
- Seeram E (ed) 2009 Computed tomography: physical principles, clinical applications, and quality control (3rd edition) (Saunders/Elsevier)
- Segars W P *et al* 2004 Development of a 4D digital mouse phantom for molecular imaging research *Mol. Imag. Biol.* 6:149-59
- Siddon R L 1985 Fast calculation of the exact radiological path for a three-dimensional CT array *Med. Phys.* 12:252-5

- Siewerdsen J H and Jaffray D A 1999 Cone-beam computed tomography with a flat-panel imager: Effects of image lag *Med. Phys.* 26:2635-47
- Siewerdsen J H and Jaffray D A 2000 Optimization of x-ray imaging geometry (with specific application to flat-panel cone-beam computed tomography *Med. Phys.* 27:1903-14
- Siewerdsen J H and Jaffray D A 2001 Cone-beam computed tomography with a flat-panel imager: Magnitude and effects of x-ray scatter *Med. Phys.* 28:220-31
- Siewerdsen J H *et al* 2004 The influence of antiscatter grids on soft-tissue detectability in cone-beam computed tomography with flat-panel detectors *Med. Phys.* 31:3506-20
- Smans K *et al* 2010 Validation of an image simulation technique for two computed radiography systems: an application to neonatal imaging *Med. Phys.* 37:2092-100
- Spezi E *et al* 2009 Monte Carlo simulation of an x-ray volume imaging cone beam CT unit *Med. Phys.* 36:127-36
- Stabin M 2006 Nuclear medicine dosimetry *Phys. Med. Biol.* 51:R187-202
- Stabin M G *et al* 2006 Voxel-based mouse and rat models for internal dose calculations *J. Nucl. Med.* 47:655-9
- Suomalainen A *et al* 2009 Dosimetry and image quality of four dental cone beam computed tomography scanners compared with multislice computed tomography scanners *Dentomaxillofac. Radiol.* 38:367-78
- Theodorakou C *et al* 2012 Estimation of paediatric organ and effective doses from dental cone beam CT using anthropomorphic phantoms *Brit. J. Radiol.* 85:153-60
- Tkaczyk J E *et al* 2004 Simulation of CT dose and contrast-to-noise as function of bowtie shape *Proc. SPIE* 5368:403-10
- Turner A C *et al* 2009 A method to generate equivalent energy spectra and filtration models based on measurement for multidetector CT Monte Carlo dosimetry simulations *Med. Phys.* 36:2154-64
- Valton S *et al* 2006 A FDK-based reconstruction method for off-centered circular trajectory cone beam tomography *IEEE Trans. Nucl. Sci.* 53:2736-45
- Walters B R B *et al* 2002 History by history statistical estimators in the BEAM code system *Med. Phys.* 29:2745-52
- Walters B R B *et al* 2009 Skeletal dosimetry in cone beam computed tomography *Med. Phys.* 36:2915-22
- Wang G 2002 X-ray micro-CT with a displaced detector array *Med. Phys.* 29:1634-6
- Wu L *et al* 2008 An image-based rat model for Monte Carlo organ dose calculations *Med. Phys.* 38:3759-64
- Wunderlich A and Noo F 2007 Achieving uniform noise in direct fan-beam CT reconstruction through bowtie filter design *IEEE Nucl. Sci. Symp. Conf. Rec.* 6:4379-82
- Xu X G *et al* 2007 A boundary-representation method for designing whole-body radiation dosimetry models: Pregnant females at the ends of three gestational periods VRIP-P3, -P6 and -P9 *Phys. Med. Biol.* 52:7023-44
- Yu L *et al* 2010 Dose and image quality evaluation of a dedicated cone-beam CT system for high-contrast neurologic applications *Am. J. Roentgenol.* 194:W193-201
- Zaidi H 1999 Relevance of accurate Monte Carlo modeling in nuclear medical imaging *Med. Phys.* 26:574-608
- Zaidi H and Sgouros G 2002 Therapeutic applications of Monte Carlo calculations in nuclear medicine (Bristol, UK: Institute of Physics Publishing)
- Zaidi H and Tsui B M W 2009 Review of computational anthropomorphic anatomical and physiological models *P. IEEE* 97:1938-53
- Zankl M *et al* 2002 Organ dose conversion coefficients for external photon irradiation of male and female voxel models *Phys. Med. Biol.* 47:2367-85

- Zbijewski W and Beekman F J 2006 Efficient Monte Carlo based scatter artifact reduction in cone-beam micro-CT *IEEE Trans. Med. Imag.* 25:817-27
- Zhang G *et al* 2008 The development and application of the visible Chinese human model for Monte Carlo dose calculations *Health Phys.* 94:118-25
- Zhang G *et al* 2011 Development and validation of a hybrid simulation technique for cone beam CT: application to an oral imaging system *Phys. Med. Biol.* 56:5823-43
- Zhang G *et al* 2009 Development of a rat computational phantom using boundary representation method for Monte Carlo simulation in radiological imaging *P. IEEE* 97:2006-14
- Zubal I G *et al* 1994 Computerized three-dimensional segmented human anatomy *Med. Phys.* 21:299-302

Abstract

X-ray Computed Tomography (CT) is one of the most important means in current medical imaging. The theory was originally proposed by Godfrey N Hounsfield in 1967. Today, the CT scanners have evolved enormously, in both system design and imaging performance. Cone beam computed tomography (CBCT) is a relatively new CT technique with applications in diagnostic radiology, image-guided surgery and image-guided radiotherapy. The most prominent feature of CBCT is the image acquisition geometry, where volumetric data are acquired within a single rotation of the paired source and detector. As compared to conventional CT, CBCT has a lower dose requirement and the images are produced (reconstructed) with truly isotropic data samples in three-dimensional space and are of a higher spatial resolution. Clinically, CBCT was first introduced for angiography in interventional radiology and later explored as an image-guidance tool in external radiotherapy. Over the last decade, CBCT of the head and neck with dedicated imaging systems has also been increasingly available.

Whether and where can CBCT replace the traditional radiography and CT has become a hot topic in recent years. On the one hand, commercial CBCT systems show large difference from each other, such as the wide range of exposure setting. On the other hand, quality test methodologies used in general radiology still have to be adapted before applied to CBCT. As every emerging technique, regulatory policies and standardization measures for CBCT are yet to be established or improved. As every imaging modality based on ionizing radiation, radiation safety is an issue too. Given all these reasons, investigation and optimization methods and tools are of great interest in current researches. The Monte Carlo simulation technique, for instance, seems to be powerful for CBCT studies by offering the possibility to look into the detailed imaging process from a physics point of view. However, real CBCT systems are very complicated in design architecture. Basic Monte Carlo simulations might therefore be limited in both accuracy and efficiency. The large difference of the CBCT systems demands also high flexibility of the simulation platform.

The objective of this thesis study was to develop an accurate, efficient and flexible simulation tool with general applicability to CBCT, and to apply the simulation tool for quality assurance, system evaluation and optimization of dedicated CBCT of the head and neck. The work consists of five parts, including one preliminary study, one in-depth study of the simulation technique and three selected applications. In the preliminary study, we learned experiences about the basics of CBCT simulation and about different approaches to represent the imaging object within the simulation. In the next study, we developed and experimentally validated a so-called hybrid simulation technique, which accounts for the complete CBCT imaging chain using combined methods and in an efficient manner. The application of this technique, as illustrated in the three subsequent studies, covers the system design, the associated dose and the resulting image quality. We managed to demonstrate the usefulness of the simulation technique in exploring the current CBCT systems beyond their provided hardware design, in systematic evaluation of the dose distribution in typical CBCT examinations as well as in identifying the causation of certain image artefacts and in assisting software algorithms to ultimately improve the image quality. We believe the hybrid simulation technique and the associated new methodologies have a great value not only for CBCT researches but also for medical imaging researches in general.

Professional career Guozhi Zhang

Guozhi Zhang was born in Hubei, China, in July 1986. He received his Bachelor's degree from the School of Life Science and Technology, Huazhong University of Science and Technology (Wuhan, China), in 2008. During the last two years of his undergraduate study, he also worked as a research assistant at the *Britton Chance* Center for Biomedical Photonics, Wuhan National Laboratory for Optoelectronics. From October 2008, he joined the Medical Physics group in Radiology, University Hospital, KU Leuven, in Belgium, for a 4-year doctoral study under the supervision of professor Hilde Bosmans. His research is about advanced Monte Carlo simulation, cone beam computed tomography, computational anatomical phantoms as well as medical image computing and processing. He also obtained a Master-equivalent diploma, Postgraduate Studies in Advanced Medical Imaging, during the first two years of his PhD.

List of Publications

International peer-reviewed journals

- Zhang G**, Marshall N, Jacobs R and Bosmans H 2012 Bowtie filtration for dedicated cone beam CT of the head and neck: A simulation study (submitted)
- Zhang G**, Bogaerts R, Liu Q, Jacobs R and Bosmans H 2012 Monte Carlo modeling for dose calculations in cone beam oral and maxillofacial CT (submitted)
- Zhang G**, Pauwels R, Marshall N, Shaheen E, Nuyts J, Jacobs R and Bosmans H 2011 Development and validation of a hybrid simulation technique for cone beam CT: Application to an oral imaging system *Physics in Medicine and Biology* 56:5823-5843
- Xie T, **Zhang G**, Li Y and Liu Q 2010 Comparison of absorbed fractions of electrons and photons using three kinds of computational phantoms of rat *Applied Physics Letters* 97:033702
- Zhang G**, Xie T, Bosmans H and Liu Q 2009 Development of a rat computational phantom using boundary representation method for Monte Carlo simulation in radiological imaging *Proceedings of the IEEE* 97:2006-2014
- Zhang G**, Liu Q, Zeng S and Luo Q 2008 Organ dose calculations by Monte Carlo modeling of the updated VCH adult male phantom against idealized external proton exposure *Physics in Medicine and Biology* 53:3697-3722
- Wu L, **Zhang G**, Luo Q and Liu Q 2008 An image-based rat model for Monte Carlo organ dose calculations *Medical Physics* 35:3759-3764
- Zhang G**, Luo Q, Zeng S and Liu Q 2008 The development and application of the visible Chinese human model for Monte Carlo dose calculations *Health Physics* 94:118-125
- Zhang G**, Liu Q and Luo Q 2007 Monte Carlo simulations for external neutron dosimetry based on the visible Chinese human phantom *Physics in Medicine and Biology* 52:7367-7383

International conference proceedings & abstracts

- Zhang G**, Jacobs R and Bosmans H 2013 A model-based volume restoration approach for Monte Carlo scatter correction in cone beam CT with limited field of view *Physics of Medical Imaging, SPIE Medical Imaging* (Orlando, Florida) submitted

- Zhang G**, Jacobs R and Bosmans H 2012 Organ absorbed dose and the effective dose calculated using computational anatomical phantoms for dedicated cone beam oral and maxillofacial CT *International Conference on Radiation Protection in Medicine*, IAEA (Bonn, Germany)
- Zhang G**, Jacobs R and Bosmans H 2012 Assessment of the central artefact in cone beam CT imaging with an offset geometry *Physics of Medical Imaging, SPIE Medical Imaging* (San Diego, California)
- Zhang G**, Jacobs R and Bosmans H 2011 Implementation of a human head and neck phantom for cone beam CT imaging simulation *European Medical Physics Engineering Conference, EMPEC* (Dublin, Ireland)
- Zanca F, **Zhang G**, Marshall N, Shaheen E, Salvagnini E, Marchal G and Bosmans H 2010 Software framework for simulating clusters of microcalcifications in digital mammography *International Workshop Digital Mammography* (Girona, Spain) | *Proceedings of Digital Mammography* 689-696
- Zhang G**, Pauwels R, Bosmans H and Jacobs R 2009 Investigation of scattered radiation and dose distribution in dental CBCT imaging using Monte Carlo simulation *The 17th International Congress of Dentomaxillofacial Radiology* (Amsterdam, The Netherlands)
- Liu Q, **Zhang G** and Zeng S 2008 Conversion coefficients for external monoenergetic photon beams in the visible Chinese human model *SPIE Complex Dynamics and Fluctuations in Biomedical Photonics V* (San Jose, California) | *Proceedings of SPIE* 6855:68550J

Book chapter

- Zhang B, Ma J, **Zhang G**, Liu Q, Qiu R and Li J 2009 The Chinese Computational Phantoms: CNMAN, VCH, and CVP *Handbook of Anatomical Models for Radiation Dosimetry* (Eds.: Xu X G and Eckerman K F, Taylor & Francis Group, London, UK)